



**National Library
of Canada**

**Bibliothèque nationale
du Canada**

Canadian Theses Service

Service des thèses canadiennes

Ottawa, Canada
K1A 0N4

NOTICE

The quality of this microform is heavily dependent upon the quality of the original thesis submitted for microfilming. Every effort has been made to ensure the highest quality of reproduction possible.

If pages are missing, contact the university which granted the degree.

Some pages may have indistinct print especially if the original pages were typed with a poor typewriter ribbon or if the university sent us an inferior photocopy.

Reproduction in full or in part of this microform is governed by the Canadian Copyright Act, R.S.C. 1970, c. C-30, and subsequent amendments.

AVIS

La qualité de cette microforme dépend grandement de la qualité de la thèse soumise au microfilmage. Nous avons tout fait pour assurer une qualité supérieure de reproduction.

S'il manque des pages, veuillez communiquer avec l'université qui a conféré le grade.

La qualité d'impression de certaines pages peut laisser à désirer, surtout si les pages originales ont été dactylographiées à l'aide d'un ruban usé ou si l'université nous a fait parvenir une photocopie de qualité inférieure.

La reproduction, même partielle, de cette microforme est soumise à la Loi canadienne sur le droit d'auteur, SRC 1970, c. C-30, et ses amendements subséquents.

THE UNIVERSITY OF ALBERTA

NON-INTRUSIVE OPTICAL FIBER TAPPING

by

MNOON-YAN LOKE

A THESIS

SUBMITTED TO THE FACULTY OF GRADUATE STUDIES AND RESEARCH
IN PARTIAL FULFILMENT OF THE REQUIREMENTS FOR THE DEGREE
OF MASTER OF SCIENCE

DEPARTMENT OF ELECTRICAL ENGINEERING

EDMONTON, ALBERTA

SPRING 1989



National Library
of Canada

Bibliothèque nationale
du Canada

Canadian Theses Service Service des thèses canadiennes

Ottawa, Canada
K1A 0N4

The author has granted an irrevocable non-exclusive licence allowing the National Library of Canada to reproduce, loan, distribute or sell copies of his/her thesis by any means and in any form or format, making this thesis available to interested persons.

The author retains ownership of the copyright in his/her thesis. Neither the thesis nor substantial extracts from it may be printed or otherwise reproduced without his/her permission.

L'auteur a accordé une licence irrévocable et non exclusive permettant à la Bibliothèque nationale du Canada de reproduire, prêter, distribuer ou vendre des copies de sa thèse de quelque manière et sous quelque forme que ce soit pour mettre des exemplaires de cette thèse à la disposition des personnes intéressées.

L'auteur conserve la propriété du droit d'auteur qui protège sa thèse. Ni la thèse ni des extraits substantiels de celle-ci ne doivent être imprimés ou autrement reproduits sans son autorisation.

ISBN 0-315-52813-3

THE UNIVERSITY OF ALBERTA

RELEASE FORM

NAME OF AUTHOR: MNOON-YAN LOKE

TITLE OF THESIS: NON-INTRUSIVE OPTICAL FIBER TAPPING

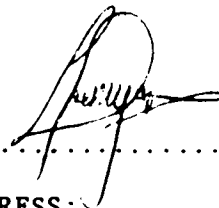
DEGREE FOR WHICH THESIS WAS PRESENTED: MASTER OF SCIENCE

YEAR THIS DEGREE GRANTED: SPRING 1989

Permission is hereby granted to THE UNIVERSITY OF ALBERTA LIBRARY to reproduce single copies of this thesis and to lend or sell such copies for private, scholarly or scientific research purposes only.

The author reserves other publication rights, and neither the thesis nor extensive extracts from it may be printed or otherwise reproduced without the author's written permission.

(SIGNED)



PERMANENT ADDRESS:

345 Happy Garden
Jalan Kuchai Lama
58200 Kuala Lumpur
Malaysia

DATED DEC 8TH 1988

THE UNIVERSITY OF ALBERTA
FACULTY OF GRADUATE STUDIES AND RESEARCH

The undersigned certify that they have read, and recommend to the Faculty of Graduate Studies and Research, for acceptance, a thesis entitled NON-INTRUSIVE OPTICAL FIBER TAPPING submitted by MNOON-YAN LOKE in partial fulfilment of the requirements for the degree of MASTER of SCIENCE.

J. N. McMullin
.....
Supervisor

W. J. Pitt
.....
C. L. Brown
.....
.....

Date.. DEC 8TH 1988

ABSTRACT

In this thesis, the modelling and experimental verification of losses and radiation patterns of a bent multimode fiber taking into account the modal power distribution are presented. It was found that for all experimental cases, the simulation model over-predicts the bending losses. A major contribution to the discrepancy was the strain induced on the fiber by the bend which in turn changes the refractive index of the fiber. With this induced strain, the effective radius of curvature was determined to be approximately 1.28 the induced radius of curvature. The introduction of R_{eff} reduces the simulation results to values more comparable to the experimental results. With the developed model, two prototypes to non-intrusively tap optical power from a live fiber have been successfully implemented. Not only do the prototypes provide a variable insertion loss feature, they are easy to install and remove without any damage to the fiber.

ACKNOWLEDGEMENTS

I would like to thank Dr. J. N. McMullin for his constant support, guidance and encouragement throughout this project. Also greatly appreciated is his derivation of the ray theory for bent optical fibers from the Hamiltonian equations of a photon. In addition, I would like to extend my sincere thanks to the following:

- the members of the examining committee.
- the staff of Alberta Telecommunications Research Centre
- Alberta Telecommunications Research Centre for the award of the ATRC Telecommunications Scholarship.
- Messrs. David Johnson and Keith Wilcox for their competent technical assistance, not forgetting the former for his Turbo Pascal software to enable writing to an external port of a P.C.
- Ms. Joanne Whalen for drawing some of the figures.
- Mr. Graham McKinnon of the AMC for the use of their facilities and wiring of the chip detectors.
- Messrs. Sharif Aktary, Jann Binder, Jeff Brown and Ms. Azmina Somani for their fruitful discussions.
- Mr. Kevin Jacobsen for his 0.825 μm single mode fiber setup.
- Mr. James Freeman for setting up the near-field pattern experiment and obtaining some results.
- Messrs. Herward Gans and Roman Lipiecki for fabricating all mechanical components especially the prototypes and their useful suggestions in the process.

Last but not least, my family and friends for their constant support and encouragement.

TABLE OF CONTENTS

CHAPTER	PAGE
1. INTRODUCTION.....	1
1.1 Introduction.....	1
1.2 Objective of the thesis.....	2
1.3 Organization of the thesis.....	4
2. RAY PROPAGATION IN A MULTIMODE GRADED-INDEX FIBER.....	5
2.1 Introduction.....	5
2.2 WKB Method.....	6
2.3 Rays in a straight graded-index fiber.....	13
2.4 Rays in a bent graded-index fiber.....	18
2.5 Rays in a bent constant index fiber.....	22
2.6 Reflection and refraction of a light ray.....	24
2.7 Power transmission and reflection at an interface.....	26
3. MODAL POWER DISTRIBUTION.....	31
3.1 Introduction.....	31
3.2 Relationship between MPD and near-field pattern (NFP).....	32
3.3 Measurement of the NFP.....	41
3.4 Ray distribution.....	44
4. COMPUTER SIMULATION.....	48
4.1 Introduction.....	48
4.2 Task of the simulation program.....	49
4.3 Structure of the simulation program.....	53
4.3.1 Generate initial data.....	53
4.3.2 Process GRIN Bend.....	55

4.3.3	Process Constant Bend I.....	55
4.3.4	Process Constant Bend II.....	56
4.3.5	Process GRIN Straight.....	56
4.3.6	Process Constant Straight.....	57
4.3.7	Interpolate.....	57
4.3.8	Interface.....	58
4.3.9	Transmission Coefficient.....	58
4.3.10	The Control Unit.....	58
4.4	Software for observing radiating patterns.....	60
5	COMPARISON OF EXPERIMENT AND THEORY.....	63
5.1	Introduction.....	63
5.2	Bending losses.....	64
5.2.1	Laser I at 0.825 μm	67
5.2.2	Laser at 1.3 μm	75
5.2.3	Laser II at 0.825 μm	86
5.2.4	Theoretical comparison with a lambertian source...	93
5.3	Radiation patterns.....	95
5.4	Discrepancy between experimental and theoretical results.....	102
5.4.1	Numerical accuracy of simulation.....	102
5.4.2	Possible existence of a doping barrier.....	104
5.4.3	Uncertainty of fiber parameters.....	107
5.4.4	Stress-optical effect.....	108
5.4.5	Measurement of the modal power distribution.....	115
6	PROTOTYPES.....	117

6.1	Introduction.....	117
6.2	Design considerations.....	117
6.3	Prototype I.....	120
6.4	Prototype II.....	125
7	SUMMARY.....	129
	REFERENCES.....	132
APPENDIX A	Ray propagation in a bent parabolic graded-index fiber.....	136
APPENDIX B	Ray propagation in a bent constant index media.....	142
APPENDIX C	Effect of stress on the ray propagation in a bent fiber.....	145
APPENDIX D	Detector data sheets.....	147
APPENDIX E	Corning fiber data sheets.....	150

LIST OF TABLES

TABLE	PAGE
5.1 Simulation results for $R = 7.125 \text{ mm}$, $\lambda = 0.825 \text{ }\mu\text{m}$ and modal power distribution of Fig. 5.4.....	71
5.2 Simulation results for $R = 8.125 \text{ mm}$, $\lambda = 0.825 \text{ }\mu\text{m}$ and modal power distribution of Fig. 5.4.....	72
5.3 Simulation results for $R = 9.125 \text{ mm}$, $\lambda = 0.825 \text{ }\mu\text{m}$ and modal power distribution of Fig. 5.4.....	73
5.4 Simulation results for $R = 10.125 \text{ mm}$, $\lambda = 0.825 \text{ }\mu\text{m}$ and modal power distribution of Fig. 5.4.....	74
5.5 Simulation results for $R = 7.125 \text{ mm}$, $\lambda = 1.3 \text{ }\mu\text{m}$ and modal power distribution of Fig. 5.14.....	82
5.6 Simulation results for $R = 8.125 \text{ mm}$, $\lambda = 1.3 \text{ }\mu\text{m}$ and modal power distribution of Fig. 5.14.....	83
5.7 Simulation results for $R = 9.125 \text{ mm}$, $\lambda = 1.3 \text{ }\mu\text{m}$ and modal power distribution of Fig. 5.14.....	84
5.8 Simulation results for $R = 10.125 \text{ mm}$, $\lambda = 1.3 \text{ }\mu\text{m}$ and modal power distribution of Fig. 5.14.....	85
5.9 Effects on simulation result for $\varphi = 30$ compared to Table 5.4 for $\varphi = 18$	103
5.10 Effects on simulation results for $(4m-1)$ combinations compared to Table 5.4 for m combinations.....	105
5.11 Effects on simulation results for $(4m-1)$ combinations and $\varphi = 30$ compared to Table 5.4 for m combinations and $\varphi = 18$	106
5.12 Comparison of experimental and theoretical results with numerical apertures of 0.2, 0.215 and 0.185.....	108
6.1 Positions and simulated tapping efficiencies for various radius of curvature.....	120

6.2	Performance of prototype I.....	125
6.3	Performance of prototype II.....	125
6.4	Performance of prototype II with 0.825 μm single mode fiber.....	128

LIST OF FIGURES

FIGURE	PAGE
2.1 Graphical representation of the WKB solution. The field is oscillatory between r_0 and r_1	9
2.2 Existence of leaky modes. Power can tunnel through r_0 and r_2	9
2.3 Refracting modes. The outer caustic does not exist.....	11
2.4 Mode space diagram.....	14
2.5 Projection of a guided ray's path.....	19
2.6 A Refracting ray.....	19
2.7 Rotating local coordinate system.....	20
2.8 Shift in equilibrium position of a ray in a bend.....	23
2.9 At interface, incident ray \vec{k}_1 , refracted ray \vec{k}_2 and reflected ray \vec{k}_3	25
2.10 Converting to radial coordinates.....	25
2.11 Transmission and reflection coefficients for both polarizations where $n_1 = 1.453$ and $n_2 = 1.54$	29
2.12 Transmission and reflection coefficients for both polarizations where $n_1 = 1.53$ and $n_2 = 1.0$	29
2.13 Transmission and reflection coefficients for both polarizations where $n_1 = 1.53$ and $n_2 = 1.54$	30
3.1 Longitudinal fourier spectrum of the electric field in the fiber when laser source is purely monochromatic.....	35
3.2 A more realistic longitudinal fourier spectrum.....	35
3.3 Near-field pattern for all rays belonging to mode m to $m+\Delta m$	38
3.4 A typical near-field pattern.....	40

3.5	The modal power distribution for the above near-field pattern.....	40
3.6	Possible scans of the near-field pattern using the conventional pinhole method.....	42
3.7	Utilization of slits to scan the near-field pattern.....	42
3.8	Coordinate system used in scanning the near-field pattern using a slit.....	43
3.9	Experimental setup to magnify and scan the near-field pattern.....	43
3.10	Typical x , y positions of rays.....	47
3.11	Typical k_x , k_y parameters of rays.....	47
4.1	Possible paths of a refracting ray in a bent fiber.....	50
4.2	Theoretical power remaining as a function of normalised distance z/a with a measured around the axis of the core.....	52
4.3	Structure of the simulation program.....	54
4.4	Algorithm of the control unit.....	59
4.5	Coordinate system used in observing the radiating patterns....	61
4.6	Computer simulated radiation pattern.....	61
5.1	Experimental setup to measure bending losses.....	65
5.2	Experimental and curve-fitted results from the slit experiment for the first of the two $0.825 \mu\text{m}$ laser sources....	68
5.3	The near-field pattern derived from Fig. 5.2.....	69
5.4	The modal power distribution derived from Fig. 5.3.....	69
5.5	Experimental and theoretical bending losses for MPD in Fig. 5.4. Experimental uncertainty of 15% in all loss measurements.....	70
5.6	Exploded comparison from Fig. 5.5.....	70

5.7	Experimental and curve-fitted results from the slit experiment for the first of the two 0.825 μm laser sources. Fiber was wrapped around a mandrel.....	76
5.8	The near-field pattern derived from Fig. 5.7.....	77
5.9	The modal power distribution derived from Fig. 5.8.....	77
5.10	Experimental and theoretical bending losses for MPD in Fig. 5.9. Experimental uncertainty of 15% in all loss measurements.....	78
5.11	Exploded comparison from Fig. 5.10.....	78
5.12	Experimental and curve-fitted results from the slit experiment for the 1.3 μm laser source.....	79
5.13	The near-field pattern derived from Fig. 5.12.....	80
5.14	The modal power distribution derived from Fig. 5.13.....	80
5.15	Experimental and theoretical bending losses for MPD in Fig. 5.14. Experimental uncertainty of 15% in all loss measurements.....	81
5.16	Exploded comparison from Fig. 5.15.....	81
5.17	Experimental and curve-fitted results from the slit experiment for the 1.3 μm laser source. Fiber was wrapped around a mandrel.....	87
5.18	The near-field pattern derived from Fig. 5.17.....	88
5.19	The modal power distribution derived from Fig. 5.18.....	88
5.20	Experimental and theoretical bending losses for MPD in Fig. 5.19. Experimental uncertainty of 15% in all loss measurements.....	89
5.21	Exploded comparison from Fig. 5.20.....	89
5.22	Experimental and curve-fitted results from the slit experiment for the second of the two 0.825 μm laser sources...	90
5.23	The near-field pattern derived from Fig. 5.22.....	91
5.24	The modal power distribution derived from Fig. 5.23.....	91

5.25	Experimental and theoretical bending losses for MPD in Fig. 5.24. Experimental uncertainty of 15% in all loss measurements.....	92
5.26	Exploded comparison from Fig. 5.25.....	92
5.27	Theoretical comparison with a lambertian source at 0.825 μm	94
5.28	Theoretical comparison with a lambertian source at 1.3 μm	94
5.29	Scanning of the radiation pattern from a bent fiber.....	96
5.30	Power as a function of y for $z = 8$ mm (see coordinate system Fig. 4.5) with $R = 7.125$ mm and $n_{\text{fluid}} = 1.50$	98
5.31	Power as a function of y for $z = 11$ mm (see coordinate system Fig. 4.5) with $R = 10.125$ mm and $n_{\text{fluid}} = 1.50$	98
5.32	Simulated radiation pattern for the same case as in Fig. 5.30.....	99
5.33	Simulated radiation pattern for the same case as in Fig. 5.31.....	99
5.34	Power as a function of y for $z = 8$ mm with $R = 7.125$ mm and $n_{\text{fluid}} = 1.538$	100
5.35	Power as a function of y for $z = 11$ mm with $R = 10.125$ mm and $n_{\text{fluid}} = 1.538$	100
5.36	Simulated radiation pattern for the same case as in Fig. 5.34.....	101
5.37	Simulated radiation pattern for the same case as in Fig. 5.35.....	101
5.38	Analysis of stress in a bent optical fiber.....	109
5.39	Experimental and revised theoretical bending losses for MPD in Fig. 5.4.....	112
5.40	Experimental and revised theoretical bending losses for MPD in Fig. 5.9.....	112
5.41	Experimental and revised theoretical bending losses for MPD in Fig. 5.14.....	113

5.42	Experimental and revised theoretical bending losses for MPD in Fig. 5.19.....	113
5.43	Experimental and revised theoretical bending losses for MPD in Fig. 5.24.....	114
6.1	Simulated radiation pattern for R = 7.125 mm with the detector at z = 5.5 mm and y = 7 mm.....	121
6.2	Simulated radiation pattern for R = 8.125 mm with the detector at z = 5.5 mm and y = 8 mm.....	121
6.3	Simulated radiation pattern for R = 9.125 mm with the detector at z = 5.5 mm and y = 9 mm.....	122
6.4	Simulated radiation pattern for R = 10.125 mm with the detector at z = 5.5 mm and y = 10 mm.....	122
6.5	Discs with different radius of curvature. They are constructed with a fixed z-origin and varying y-origin respect to the detector.....	123
6.6	Prototype I with the different discs magnified 1.8X.....	124
6.7	Basic operating principal of prototype II.....	126
6.8	Prototype II magnified 1.8X.....	127

Symbols and Acronyms

E	1. electric field 2. Young's modulus (see Chapter 5)
n_1	refractive index of the axis of the core
n_2	refractive index of the cladding
Δ	relative change in refractive index
Q	rate of relative change in refractive index
a	radius of the core
$n(r)$	refractive index profile of the core
r	radial position
μ	radial mode number
ν	1. azimuthal mode number 2. Poisson's ratio (see Chapter 5)
k_0	free space wave propagation constant
λ_0	free space wavelength
ω	free space angular frequency
c	speed of light in free space
v	speed of light on the axis of the core
V	normalized frequency parameter
m	principal mode number
M	maximum principal mode number of guided modes
\hbar	Planck's constant over 2π
τ	normalised time variable
R	radius of the bend
p_{ij}	strain-optical coefficients
ϵ	strain

σ	stress
WKB	Wentzel, Kramers, Brillouin
N.A.	numerical aperture
$N(r)$	near-field pattern
$Q(m)$	total power of the near-field pattern
$P(m)$	power of principal mode number m
MPD	modal power distribution
SMPD	steady-state modal power distribution
DMG	degenerate mode group

Chapter 1

Introduction

1.1 Introduction

There are many potential applications where only small amounts of light need to be extracted from an optical fiber, such as broadcasting to a large number of nodes, optical clock distribution in synchronous optical local area networks, and CATV distribution. Conventional fiber optic taps require one [1] or two [2] connectors in the optical fiber bus necessitating the disruption of the system when a tap is removed or connected. The tapping ratios of these taps are typically fixed and cannot be adjusted to accommodate the change in the power level in the fiber or the change in desired tapping power. Furthermore, connector losses of 0.2 dB to 2.0 dB inherent in these tap designs limit the number of taps that can be connected in a fiber distribution system.

A new connectorless tap was proposed by Miller [3]. This type of tap is attractive, as disruption of the signal to install or remove a tap is eliminated. This tap is based on the idea of introducing power into the jacket by inducing a bend in the fiber with a bent tube. Power in the jacket is then optically coupled to the exterior by using index matching fluid. The coupled power is then guided by the tube onto a detector. However the tapping ratio is always fixed for a particular tap unless a new tap with a different angle of bend is applied. Furthermore, the overall tapping efficiency is only in the 10-30% range. A recent paper presented at OFC 1988 [4] proposed a low-loss high-impedance integrated fiber-optic tap. This new tap not only has the advantage of being variable in terms of tapping ratio but

is also compact. This method is based on the idea of exciting cladding modes with a microbender and the cladding modes are tapped via a circular symmetric notch etched into the cladding. The tapped light is collected by an integrated photodetector which results in a highly proficient device in terms of tapping efficiency. However, this tap has its drawbacks too. Not only is it necessary to remove the jacket of the fiber, but etching into the cladding is also required. Damage to the fiber is inherent in this process.

In the above proposed taps, no theoretical derivations on the amount of bending losses are provided. All papers are purely experimental. However, there are other published papers on theoretical bending losses for multimode fibers [5]-[7] and single mode fibers [8]-[11]. Surprisingly enough, no published papers on the comparison between the published theories and experimental results have been found except for a brief statement on the major discrepancy between the two [12]. Furthermore in the multimode fiber cases, no consideration is given as to which modes are propagating and their individual power in the derivation. The common case is to assume that a lambertian source is used to excite the entire fiber.

1.2 Objective of the thesis

The primary objective of this thesis is to design a variable optical fiber tap with tapping ratios in the range of 1-10%, high collecting efficiency with easy installation and removal procedures that do not damage the fiber or disrupt the system. The design of the tap will be based on the idea of detecting the light radiated from the fiber at an induced bend. The idea is similar to Ref. [3] however

attempts will be made to improve the collecting efficiency and make the tapping ratios variable.

Prior to the development of a prototype, the properties of light propagating in a bent fiber should be understood so that the variation of the bending loss and radiation pattern can be predicted from a knowledge of the bend radius and the material properties of the fiber. Furthermore, in a multimode fiber, many modes propagate depending on the launching conditions and the amount of power lost will vary from mode to mode. Hence, the bending loss also depends on the power distribution among the propagating modes (modal power distribution). On the road to fulfilling the primary objective, the following secondary objectives must be met:

1. develop a simulation program to predict bending losses for various modal power distribution.
2. develop capabilities to measure the modal power distribution in an actual fiber with arbitrary launching conditions.
3. perform measurements of bending losses and radiation patterns.

The major portion of the thesis deals with these secondary objectives. The initial motivation is to use multimode fiber as it is more commonly used in applications that involve short distance transmission like the local area network. However, testing with single mode fiber on the final prototype will also be done.

1.3 Organization of the thesis

In Chapter 2, the ray theory in multimode fibers is presented. A full theoretical analysis on ray propagation is provided taking into account the various regions of a graded-index fiber and the effects on the ray as it propagates from region to region.

In Chapter 3, the modal power distribution problem is addressed. A short survey of published papers on various methods in obtaining the modal power distribution is presented with an elaboration on the chosen method.

In Chapter 4, the structure and algorithm in developing the simulation program is discussed. Other software developed to observe simulated radiation patterns is also described.

In Chapter 5, experimental and theoretical results on bending losses and radiation patterns are presented. Discussions on the discrepancies are also presented.

In Chapter 6, the designs and test results of the prototypes are presented.

In Chapter 7, a summary of the entire research project with a major emphasis on the comparison between theoretical and experimental results are presented. The performances of the prototype are recapitulated and suggestions of future research work are made.

Chapter 2

Ray Propagation in a Multimode Graded-Index Fiber

2.1 Introduction

Optical fibers for communication purposes are grouped into two classes: multimode and single mode fibers. As the name suggests, single mode fibers are capable of supporting only one mode, namely the HE_{11} mode when the criterion of $V^1 < 2.405$ is met. To meet the criterion, the maximum size of the core is restricted to approximately $10\mu\text{m}$. A pulse propagating in a single mode fiber broadens only very slightly due to the dispersive properties of the fiber material and the inherent dispersion of the waveguiding process [13]. Multimode fibers on the other hand, have larger cores and are capable of supporting many modes. When the power is initially launched in a short pulse, it is distributed among many modes, each of which travels with a slightly different group velocity. The receiver at the other end thus receives many different, overlapping pulses each carried by a different mode. Thus a multimode fiber causes the pulse to broaden much more than in a single mode fiber. Consequently, multimode fibers have a much more limited information carrying capacity than single mode fibers for a given distance.

In terms of channel capacity, multimode fibers cannot compete with single mode fibers. However, there are attractive features of multimode fibers. For example, the larger core diameter, approximately

$V^1 = \frac{2\pi}{\lambda_0} a (n_1^2 - n_2^2)^{1/2}$ is the normalized frequency parameter. For the other variables, refer to eqn. (2.12).

50 μm , facilitates the splicing and handling of the fiber. Furthermore, it is easier to couple light into a multimode fiber. Multimode fibers are being used in applications which do not involve long distance transmission or where high channel capacity is not important.

This chapter deals with light propagation in a multimode graded-index optical fiber. The first section deals with the WKB method. It is presented in a summarized form to provide some insight into the conditions that lead to various classification of modes. It is followed by the derivation of ray equations for a straight fiber in section 2.3. Then in sections 2.4 and 2.5, the extension is made to a bent fiber for two different index profiles, parabolic graded-index for the core and step index for the cladding/jacket. The effects of a ray passing through an interface are discussed in terms of refracting angles and power transmission in sections 2.6 and 2.7 respectively.

2.2 WKB method

Unlike the case of a step-index fiber where a modal analysis based on solving Maxwell's equations can be performed, any general analysis to obtain solutions to the electromagnetic wave equations in a graded-index fiber will soon become intractable. The most widely used analysis of modes in a graded-index fiber is an approximation based on the WKB method from quantum mechanics [14]. The general approach to this method is to recognize the fact that the refractive index of the core is slowly varying with the radius. In this section, the WKB method will be very briefly summarized. The full mathematical approximation and derivation can be obtained from numerous books [13, 15, 16]. The important result of the WKB method is the expression

for the modal propagation constant k_z , which is undetermined by ray theory.

The starting point of the WKB method is the wave equation in cylindrical coordinates (r, ϕ, z) :

$$\nabla^2 E + n^2(r) k_0^2 E = 0, \quad (2.1)$$

where $k_0 = \omega/c$ is the free space propagation constant. Mode solution of this form is sought

$$E = F(r) \begin{Bmatrix} \cos \nu \phi \\ \sin \nu \phi \end{Bmatrix} e^{-ik_z z} \quad (2.2)$$

introducing the azimuthal mode number ν , an integer, to ensure that E remains single valued as a function of ϕ . Substituting eqn. (2.2) into eqn. (2.1)

$$\frac{d^2 F}{dr^2} + \frac{1}{r} \frac{dF}{dr} + \left[n^2(r) k_0^2 - k_z^2 - \frac{\nu^2}{r^2} \right] F = 0 \quad (2.3)$$

where

$$k_\phi = \frac{\nu}{r}. \quad (2.4)$$

In the attempt to solve eqn. (2.3), the following trial solution is used

$$F(r) = A(r) e^{iS(r)}. \quad (2.5)$$

The exponent of the exponential function is found to be (under zero-order WKB approximation)

$$S(r) = \int_{r_0}^{r_1} \left[n^2(r) k_0^2 - k_z^2 - \frac{\nu^2}{r^2} \right]^{1/2} dr = \int_{r_0}^{r_1} g(r) dr. \quad (2.6)$$

If $g(r)$ is real, the exponent term in eqn. (2.5) is imaginary and the

solution is oscillatory between the two points $r = r_0$ and $r = r_1$ that are defined as solutions to

$$g(r) = n^2(r)k_0^2 - k_z^2 - \frac{\nu^2}{r^2} = 0. \quad (2.7)$$

In wave optics, the cylindrical surfaces of such radii are known as caustics. For values of r greater than the outer caustic radius, $r > r_1$, $g(r)$ becomes imaginary and eqn. (2.5) is real and assumes an evanescent behavior in that it decays exponentially. A graphical representation is shown in Fig. 2.1. As long as the solid curve, $n^2(r)k_0^2 - k_z^2$, lies above the dotted curve, ν^2/r^2 , oscillation occurs between the two points that the curves intersect.

Modes are guided as long as the outer caustic surface remains within the radius of the core, $r_1 < a$. Guided modes are divided into two categories, bound and leaky modes. If $n^2(r)k_0^2 - k_z^2$ remains negative for $r > a$, then there is no possibility of a third intersection and eqn. (2.5) will remain imaginary. The ray is bounded. Thus the condition for a bound ray can be expressed as

$$k_z > n_2 k_0 \quad (2.8)$$

where n_2 is the refractive index for $r > a$. Consider the other possibility of $k_z < n_2 k_0$ where the solid curve remains positive throughout as shown in Fig. 2.2. Here a third intersection occurs between the two curves resulting in eqn. (2.5) being real again at $r > r_2$. Since the function in eqn. (2.5) oscillates whenever it is real, the figure shows that the field will resume its oscillatory behaviour outside the third intersection point. In this case, energy can tunnel away from the core into the cladding. Modes with this characteristic are known as leaky modes. The boundary dividing bounded and leaky modes is given by

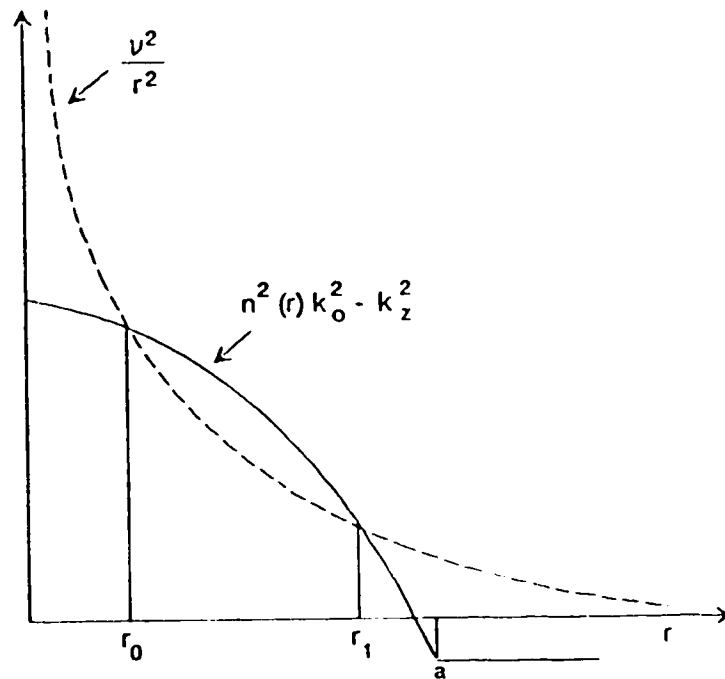


Fig. 2.1 Graphical representation of the WKB method solution. The field is oscillatory between r_0 and r_1

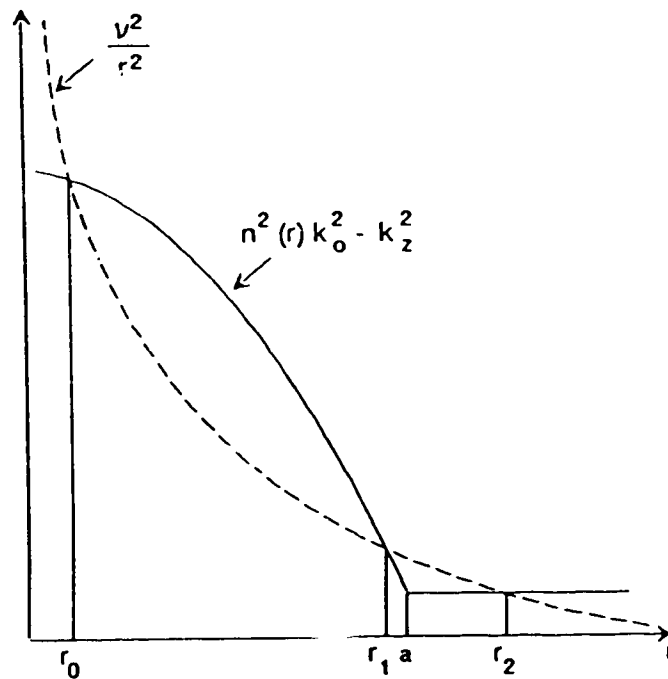


Fig. 2.2 Existence of leaky modes. Power can tunnel through r_1 and r_2

$$k_z = n_2 k_0 \quad (2.9)$$

The amount of energy lost due to this radiation depends on the length of the tunnelling region. Obviously for large values of ν , the region between r_1 and r_2 increases resulting in an infinitesimally small amount of loss and vice versa.

Consider the third possibility when the solid curve remains above the dotted curve for $r > r_0$. In this case, the outer caustic surface does not exist as shown in Fig. 2.3. Modes in this category are termed refracting modes. There is no outer confinement for the modes to oscillate within thus these modes are not guided by the core. The boundary that separates leaky and refracting modes is expressed as

$$k_z^2 = n_2^2 k_0^2 - \frac{\nu^2}{r^2} \quad (2.10)$$

To form a guided mode in the graded-index fiber, each wave associated with this mode must interfere constructively with itself in such a way as to form a standing-wave pattern in the radial cross-sectional direction. This imposes a requirement that the phase function $S(r)$ between r_0 and r_1 be multiples of π , so that

$$\mu\pi = \int_{r_0}^{r_1} \left[n^2(r) k_0^2 - k_z^2 - \frac{\nu^2}{r^2} \right]^{1/2} dr \quad (2.11)$$

where $\mu = 0, 1, 2, \dots$ is the radial mode number which counts the number of half periods between caustic surfaces. Eqn. (2.11) is the famous WKB expression for the propagation constant k_z of the guided modes.

The solution to the above equation for a parabolic graded-index profile

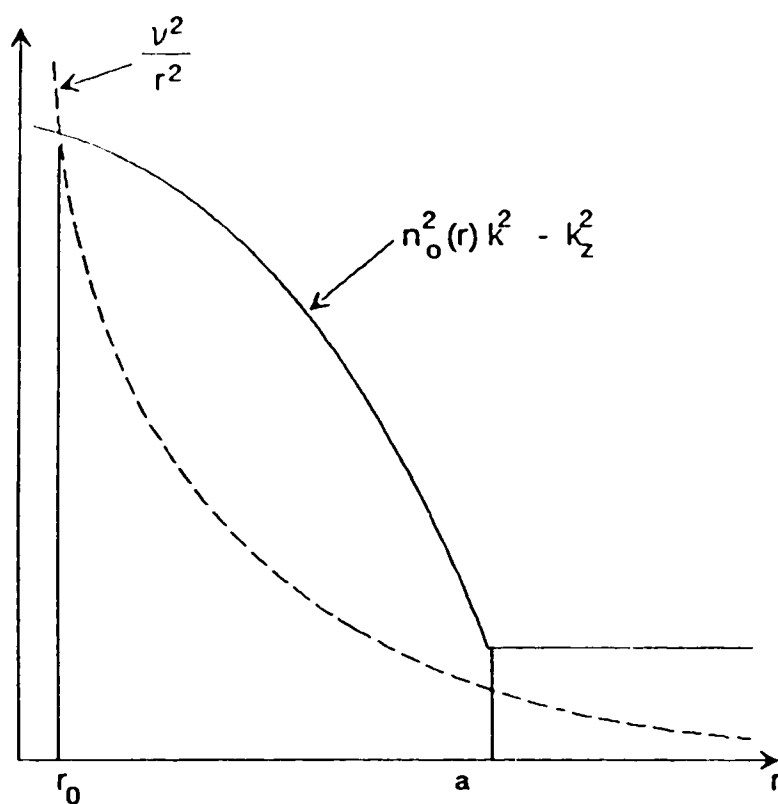


Fig. 2.3 Refracting modes. The outer caustic does not exist

$$n^2(r) = n_1^2 \left[1 - 2\Delta \frac{x^2 + y^2}{a^2} \right] \quad (2.12)$$

where

$$r^2 = x^2 + y^2$$

n_1 = axis index of refraction

$$\Delta = \frac{n_1 - n_2}{n_1}$$

n_2 = cladding index of refraction

a = radius of the core,

has been derived in Ref. [16] and will not be repeated here. The propagation constant for the modes in this case is

$$k_z^2 = n_1^2 k_o^2 - 2n_1 k_o \frac{\sqrt{2\Delta}}{a} (2\mu + \nu + 1). \quad (2.13)$$

The above equation is extremely useful and will be used extensively to determine the allowed propagation constant for a certain mode which is specified by the radial and azimuthal mode number. All modes that have the same propagation constant are grouped under the same principal mode number given by

$$m = 2\mu + \nu + 1. \quad (2.14)$$

To obtain a more pictorial view of the boundary conditions for bound, leaky and refracting modes in terms of the mode numbers, substitution of eqns. (2.9) and (2.10) into eqn. (2.13) is performed. For the bound and leaky mode boundary

$$\mu = \frac{1}{2} \left[\frac{1}{2} n_1 k_o a \sqrt{2\Delta} - \nu - 1 \right] \quad (2.15)$$

and boundary between leaky and refracting modes

$$\mu = \frac{\left[n_1 k_0 a \sqrt{2 \Delta} - \nu \right]^2 - 2 n_1 k_0 a \sqrt{2 \Delta}}{4 n_1 k_0 a \sqrt{2 \Delta}} . \quad (2.16)$$

A typical mode space diagram ($\nu\mu$ plane) is shown in Fig. 2.4. Each mode of the fiber, belonging to a pair of mode numbers ν and μ , is represented as a point in the mode space diagram. Each point represents four modes, because each mode can have a azimuthal mode dependence $\cos \nu\phi$ and $\sin \nu\phi$ and can exist in two mutually orthogonal polarizations. Modes of this kind are fourfold degenerate except when $\nu = 0$, that are doubly degenerate because $\sin \nu\phi$ no longer exist.

2.3 Rays in a straight graded-index fiber

An alternate method for theoretically studying the propagation characteristics of light in an optical fiber is the geometrical optics or ray-tracing approach. This method provides a good approximation to the guiding properties of optical fibers when the ratio of the fiber radius to the wavelength is large. This is known as the small wavelength limit. Although the ray approach is strictly valid only in the zero wavelength limit, it is relatively accurate and extremely valuable for non-zero wavelengths when the number of modes is large, that is, for multimode fibers. The advantage of the ray approach is that, compared to the exact electromagnetic wave analysis, it gives a more direct physical interpretation of the light propagation characteristics in an optical fiber.

It is known that there is a relation between the motion of wave packets, or photons, and the motion of a particle as described by the Hamiltonian mechanics [17]-[18]. The equation of motion of a particle

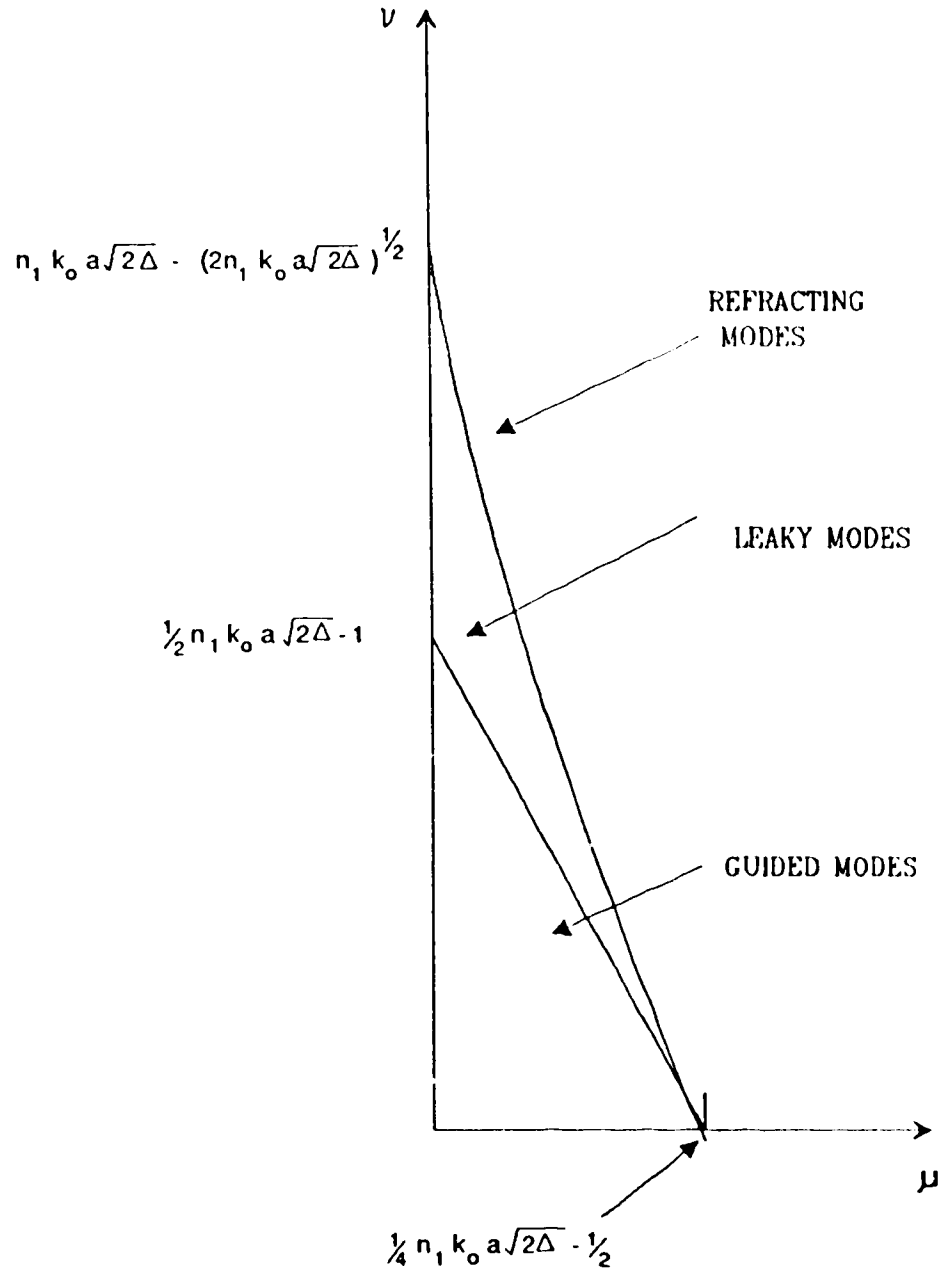


Fig. 2.4 Mode space diagram

is given by

$$\frac{d\vec{r}}{dt} = \nabla_{\vec{p}} H(\vec{r}, \vec{p}) \quad (2.17)$$

$$\frac{d\vec{p}}{dt} = - \nabla_{\vec{r}} H(\vec{r}, \vec{p}) \quad (2.18)$$

where \vec{r} is the position vector, \vec{p} is the momentum

$$\vec{p} = \hbar \vec{k} \quad (2.19)$$

and $\hbar = h/2\pi$ (h is Planck's constant). The Hamiltonian, $H(\vec{r}, \vec{p})$ is the energy of a photon,

$$H(\vec{r}, \vec{p}) = \hbar \omega(\vec{r}, \vec{k}), \quad (2.20)$$

where $\omega(\vec{r}, \vec{k})$ is the classical dispersion relation for the photons in the medium. In glass, this is approximately given by

$$\omega(\vec{k}, \vec{r}) = \frac{|\vec{k}| c}{n(\vec{r})} \quad (2.21)$$

where \vec{k} is the propagation vector. Using eqns. (2.17)-(2.21), the following equations can be derived

$$\frac{d\vec{r}}{dt} = \frac{c}{n(\vec{r})} \hat{k} \quad (2.22)$$

$$\frac{d\vec{k}}{dt} = \frac{k c}{n^2(\vec{r})} \nabla_{\vec{r}} n(\vec{r}). \quad (2.23)$$

Using eqn. (2.21), and the fact that the energy $\hbar\omega(\vec{k}, \vec{r})$ is a constant

$$\frac{d\vec{r}}{dt} = \frac{c^2 \vec{k}}{n^2(\vec{r}) \omega} \quad (2.24)$$

and

$$\frac{d\vec{k}}{dt} = \frac{\omega}{2 n^2(\vec{r})} \nabla_{\vec{r}} n^2(\vec{r}). \quad (2.25)$$

Eqs. (2.24) and (2.25) are the two general ray equations which describe the propagation of a ray in a medium with a refractive index profile $n(\vec{r})$. Differentiating eqn. (2.24) with respect to t and using eqn. (2.25) to eliminate $d\vec{k}/dt$ will result in the well-known second-order equation for the trajectory of a ray in a slowly-varying inhomogeneous medium (see for example eqn. (11.2-1) in [13] and eqn. (2.1.1) in [19]).

For a fiber core with a parabolic graded-index profile (see eqn. (2.12)),

$$\nabla_{\vec{r}} n^2(\vec{r}) = -2 \Delta n_1^2 \left[\frac{2x}{a^2} \hat{x} + \frac{2y}{a^2} \hat{y} \right]. \quad (2.26)$$

Defining a new time variable

$$dt = d\tau \frac{n^2(\vec{r})}{n_1^2} \quad (2.27)$$

and substituting eqns. (2.12) and (2.26) into eqns. (2.24) and (2.25) respectively,

$$\frac{d\vec{r}}{d\tau} = \frac{c^2 \vec{k}}{n_1^2 \omega} \quad (2.28)$$

$$\frac{d\vec{k}}{d\tau} = -\frac{2\Delta \omega}{a^2} \left[x \hat{x} + y \hat{y} \right]. \quad (2.29)$$

Consider the direction of propagation, z . From eqn. (2.29)

$$\frac{dk_z}{d\tau} = 0$$

$$\therefore k_z = \text{constant},$$

and from eqn. (2.28)

$$\frac{dz}{dr} = \frac{c^2 k_x}{n_1^2 \omega}$$

$$z = \frac{c^2 k_x}{n_1^2 \omega} r + C_1 \quad (2.31)$$

Similarly for the x direction

$$\frac{dx}{dr} = \frac{c^2 k_x}{n_1^2 \omega} \quad (2.32)$$

$$\frac{dk_x}{dr} = - \frac{2 \omega \Delta}{a^2} x \quad (2.33)$$

Differentiating eqn. (2.32) and using eqn. (2.33) to eliminate dk_x/dr , the solution of the second-order differential equation is

$$x = x_o \cos (Qvr) + \frac{v k_{ox}}{\omega Q} \sin (Qvr) \quad (2.34)$$

and vice versa

$$k_x = k_{ox} \cos (Qvr) - \frac{Q \omega x_o}{v} \sin (Qvr) \quad (2.35)$$

where

$$Q = \frac{\sqrt{2\Delta}}{a} \quad (2.36)$$

$$v = \frac{c}{n_1} \quad (2.37)$$

and x_o , y_o , k_{ox} and k_{oy} are the initial conditions. Applying the same procedure for the y direction

$$y = y_o \cos (Qvr) + \frac{v k_{oy}}{\omega Q} \sin (Qvr) \quad (2.38)$$

$$k_y = k_{oy} \cos(Qvr) - \frac{Q \omega y_o}{v} \sin(Qvr). \quad (2.39)$$

Hence using eqns. (2.30) (2.31) and (2.34) through (2.39), the propagation of a ray in a parabolic graded-index fiber can be fully described. For non-parabolic profiles, the two general ray eqns. (2.24) and (2.25) can be integrated numerically.

The projection of a ray path onto a fiber cross-section is shown in Fig. 2.5. It is observed that the trajectory of a guided ray is elliptical and confined to the region between r_0 and r_1 which are analogous to the caustic surfaces in the wave optics. In ray optics, the radii are known as turning points. They represent points at which the ray trajectory has no radial component. Bound and leaky rays exhibit the same oscillatory behaviour between the two turning points. On the other hand, refracting rays impinging on the core-cladding interface due to the absence of the outer turning point are refracted out of the core (refer to Fig. 2.6).

2.4 Rays in a bent graded-index fiber

Consider a ray entering a bend of radius of curvature R on the y - z plane as shown in Fig. 2.7. The derivation of the ray parameters as shown in Appendix A are based on the rotating local coordinate system [17]. In this coordinate system, the origin is situated on the axis of the bent fiber core. It rotates along this axis as the ray propagates. Hence, the x , y coordinates determined at any time will specify the location of the ray with respect to the axis of the core while the angle θ determines the location of the ray with respect to the origin

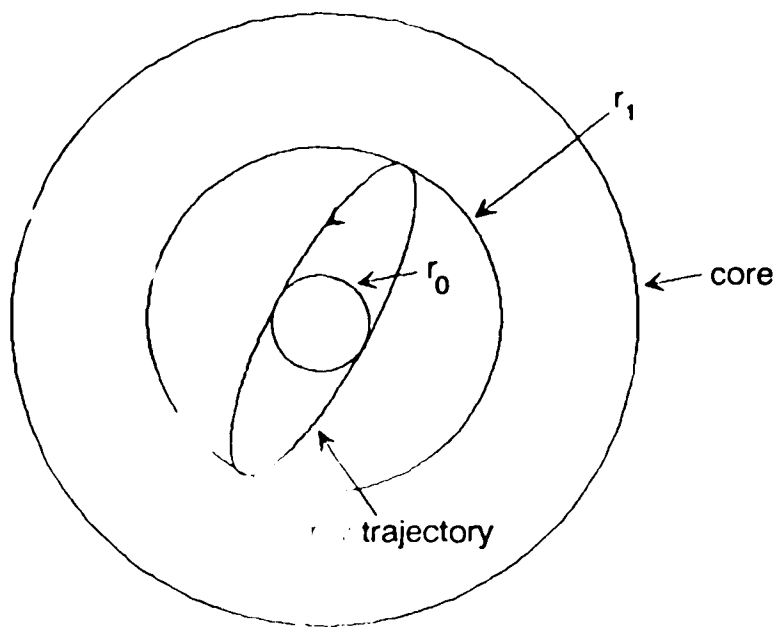


Fig. 2.5 Projection of a guided ray's path

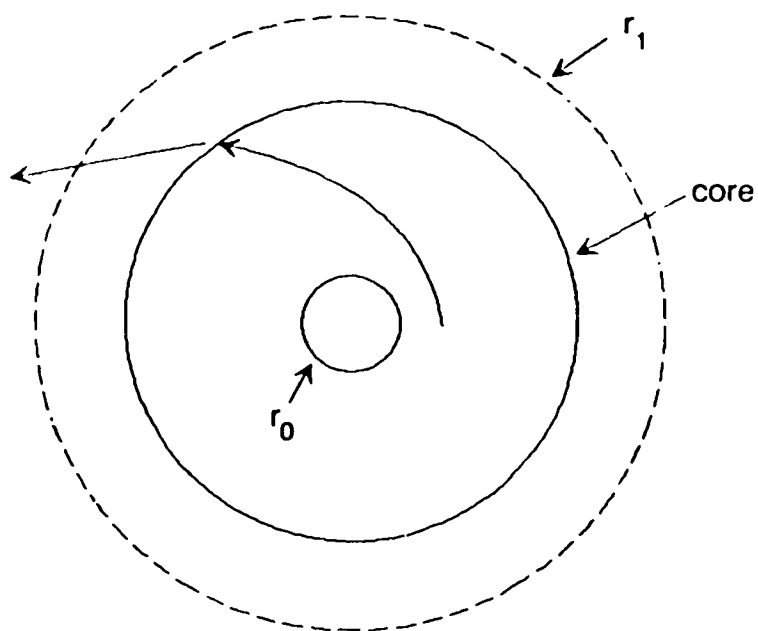


Fig. 2.6 A refracting ray

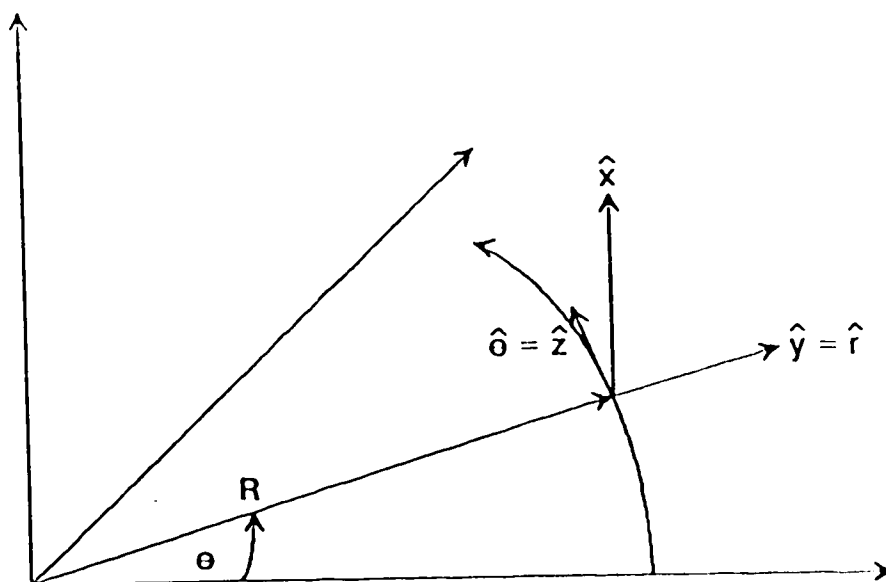


Fig. 2.7 Rotating local coordinate system

of the bend.

The approximate solutions for the ray propagation while in the bend are

$$x = x_o \cos(Qvr) + \frac{v k_{ox}}{\omega Q} \sin(Qvr) \quad (2.40)$$

$$k_x = k_{ox} \cos(Qvr) - \frac{Q \omega x_o}{v} \sin(Qvr) \quad (2.41)$$

$$y = \frac{k_{oz}^2 c^2}{(n_1 \omega Q)^2 R} + \frac{\gamma c}{n_1 \omega Q} \sin(Qvr + \phi) \quad (2.42)$$

$$k_y = \gamma \cos(Qvr + \phi) \quad (2.43)$$

where

$$\gamma^2 = \frac{k_{oz}^4 c^2}{(R n_1 \omega Q)^2} + k_{oy}^2 + \left[Q y_o n_1 \frac{\omega}{c} \right]^2 - \frac{2k_{oz}^2 y_o}{R} \quad (2.44)$$

and ϕ depends on the initial conditions. The on-axis distance travelled by the ray can be estimated by

$$z = \frac{rc}{n_1} \quad (2.45)$$

The equations describing the propagation of a ray in a bent multimode graded-index fiber are identical to the ones in Ref. [5].

Note that eqns. (2.40) and (2.41) are identical to eqns. (2.34) and (2.35). A bend in the y-z plane does not affect the x components of a ray. However in the y direction as compared to a straight fiber, the ray exhibits an oscillatory function offset from its equilibrium position by

$$\Delta y = \left(\frac{k_{ox} c}{n_1 \omega Q} \right)^2 \frac{1}{R} \quad (2.46)$$

The shift from its equilibrium position may be sufficient enough to cause the ray to leave the core, hence introducing bending losses. Note that the shift is inversely proportional to the radius of the bend. Fig 2.8 shows the trajectory of a ray onto a fiber cross-section, starting off in a straight fiber prior to the bend.

2.5 Rays in a bent constant index fiber

Rays that leave the core due to an induced bend will enter the cladding, a region that is of constant refractive index (n). In this section, the propagation of a ray in a bent constant index fiber will be presented. It is not only applicable to the cladding region but as well as to the jacket region as the latter is also of constant refractive index material but of slightly higher value. The derivation is compiled in Appendix B and is based on the same rotating coordinate system as in the previous section. Only relevant equations will be presented here.

The ray equations that describe the ray's propagation are:

$$x = -\frac{c^2 k_{ox}}{n^2 \omega} t + C_1 \quad (2.47)$$

$$k_x = \text{Constant} = k_{ox} \quad (2.48)$$

$$y = \left[\frac{v^2 k_{oz}^2}{2Rn^2 k_o^2} (t+C_2)^2 - \frac{\delta^2 R}{2k_{oz}^2} \right] \quad (2.49)$$

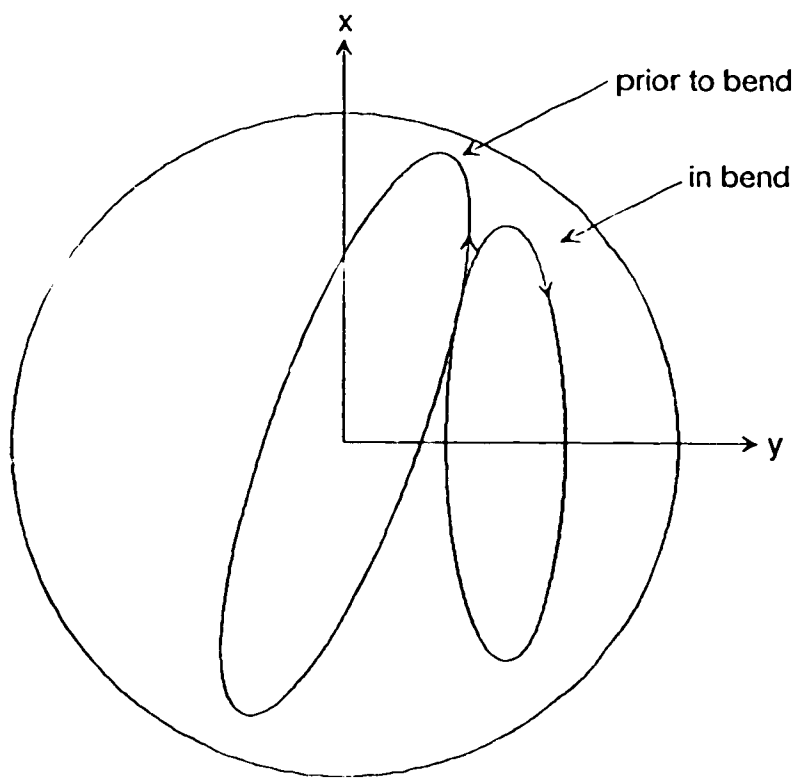


Fig. 2.8 Shift in equilibrium position of a ray in a bend

$$k_y = \frac{k_{oz}^2 \omega}{n^2 k_o^2 R} (t + C_2) \quad (2.50)$$

where

$$\delta^2 = k_{oy}^2 - \frac{2k_{oz}^2 y_o}{R} \quad (2.51)$$

and C_1 and C_2 depend on the initial conditions. To complete the set of equations, the estimated on-axis distance travelled around the bend while in the cladding or jacket ($z_2 - z_1$),

$$\frac{ct_1}{n} = \left[(x_2 - x_1)^2 + (y_2 - y_1)^2 + (z_2 - z_1)^2 \right]^{1/2} \quad (2.52)$$

where t_1 is the amount of time the ray spends in that region. All other variables with the subscript '1' and '2' denote the location of the ray when entering and leaving the region. Note that eqn. (2.49) does not indicate a linear relationship between position and time. This is due to the rotating frame of reference that is used in deriving the equations.

2.6 Reflection and refraction of a light ray

A light ray striking a plane surface between two media of different refractive indexes will be reflected and refracted; see Fig. 2.9. It is well-known that the reflection angle equals the incident angle and that the magnitude of the wave vectors is unchanged;

$$\theta_1 = \theta_3 \quad (2.53)$$

$$|\vec{k}_1| = |\vec{k}_3| \quad (2.54)$$

On the other, the refracted angle will depend on the refractive indices of the two media and the incident angle as stated by Snell's law,

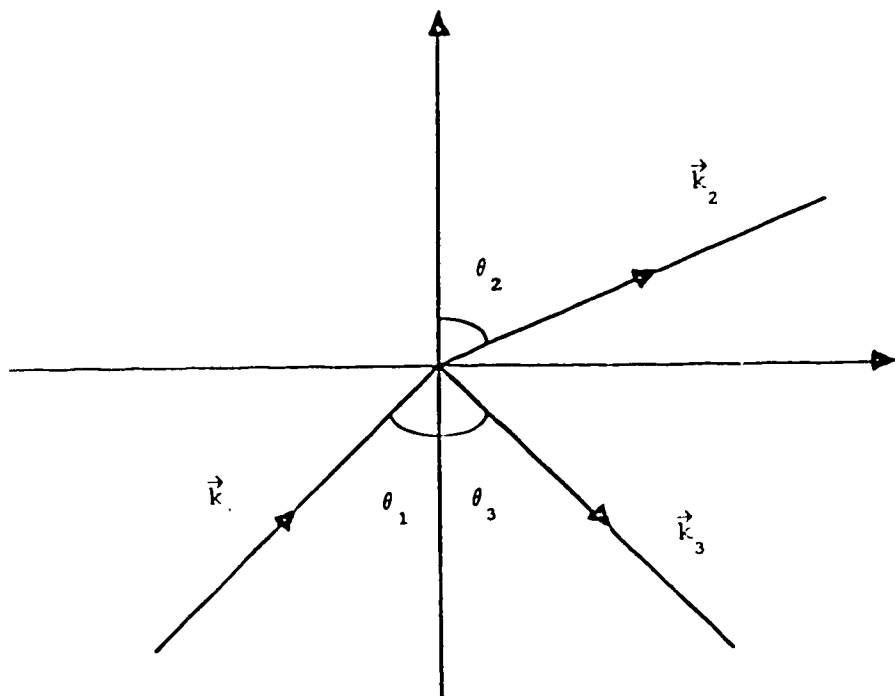


Fig. 2.9 At an interface, incident ray \vec{k}_1 , refracted ray \vec{k}_2 and reflected ray \vec{k}_3

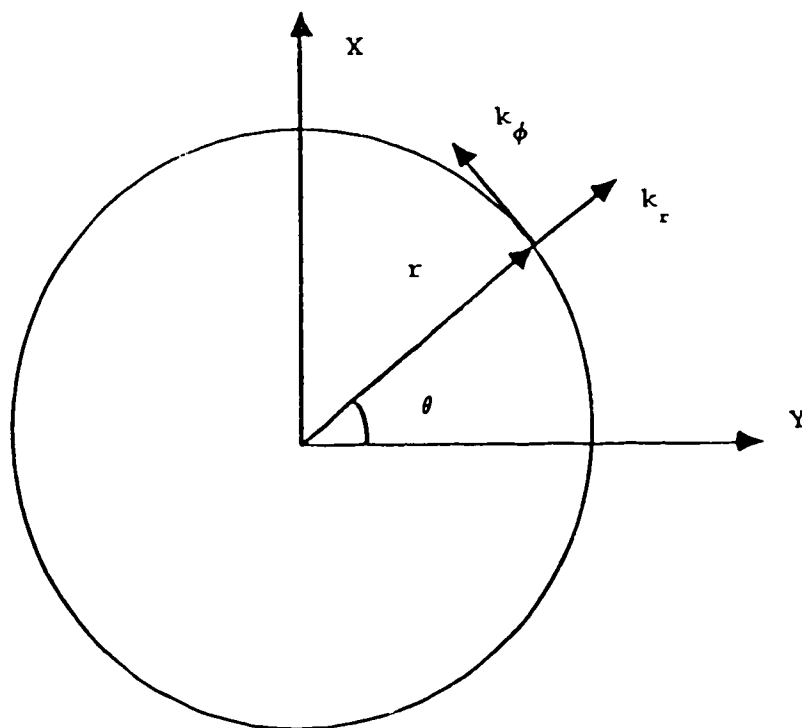


Fig. 2.10 Converting to radial coordinates

$$n_2 \sin \theta_2 = n_1 \sin \theta_1 . \quad (2.55)$$

The magnitude of the refracted wave vector is [20]

$$|\vec{k}_2| = |\vec{k}_1| \frac{n_2}{n_1} . \quad (2.56)$$

In determining the refracted wave vector in terms of the individual components (k_x, k_y, k_z) , it is easier to utilize the radial coordinate system as wave vectors parallel to the interface remain unchanged, Fig. 2.10, i.e.

$$k_{\phi_1} = k_{\phi_2} \quad (2.57)$$

$$k_{z_1} = k_{z_2} . \quad (2.58)$$

Expressing $|k_1|$ and $|k_2|$ in radial components and using eqns. (2.57) and (2.58)

$$k_{r2} = \left[\left[\left[\frac{n_2}{n_1} k_{r1} \right]^2 + (k_{\phi_1}^2 + k_{z_1}^2) \left[\left[\left[\frac{n_2}{n_1} \right]^2 - 1 \right] \right] \right]^{1/2} . \quad (2.59)$$

Note that $(|k_1| n_2/n_1)^2 > (k_{z_1}^2 + k_{\phi_1}^2)$ must hold otherwise total internal reflection occurs. This requirement is equivalent θ_1 being less than the critical angle (see Section 2.7).

2.7 Power transmission and reflection at an interface

In the previous section, the effects of a ray propagating through an interface are expressed in terms of angles and wave vectors. To conclude, the power transmission and reflection coefficients depending on the incident angle and refractive indices of the two media are presented. The derivation can be found in numerous books and only the final results are summarized here. The reflection coefficients

depending on the polarization are [15]

$$R_{\perp} = \frac{\left[n_1 \cos \theta_1 - \sqrt{n_2^2 - n_1^2 \sin^2 \theta_1} \right]^2}{\left[n_1 \cos \theta_1 + \sqrt{n_2^2 - n_1^2 \sin^2 \theta_1} \right]^2} \quad (2.60)$$

$$R_{\parallel} = \frac{\left[n_2 \cos \theta_1 - n_2/n_1 \sqrt{n_2^2 - n_1^2 \sin^2 \theta_1} \right]^2}{\left[n_2 \cos \theta_1 + n_2/n_1 \sqrt{n_2^2 - n_1^2 \sin^2 \theta_1} \right]^2} \quad (2.61)$$

while the transmission coefficients are

$$T_{\perp} = \frac{4n_1 \cos \theta_1 \sqrt{n_2^2 - n_1^2 \sin^2 \theta_1}}{\left[n_1 \cos \theta_1 + \sqrt{n_2^2 - n_1^2 \sin^2 \theta_1} \right]^2} \quad (2.62)$$

$$T_{\parallel} = \frac{4n_1 \cos \theta_1 \sqrt{n_2^2 - n_1^2 \sin^2 \theta_1}}{\left[n_2 \cos \theta_1 + n_2/n_1 \sqrt{n_2^2 - n_1^2 \sin^2 \theta_1} \right]^2} \quad (2.63)$$

The angle θ_1 is the angle the ray trajectory (k_x, k_y, k_z) makes with the radial distance (x, y) at the interface

$$\theta_1 = \cos^{-1} \left[\frac{k_x x + k_y y}{(x^2 + y^2)^{1/2} (k_x^2 + k_y^2 + k_z^2)^{1/2}} \right] \quad (2.64)$$

If this angle exceeds the critical angle defined as

$$\theta_c = \sin^{-1} \left(\frac{n_2}{n_1} \right) , \quad (2.65)$$

total internal reflection will occur. For commercially available

fibers, the refractive index of the cladding at $0.825 \mu\text{m}$ is roughly 1.453 and they are coated with a primary and secondary jacket with refractive indices of around 1.54 and 1.53 respectively. Figs. 2.11 and 2.12 depict typical transmission and reflection coefficients for both polarization of rays passing through the cladding/primary jacket and secondary jacket/air interface respectively. In the latter figure, for the rays with $\theta_1 > \theta_c$ (40.8°), total internal reflection will occur. This case is not desirable as for optimum collection efficiency, the power lost from the core should leave the fiber without any attenuation. A majority of rays hitting this interface will exceed the critical angle as k_z is typically much larger than k_x and k_y . Ideally, the exterior should be of the same or close to the refractive index as the secondary jacket. Fig. 2.13 depicts the situation of an external refractive index of 1.54. Note that in Figs. 2.11 and 2.13 the plots are very similar for either polarization. This is due to the very small refractive index difference between the two corresponding media. Hence, it is reasonable to use either equation for all rays.

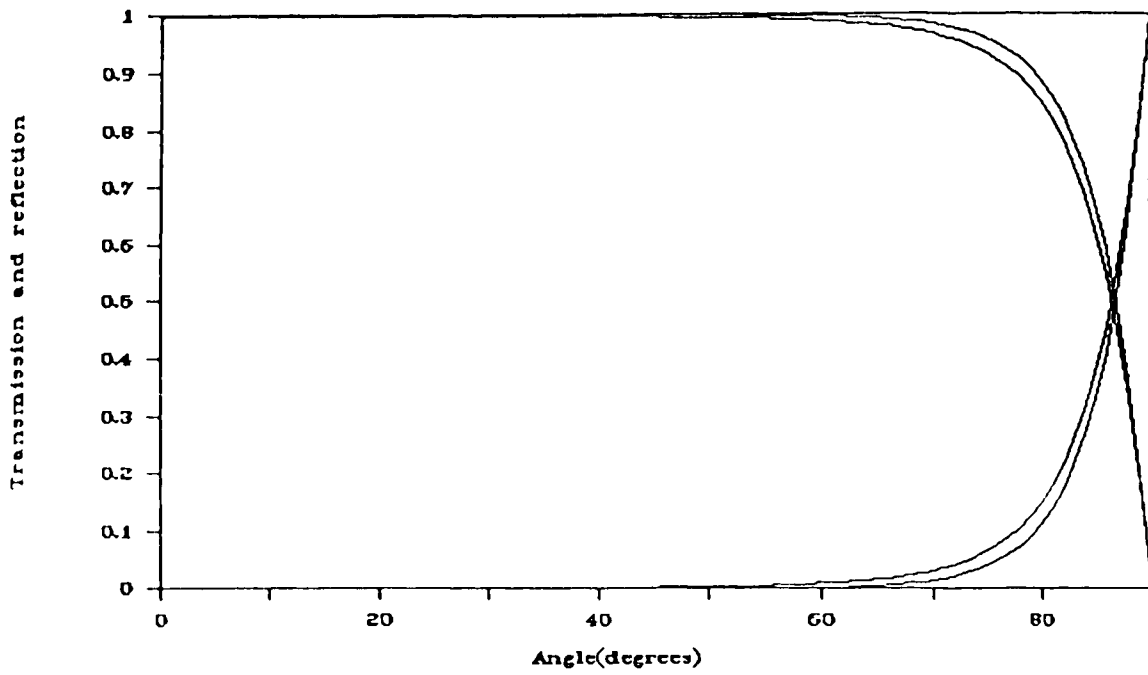


Fig. 2.11 Transmission and reflection coefficients for both polarizations where $n_1 = 1.453$ and $n_2 = 1.54$.

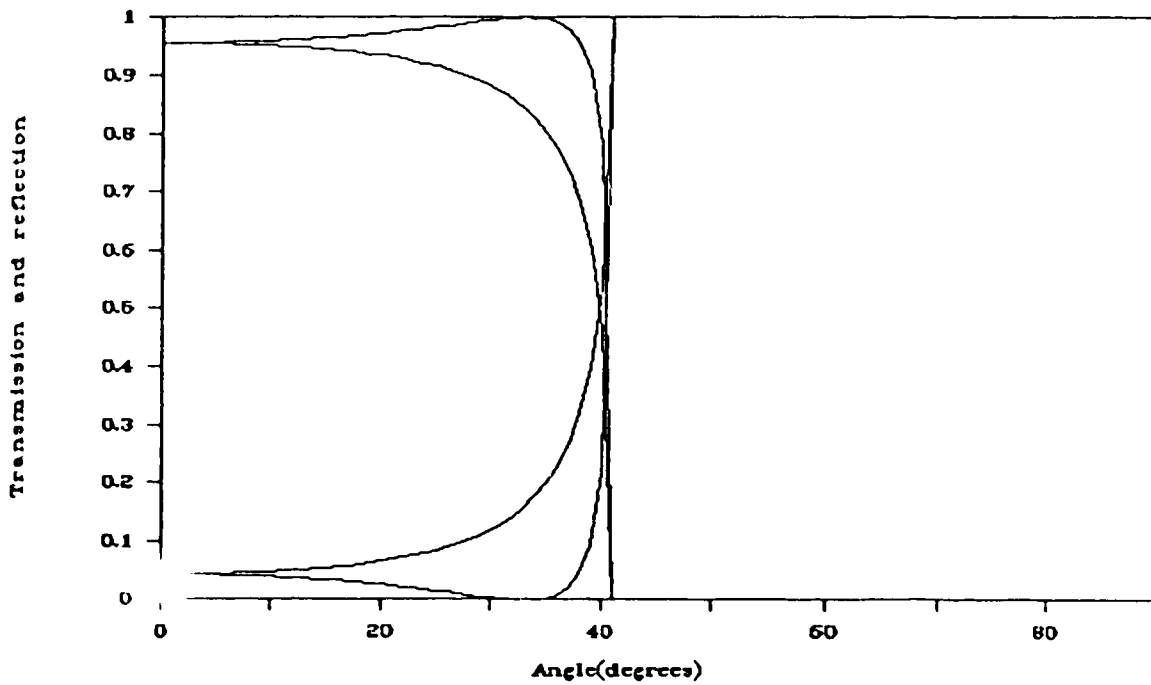


Fig. 2.12 Transmission and reflection coefficients for both polarizations where $n_1 = 1.53$ and $n_2 = 1.0$.

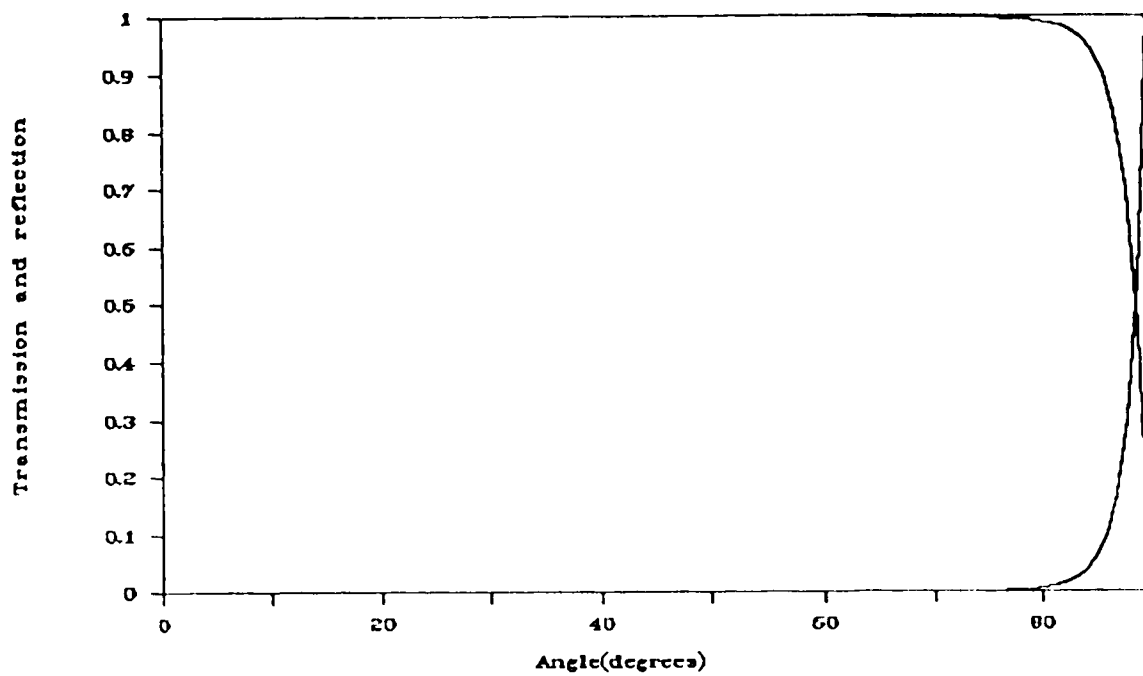


Fig. 2.13 Transmission and reflection coefficients for both polarizations where $n_1 = 1.53$ and $n_2 = 1.54$

Chapter 3

Modal Power Distribution

3.1 Introduction

In multimode optical fiber systems, the modal power distribution (MPD) which specifies the amount of power propagating in each of the individual fiber mode affects the fiber bending losses. The MPD in turn depends substantially on the manner in which the power is being launched into the fiber. Different launching conditions (axial offsets, beam width, etc.) have been shown to excite different modes in a graded-index fiber [21]-[23]. Moreover, the MPD is also distance dependent. There are typically several hundred modes in a multimode fiber, each propagating with different loss and velocity. The higher order modes (modes of higher principal mode number) attenuate faster than the lower order modes. Mode mixing also occurs causing power to shift from mode to mode. Hence, experimental results will differ when performed at different locations along the fiber due to the variations in MPD.

A steady-state modal power distribution (SMPD) is established when the mechanisms of differential mode attenuation and mode coupling are in equilibrium. This implies that MPD remains constant along the fiber. Since the stable equilibrium state is a function of fiber propagation mechanisms which in turn are strongly dependent on the fiber parameters, the SMPD is independent of the launched power distribution and a unique steady-state condition characteristic of all fibers does not exist [24]. In modern low-loss fiber, SMPD is reached only after several kilometers [25]. To avoid using long fibers,

various other techniques have been proposed to approximate SMPD near the fiber input:

- by using restricted numerical aperture and spot size
- by means of mode filters
- by means of mode scramblers.

A comparative study of these techniques was done in Ref. [25]. When performing experiments to characterize the fiber parameters, it is imperative that the fiber has obtained its SMPD. However, in this case it isn't so as one of the objectives of this thesis is to estimate the bending losses for an arbitrary MPD.

The relationship between the near-field pattern and the MPD is derived in the first section. Section 3.3 deals with the theoretical and experimental aspects of using slits instead of the conventional pin hole method in obtaining the near-field pattern. The chapter concludes with the problem of assigning the number of rays for each mode and the power per ray.

3.2 Relationship between MPD and near-field pattern (NFP)

In step-index fibers, the mode number corresponds approximately to the propagation angle of the light. Hence, the MPD can be instantly obtained by measuring the far-field pattern (FFP) [26]. However, this simple relationship is not applicable to a multimode graded-index fiber since a mode cannot generally be identified with its propagation angle as it changes during the course of travel [27].

This led to the derivation of the relationship between the NFP and MPD [27]. Further calculations followed which was extended to

arbitrary refractive index profile functions [28]. In Ref. [29], a new method was proposed and implemented experimentally where the MPD was obtained by numerically processing the measured Fraunhofer diffraction patterns of the NFP. This method is similar to Ref. [27] except for the fact that the NFP was measured using circular slits. The relationship between the NFP and MPD derived by the authors mentioned above is based on the assumption that the MPD is not a function of the azimuthal mode number ν . This implies that the FFP and NFP are azimuthally symmetric [30]. A derivation relating the NFP and FFP to the MPD was later done [31] without the assumption of azimuthal symmetry made by the previous authors. It was concluded that for a given MPD, a unique NFP and FFP can be obtained. However, if the NFP and FFP are determined, there are an infinite number of solutions for the MPD. With the assumption of azimuthal symmetry, a unique MPD can be obtained from a given NFP or FFP. So for practical applications, the suggestion has been made to determine the MPD from both the NFP and FFP with that assumption and compare the two distributions [31]. If both results coincide and the fiber is non-parabolic, the assumption is verified. The assumption cannot be verified in the parabolic graded-index fiber case because a direct relationship exists between the NFP and FFP [31].

Despite the skepticism concerning the validity of the assumption, the derived relationship between the NFP and MPD [27] is widely accepted by other authors [25, 28, 32]. Unless a new method is proposed and implemented experimentally, one has to proceed with this assumption.

The relationship between the NFP and MPD derived in this section

is similar to Ref. [27] but simpler. The derivation is based on the mode-continuum approximation that was first introduced in Ref. [33]. Recall eqn. (2.13)

$$k_z^2 = n_1^2 k_0^2 - 2n_1 k_0 \frac{\sqrt{2\Delta}}{a} (2\mu + \nu + 1). \quad (2.13)$$

Using eqn. (2.14) and rewriting eqn. (2.13)

$$k_z^2 = n_1^2 k_0^2 \left(1 - 2\Delta \frac{m}{M} \right) \quad (3.1)$$

where M is the maximum principal mode number for a guided mode

$$M = \frac{n_1 k_0 a \sqrt{2\Delta}}{2}. \quad (3.2)$$

For discrete values of m , the propagation constants of the discrete modes are given by eqn. (3.1). The spacing between adjacent modes is [19]

$$\Delta k_z \approx \frac{\sqrt{2\Delta}}{a}. \quad (3.3)$$

Fig. 3.1 depicts the longitudinal Fourier spectrum of the electric field for the case where the source used to excite the fiber is purely monochromatic [34]. However in a realistic situation, the source has a finite linewidth resulting in a different longitudinal Fourier spectrum of the electric field as shown in Fig. 3.2. If the linewidth $\delta\lambda$ of the source is sufficiently large that the corresponding width δk_z of each mode in the k_z space exceeds the mode spacing Δk_z , the modes within the fiber will constitute a continuum. The mode-continuum approximation is valid if the source satisfies the following inequality [34]

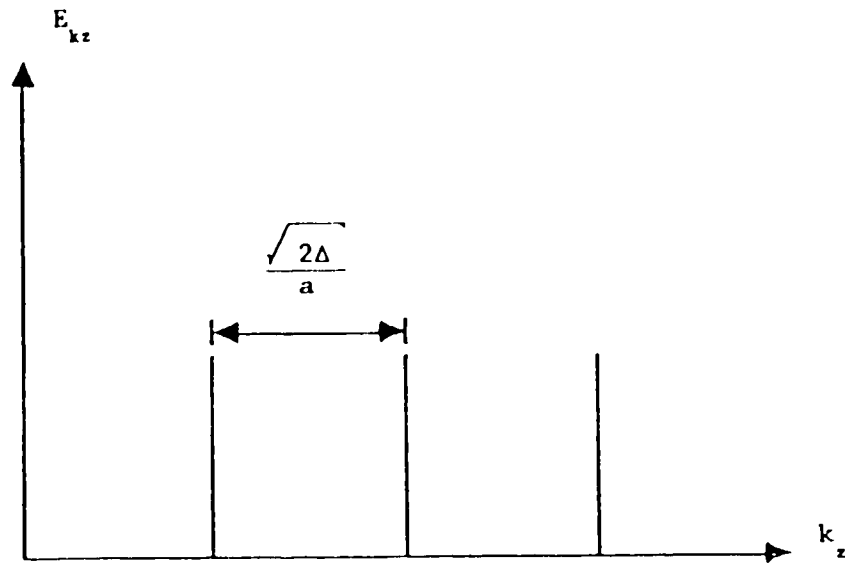


Fig. 3.1 Longitudinal Fourier spectrum of the electric field in the fiber when the laser source is purely monochromatic

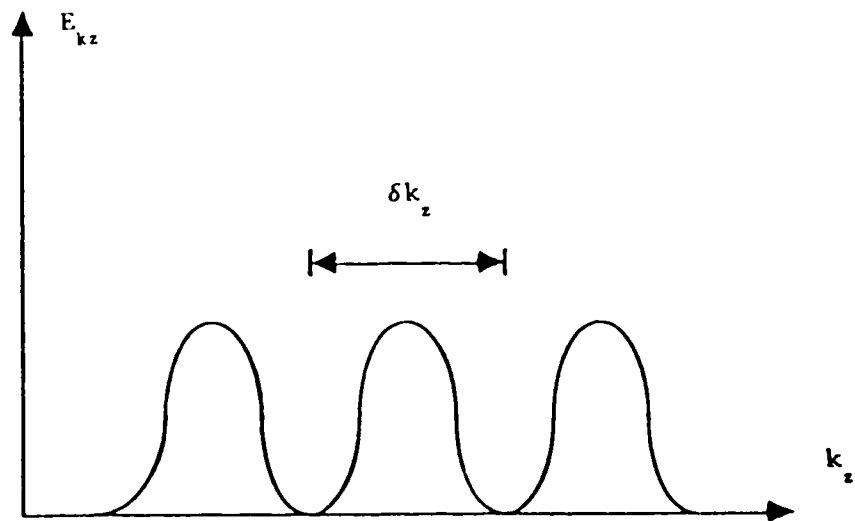


Fig. 3.2 A more realistic longitudinal Fourier spectrum

$$\frac{\delta\lambda}{\lambda_0} > \frac{\sqrt{2\Delta}}{ak_0 N_1} \quad (3.4)$$

where N_1 is the material group index. For a typical fiber with $N_1 \approx n_1 = 1.467$, $a = 25 \mu\text{m}$, $\Delta \approx 0.00934$, the linewidth of the source must exceed 0.4 nm and 1.0 nm for $\lambda_0 = 0.825 \mu\text{m}$ and $1.3 \mu\text{m}$ respectively. This limit is exceeded by present-day sources with the exclusion of single-mode lasers [34].

Referring to eqn. (2.13), there are many modes with the same principal mode number, hence the same propagation constant. A mode group with this property is called a degenerate mode group (DMG). Due to their identical propagation constants, strong power coupling occurs among the modes in the group so that the power distribution becomes uniform during the propagation of optical power along a fiber [27]. From now on, it is assumed that the power distribution within a DMG is uniform. Hence, the power distribution is given as a function of m only.

Manipulating eqn. (3.1)

$$k_{\perp}^2 = \left[\frac{m}{M} - \left(\frac{r}{a} \right)^2 \right] k_{\text{max}}^2 \quad (3.5)$$

where

$$k_{\perp}^2 = k_x^2 + k_y^2 \quad (3.6)$$

and

$$k_{\text{max}}^2 = 2\Delta n_1^2 k_0^2. \quad (3.7)$$

Eqn. (3.5) states the relationship between any ray's position, direction and principal mode number. Furthermore

$$\left(\frac{r}{a} \right)^2 < \frac{m}{M} \quad (3.8)$$

must hold. For a given principal mode number m , eqn. (3.8) determines the maximum radial distance a ray can exist. For modes from m to $m+\Delta m$, eqn. (3.5) is rewritten as

$$\left[\frac{m}{M} - \left(\frac{r}{a} \right)^2 \right] k_{\max}^2 \leq k_{\perp}^2 \leq \left[\frac{m + \Delta m}{M} - \left(\frac{r}{a} \right)^2 \right] k_{\max}^2. \quad (3.9)$$

Assuming that all rays that satisfy the above criteria have equal power P_o , the NFP (power per unit area),

$$N(r) = P_o * \text{k-space area.} \quad (3.10)$$

The NFP for modes m to $m+\Delta m$

$$N_m(r)\Delta m = P_o \int 2\pi k_{\perp} dk. \quad (3.11)$$

For $(r^2/a^2) < (m/M)$

$$N_m(r)\Delta m = \pi k_{\max}^2 \frac{\Delta m}{M} P_o \quad (3.12)$$

and $(r^2/a^2) > (m/M)$

$$N_m(r)\Delta m = 0. \quad (3.13)$$

The NFP formed by modes, m to $m+\Delta m$ is shown in Fig. 3.3. For all groups of m , assuming equal power for all modes (equal excitation)

$$N(r) = \int_{Mr^2/a^2}^M N_m(r) dm \quad (3.14)$$

$$= P_o \pi k_{\max}^2 \left[1 - \left(\frac{r}{a} \right)^2 \right]. \quad (3.15)$$

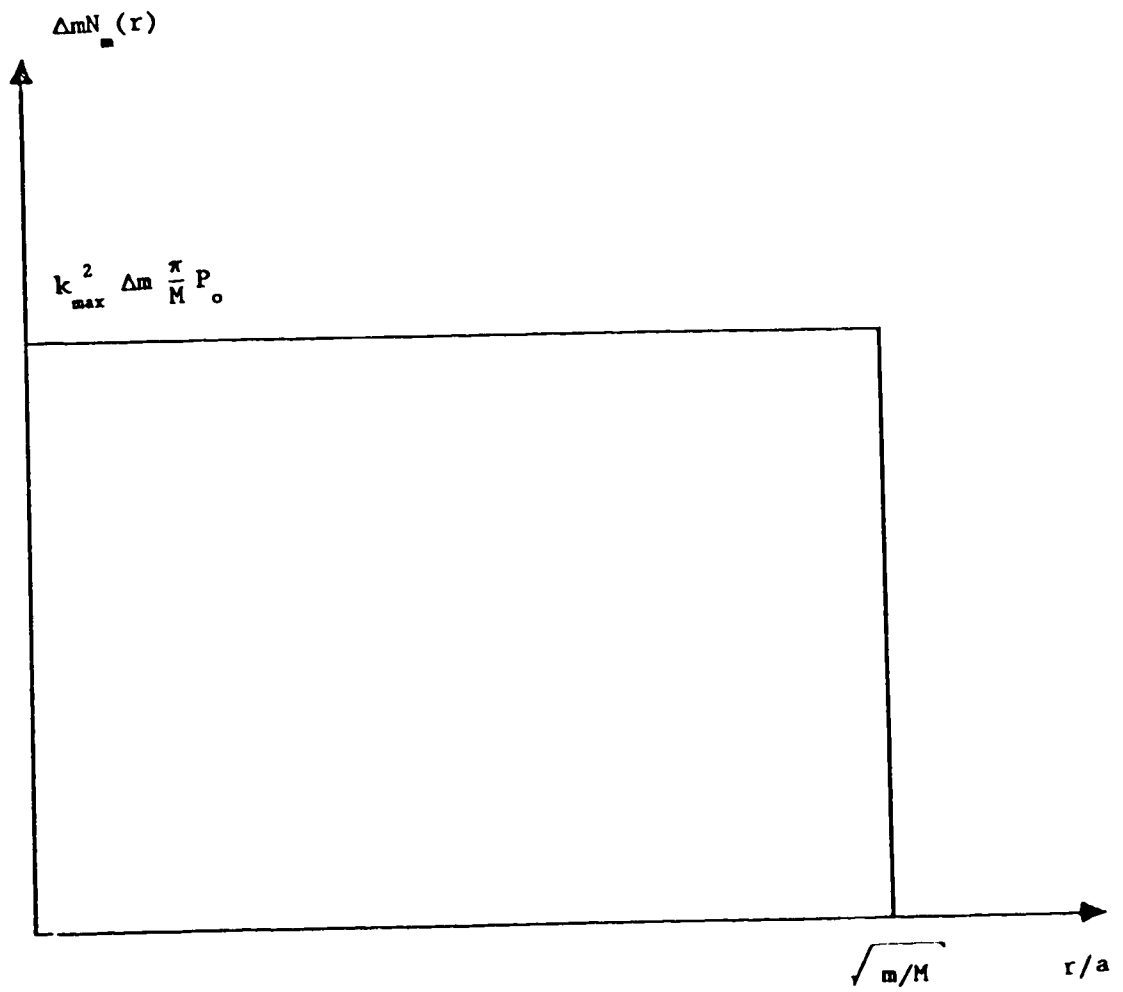


Fig. 3.3 Near-field pattern for all rays belonging to mode m to $m+\Delta m$

This result is identical with the result derived in Ref. [15] for a parabolic graded-index profile. The total power for modes m to $m+\Delta m$ is just the integral of the near-field pattern

$$Q(m)\Delta m = \int_0^{\sqrt{m/M} a} \frac{\Delta m P_{\text{max}} \pi k^2}{M} 2\pi r dr \quad (3.16)$$

$$= P_0 4\pi^2 m \Delta m \quad (3.17)$$

$Q(m)\Delta m$ is the power required to form the NFP given by eqn. (3.12). Integrating for all possible modes will result in the NFP as in eqn. (3.15). Hence, for an arbitrary power $P(m)\Delta m$, the near-field pattern

$$N(r) = \int_{Mr^2/a^2}^M \frac{N_m(r) P(m)}{Q(m)} dm \quad (3.18)$$

$$= \frac{k_{\text{max}}^2}{4\pi M} \int_{Mr^2/a^2}^M \frac{P(m)}{m} dm \quad (3.19)$$

Differentiating the near-field pattern $N(r)$

$$P(m) = - \frac{2\pi M}{k_{\text{max}}^2} \left[r \frac{dN(r)}{dr} \right] \Bigg|_{r = a\sqrt{m/M}} \quad (3.20)$$

Eqn. (3.20) is the relationship between the NFP and the power per principal mode group. A typical NFP is shown in Fig. 3.4 and the power per principal mode number is shown in Fig. 3.5.

In the derivation, the absence of leaky modes in the fiber has been assumed. In reality, this assumption is not valid. It is

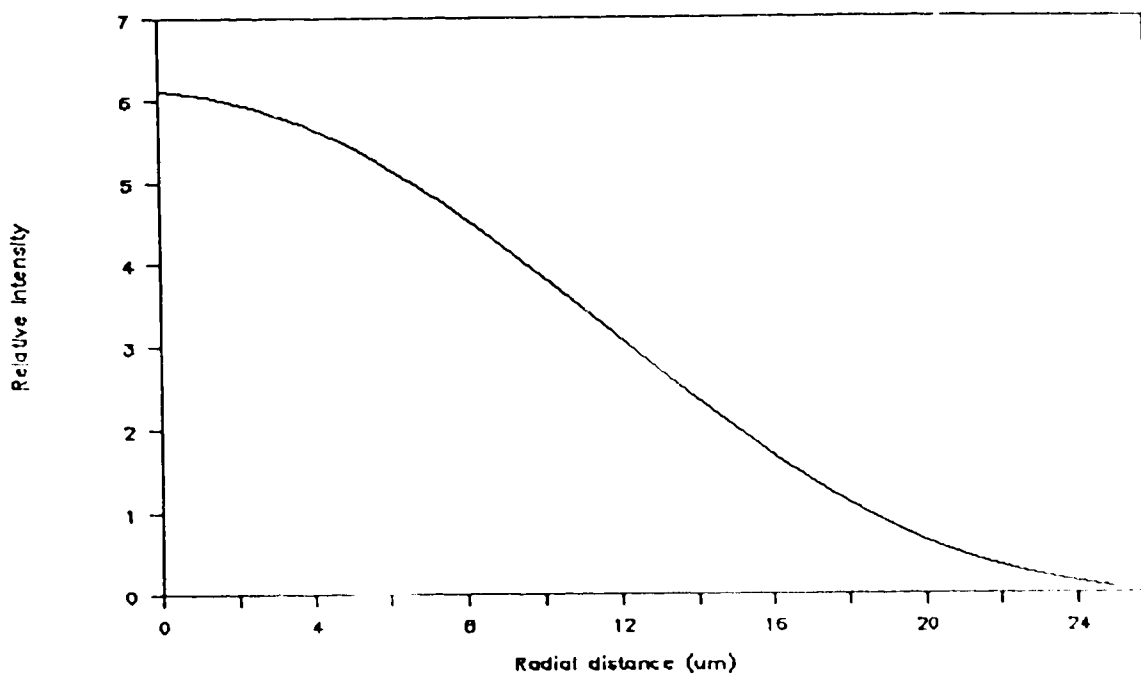


Fig. 3.4 A typical near-field pattern

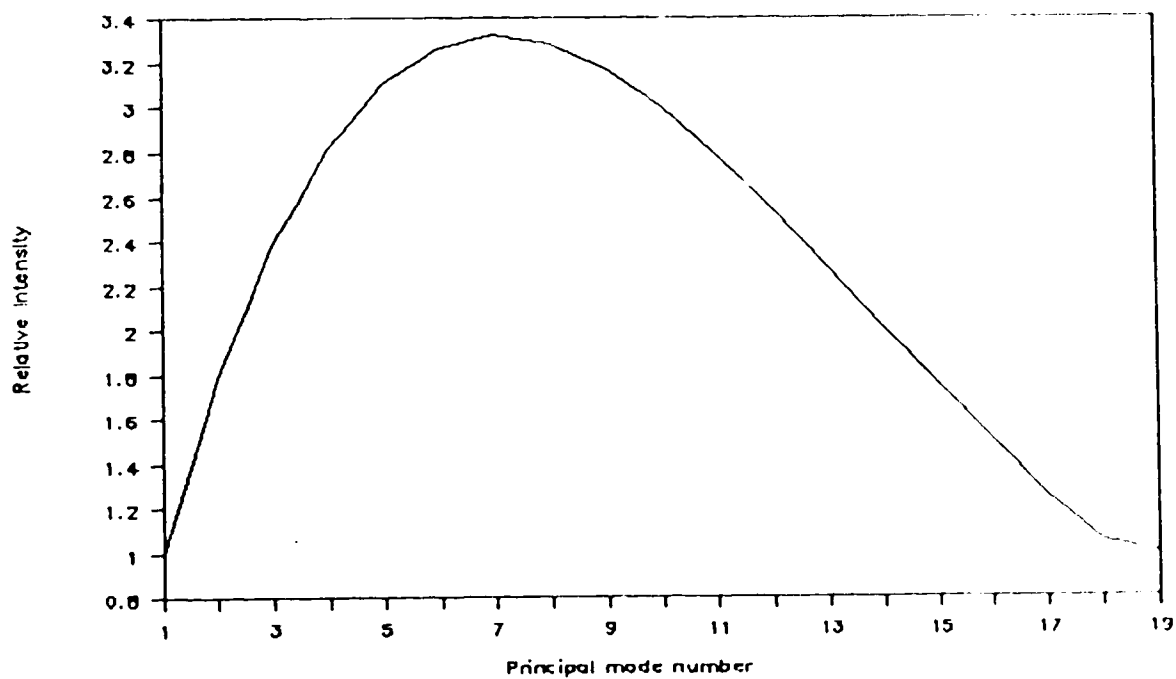


Fig. 3.5 The modal power distribution for the above near-field pattern

impossible to excite only guided modes in a fiber without exciting leaky modes. For leaky modes where $m/M > 1$, the relationship between the NFP and MPD is still an unsolved problem [30].

3.3 Measurement of the NFP

The intensity on the surface of a radiating source such as the end of a fiber is classified as near-field intensity. The emitting areas are typically very small (core radius $\approx 25 \mu\text{m}$). Hence, the near-field pattern cannot be measured directly. Instead imaging techniques must be applied to magnify the NFP to a size appropriate for measurements.

To avoid the effects of convolution, the magnified near-field can be scanned by placing a photodiode masked by a pin hole and moving it radially across the image. However, this method has two major disadvantages, the first being the critical alignment required. To obtain a near-field, the fiber has to be scanned across the axis of the fiber as shown in Fig. 3.6. The second disadvantage is the possibility of a difference in NFP when scanning across different axial directions (scans 2 & 3 in Fig. 3.6). This error is avoided provided the field is radially symmetric.

To avoid the above problems, a method utilizing slits is implemented. A large area detector masked by a slit is used to scan the magnified near field as shown in Fig. 3.7. One has to ensure that the magnified NFP falls within the large area detector. With this method, the power as function of x , $I(x)$ is measured, Fig. 3.8. The intensity $I(x)$ as a function of the radial distance, $I(r)$ takes the form of an Abel transform [35]

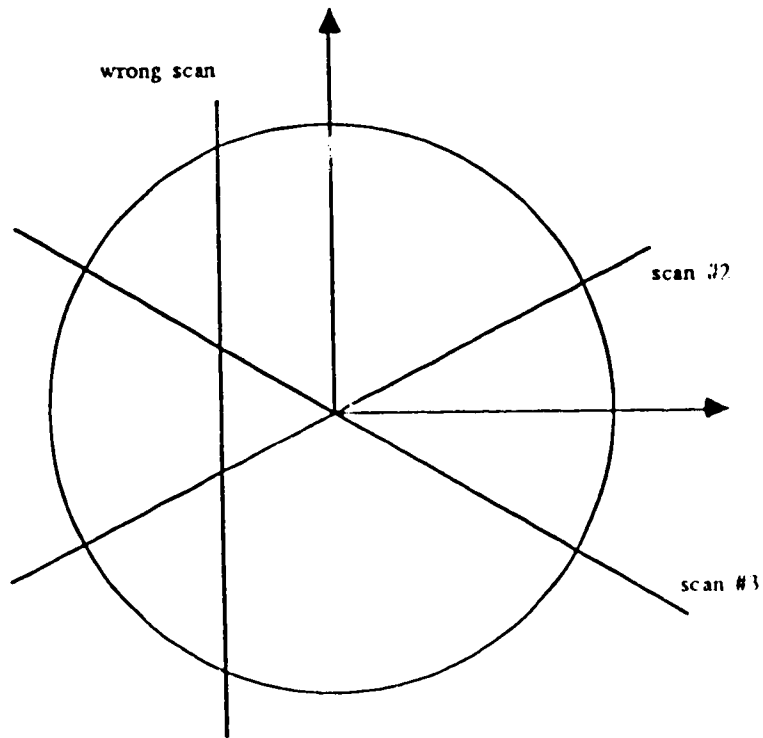


Fig. 3.6 Possible scans of the near-field pattern using the conventional pinhole method

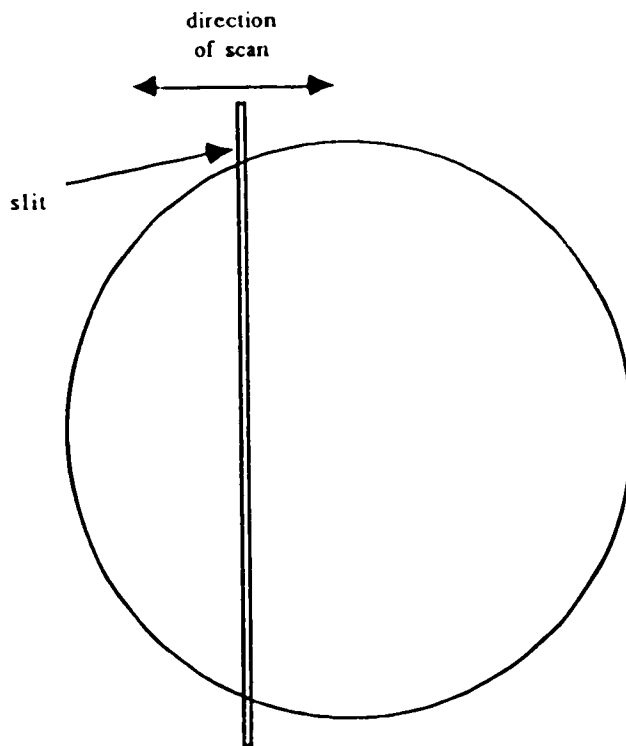


Fig. 3.7 Utilization of slits to scan the near-field pattern

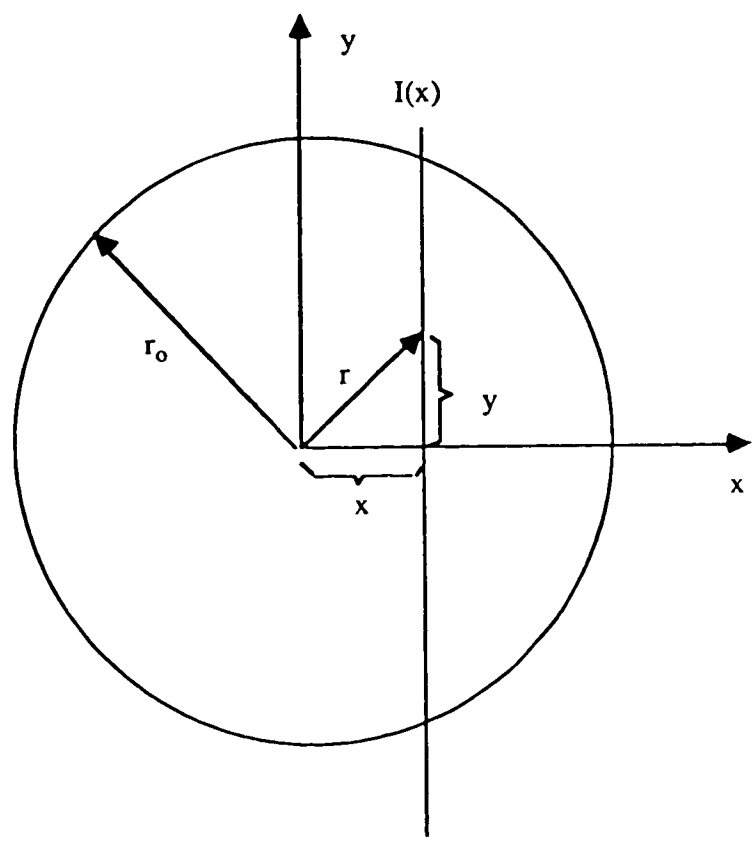


Fig. 3.8 Coordinate system used in scanning the near-field pattern using a slit

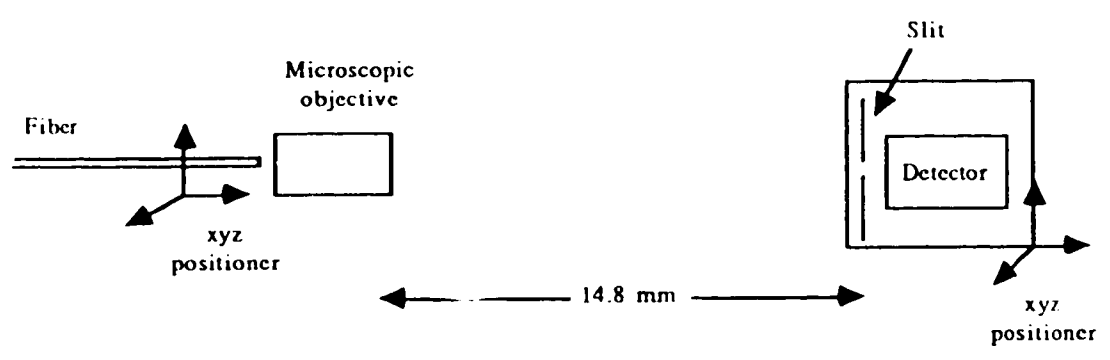


Fig. 3.9 Experimental setup to identify and scan the near-field pattern

$$I(x) = 2 \int_x^{r_0} \frac{I(r) r dr}{(r^2 - x^2)^{1/2}} \quad (3.21)$$

if one assumes a cylindrical column. The inversion to obtain the power as a function of the radial distance $I(r)$ can be accomplished by taking the inverse Abel transform [35]

$$I(r) = -\frac{1}{\pi} \int_r^{r_0} \frac{I'(x) dx}{(x^2 - r^2)^{1/2}} \quad (3.22)$$

For a particular slit position x , the average intensity in the y direction is measured. This method will provide an average NFP without having to depend on which direction the fiber's NFP is scanned.

The experimental setup to perform the slit experiment is shown in Fig. 3.9. A microscopic objective lens with a magnification of 40X was used to magnify the NFP. The distance between the lens and the magnified image (also the location of the slit) was set at 14.8 cm [36]. The fiber end is placed within the working distance of the lens on a xyz positioner. The position of the fiber was adjusted until a focused image is formed. The detector was masked with a slit of approximately 10 μm and both were placed on another xyz positioner. Hence, the intensity across the magnified NFP through the slit can be measured. Typical core radius is 25 μm and since a magnification factor of 40X was used, only a scan of ± 1 mm is necessary.

3.4 Ray distribution

The numerical simulation of bending loss consists of following a representative set of rays through the fiber bend. What remains to be determined is the selection of a set of rays for a principal mode

number. The method used is based on eqn. (3.5) which when rearranged is

$$\frac{m}{M} = \left(\frac{r}{a} \right)^2 + \left(\frac{k_{\perp}}{k_{\max}} \right)^2. \quad (3.23)$$

Discrete r and k_{\perp} variables r_i and $k_{\perp j}$ can be defined by

$$r_i^2 = \left(\frac{i}{M} \right) a^2 \quad (3.24)$$

$$k_{\perp j}^2 = \left(\frac{j}{M} \right) k_{\max}^2 \quad (3.25)$$

where i and j have discrete values of $\frac{1}{2}, 1\frac{1}{2}, 2\frac{1}{2}, \dots, M - \frac{1}{2}$. Hence the relationship between m , i and j is such that

$$m = i + j. \quad (3.26)$$

Therefore, there will be m combinations of i and j that can be selected to satisfy the above criterion for a given principal mode number. From eqns. (3.24) and (3.25) there will be m rings in the r and k_{\perp} space. To evenly select x , y , k_x and k_y , let there be L angles for each ring in either space such that

$$\phi_q = \frac{q 2\pi}{L} \quad (3.27)$$

where $q = 1, 2, 3, \dots, L$. Hence, there will be L spatial positions for each ring and L directions for each of the spatial positions.

An example to illustrate this procedure is in order. For principal mode number 6 there are 6 combinations of i and j

i	0.5	1.5	2.5	3.5	4.5	5.5
j	5.5	4.5	3.5	2.5	1.5	0.5

that satisfy eqn. (3.26). There are six rings in each of the r and k spaces. For an arbitrary value of L , there will be L spatial positions and direction vectors for each ring where

$$x, k_x = r_i, k_j * \sin(\phi_q)$$

$$y, k_y = r_i, k_j * \cos(\phi_q).$$

Figs. 3.10 and 3.11 depict typical position and wave vector parameters. Note that the innermost ring in the r space corresponds to the outermost ring in the k space and so forth. With L rays for each (x, y) positions, there are L^2 rays for each combination of i and j , and mL^2 rays for principal mode number m . The value of L is arbitrary. There is no rule as to how many rays are needed to represent a mode. The greater the value is, the finer the grid is in selecting the x, y, k_x, k_y values. Presumably, increasing the number of rays will lead to greater accuracy in the simulation results (see Section 5.4.1).

Recall from Section 3.2, it is assumed that all rays with the same principal mode number have equal power. Therefore, once the power and number of rays representing the modes with principal mode number m are determined, the power per ray is simply the ratio of the former over the latter.

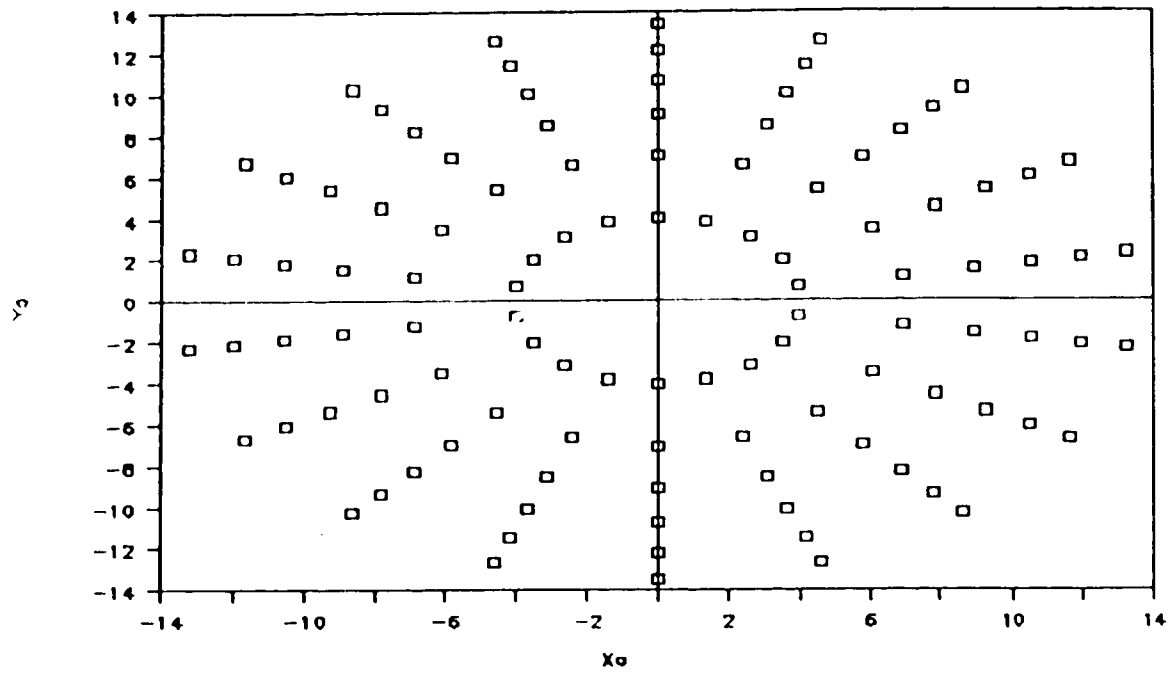


Fig. 3.10 Typical x , y positions of rays

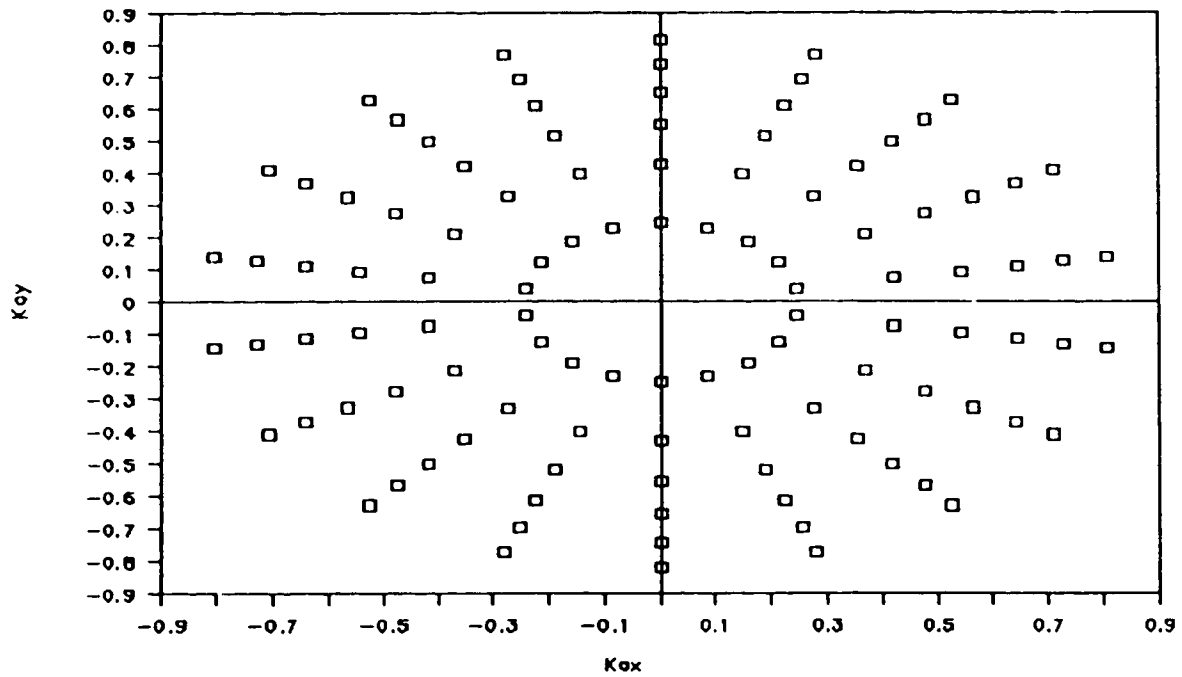


Fig. 3.11 Typical k_x , k_y parameters of rays

Chapter 4

Computer Simulation

4.1 Introduction

The ray equations in a fiber are presented in Chapter 2 with the emphasis on bent fibers. Ray propagation in different regimes of the fiber are taken into account. Chapter 3 deals with the modal power distribution of the fiber and a proposed method to generate initial parameters and assignment of power to each ray. The next stage to undertake is to implement the theory into a simulation program involving thousands of rays. The aim of this simulation program is to predict the bending losses and characteristics of radiation for a predetermined modal power distribution. Then the only parameters within the designer's control that affect the bending losses are :

1. radius of bend
2. amount of bend induced onto the fiber (angle of bend).

Once the above two parameters are determined for a given required performance level, the radiation pattern from the bend must be studied. This will allow proper positioning of the detector to improve the tapping efficiency. The tapping efficiency is defined as the fraction of power lost in the bend that is collected by the detector.

The aim of this chapter is to present the algorithm utilized in developing the simulation program. It starts off by describing the task of the program and stating any assumptions made in developing the software. Section 4.3 deals with the structure of the software program, breaking them down into different units and describing the task of each individual unit. The chapter concludes with a description

of another software package that is to be utilized in assisting in the pictorial representation of the radiating pattern from the bend. All software is written in Turbo Pascal 4.0 for usage on IBM compatible P.C.'s and all graphics require an EGA card.

4.2 Task of the simulation program

During its propagation, the ray will either leave the core or remain in it throughout. In the latter case, there is still a possibility of the ray leaving the core after the bend as it may not satisfy the conditions of a bound ray in a straight fiber. Such cases are only common when the angle of the bend is small. A typical path of the ray leaving the fiber is shown in Fig. 4.1. Only rays that leave the core are of interest. Once it is determined that the ray is leaving the core, it is tracked till the point it leaves the jacket. Seven parameters are required in the characterization of a ray : x, y, z, k_x, k_y, k_z (where z represents the on-axis length the ray travelled around the bend) and power remaining after going through the interfaces of different refractive indices. The parameters of the rays that leave the fiber are to be stored in an external file from where they can be processed by other software programs.

A number of assumptions are made in the process of developing the software simulation.

1. The effects of leaky rays are not considered.
2. The mechanism of tunnelling for the ray while in the bend is ignored.
3. The only reflected rays considered are the ones from the cladding/primary jacket interface.

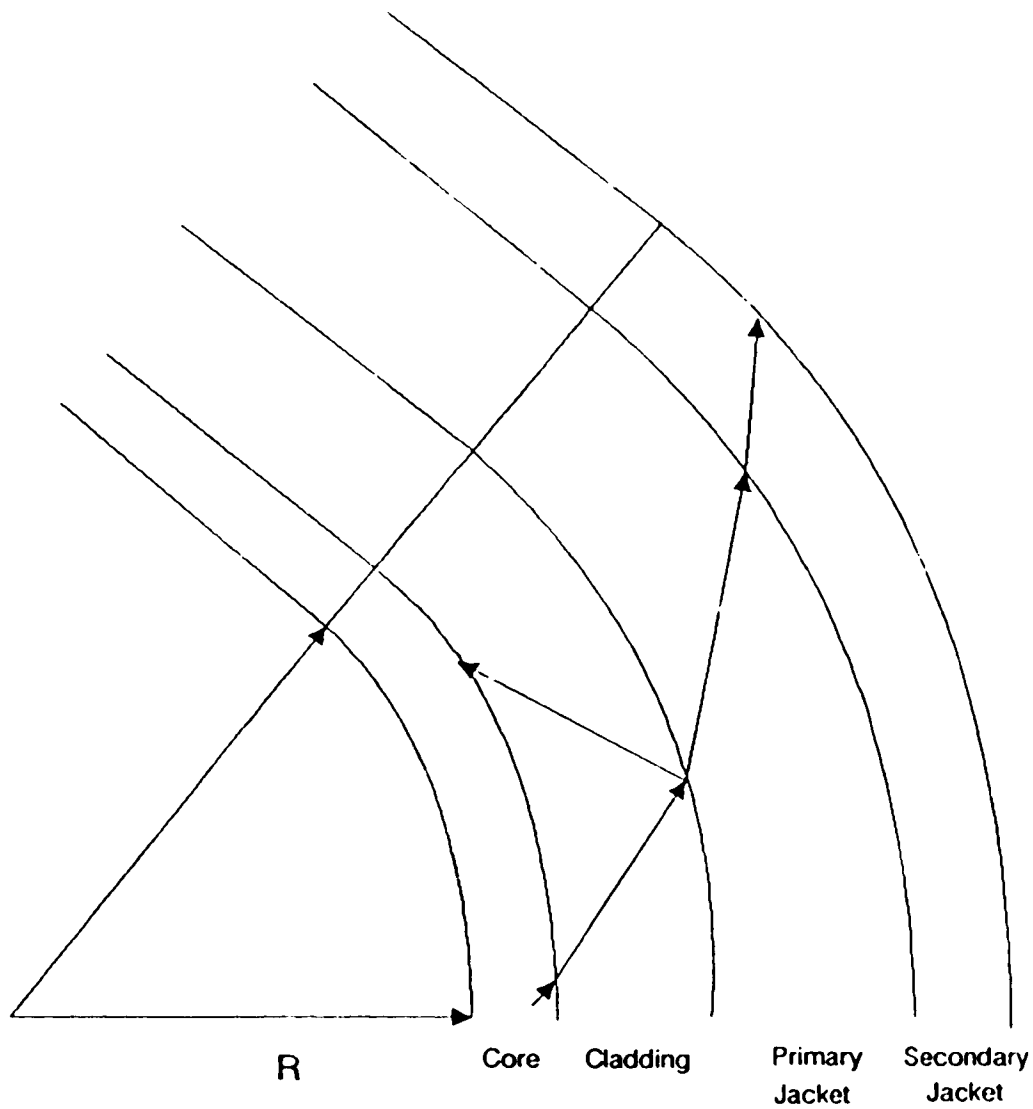


Fig. 4.1 Possible path of a refracting ray in a bent fiber

With regard to the first assumption, it is true that it is impossible to excite guided rays without exciting some leaky rays. However, the task of relating the near-field pattern and leaky modes is still an unsolved problem (see Chapter 3). Hence, they are ignored.

The mechanisms of power loss for rays while in the bend are by refracting and tunnelling [5]. In Ref. [5], the transmission coefficient formula of tunnelling rays derived in Ref. [37] was used in determining the tunnelling loss of rays in a bend. A typical plot of power remaining in a bent fiber reconstructed from Fig. 8 of Ref. [5] is shown in Fig. 4.2. It can be noted that there is an initial rapid loss of power from the bent fiber and subsequently a more gradual loss. Recall from Chapter 2, that the propagation of rays in a bent fiber is periodic (for a typical value of $\Delta = 0.00934$, the ray will repeat itself every 1.2 mm). Hence, rays leaving the core will do so within the first period or remain in the core throughout the bend. This explains the initial rapid drop in power. The subsequent gradual drop in power is due to the tunnelling of the rays that remain in the core. The power loss from tunnelling is not very significant compared to the loss by refraction.

Reflection is significant at interfaces with a great refractive index mismatch. If an external fluid with a refractive index close to that of the secondary jacket is used, the only significant mismatch in refractive index is at the cladding/primary jacket interface. The other slight mismatches can be ignored due to the following reason. As a ray passes through the cladding/primary jacket interface, its propagation constant $|\vec{k}|$ will increase by a factor of 1.54/1.453 (see Chapter 2). Since k_z remains unchanged through an interface, the

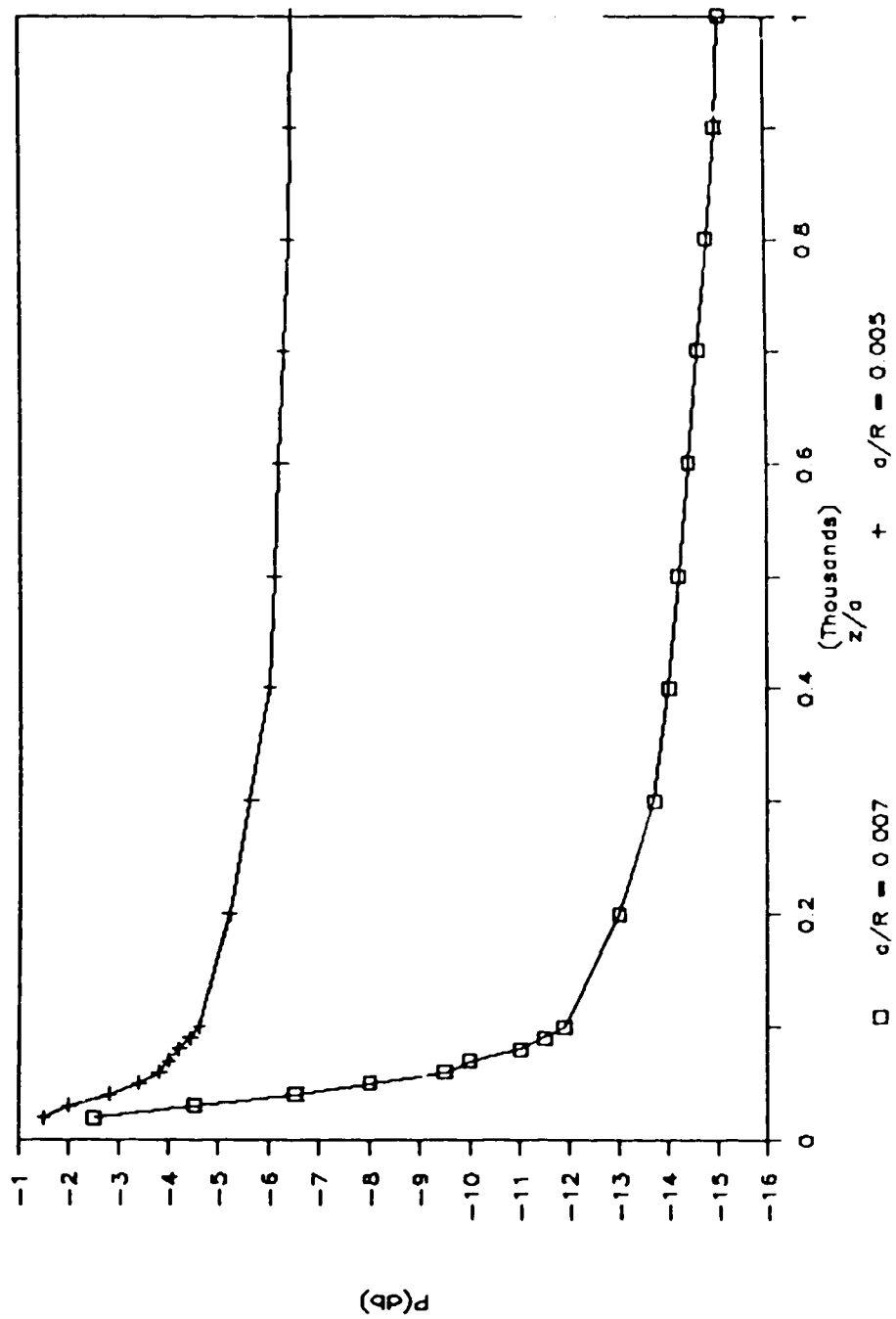


Fig. 4.2 Theoretical power remaining as a function of normalised distance z/a with z measured around the axis of the core

values of k_x and k_y will increase accordingly. With that, it is expected by the time the ray hits the other two interfaces (primary jacket/secondary jacket and secondary jacket/coupling fluid), the angle (see Chapter 2 for definition of angle) will be less than what is required for a significant reflected power. To consider all mismatches would be a monumental task as each ray splits into two each time it encounters an interface. Therefore, for each single ray leaving the core would mean tracking hundreds of rays. To consider one interface is already a monumental task, see Fig. 4.4.

4.3 Structure of the simulation software

The simulation software consists of ten main units as shown in Fig. 4.3. The simulation begins at the Generate Initial Data unit. Rays are generated, passed onto the control unit and processed one at a time. At the start of each processing sequence, a global time clock is initialized to zero and the propagation of the ray is calculated by stepping up in time. The functionality of each unit is described in the following subsections.

4.3.1 Generate Initial Data

Input : external file consisting of power per ray depending
on the principal mode number.

Output : k_x , k_y , k_z , x , y , Power of the ray.

The task of this unit is to generate the initial parameters of the ray and pass them onto the control unit. As mentioned before, only guided rays are considered. For a given wavelength, the number of rays, position and wave vector of each ray are set (see Section 3.4).

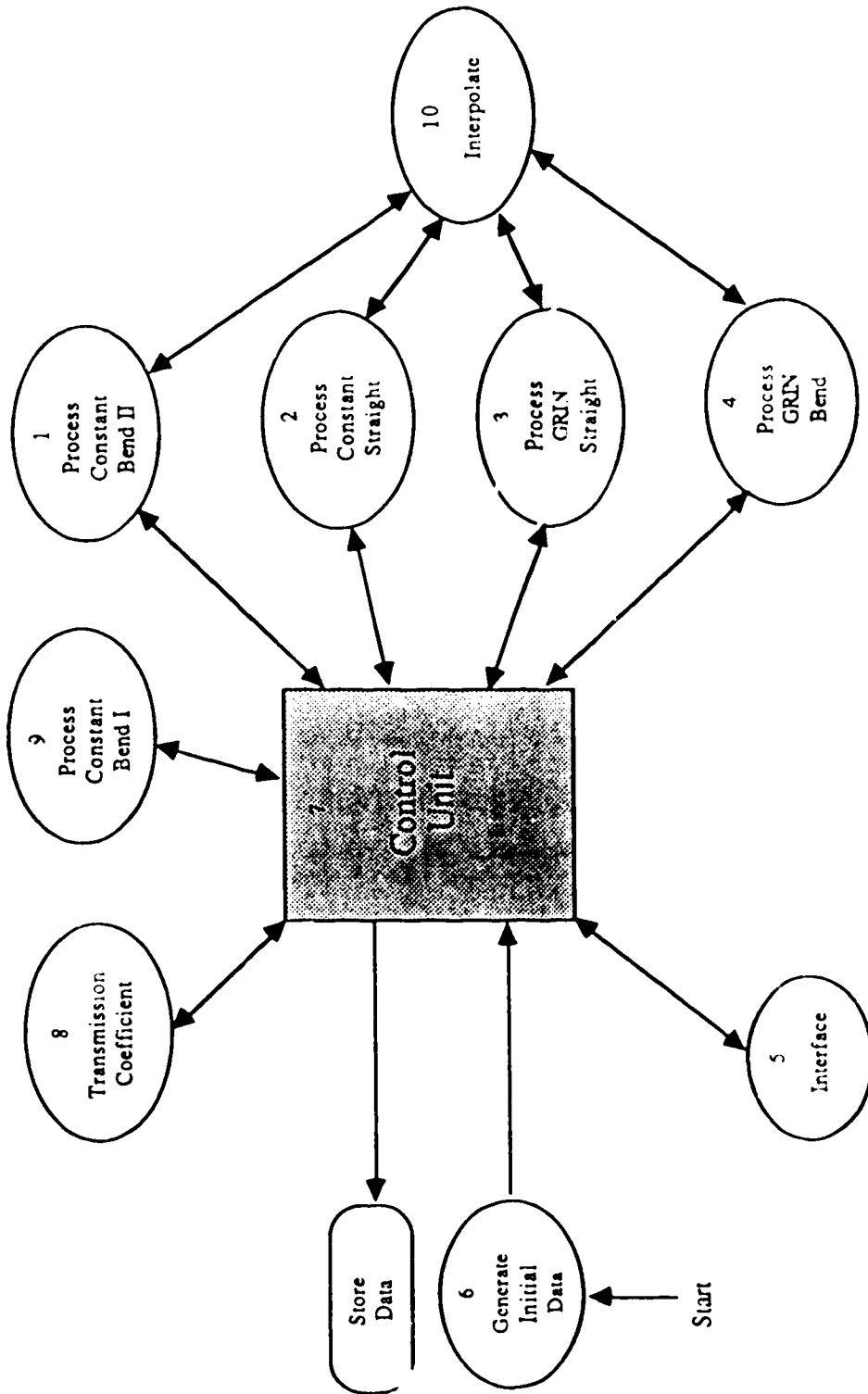


Fig. 4.3 Structure of the simulation program

However, the power per ray will depend on the modal power distribution of the fiber. This task is to be determined externally. A file consisting of power per ray depending on the principal mode number is to be created and will be a required input data file for this unit. Rays are processed in order of ascending principal mode number.

4.3.2 Process GRIN Bend

Input : x, y, k_x, k_y, k_z

Output : x, y, z, k_x, k_y, k_z and condition of exit

This unit tracks the propagation of the ray in the parabolic graded-index core as described by the formulas presented in Section 2.4. The values of x, y and z are computed until either one of the two exit conditions is met. The first condition is satisfied when $\sqrt{x^2 + y^2}$ is greater than the radius of the core indicating a refracting ray. Second condition of exit occurs when the ray reaches the end of the bend while remaining in the core. Since the propagation of the ray is periodic, it is only necessary to track the ray for one whole period or until it leaves the core. If the ray does not leave the core within the first period, the ray will remain in the core throughout the bend. The control unit is notified on the condition of exit to enable it to enact the next appropriate action. The remaining ray parameters are to be computed at the time of exit and returned to the control unit.

4.3.3 Process Constant Bend I

Input : x, y, z, k_x, k_y, k_z

Output : x, y, z, k_x, k_y, k_z and condition of exit

This unit tracks the propagation of the reflected ray in the

cladding as described by the formulas presented in Section 2.5. There are three conditions of exit. The first being the reflected ray re-entering the core while the second condition is the reflected ray re-entering the primary jacket. The third condition is the reflected ray encountering the end of the bend. Here the equations are not periodic, so the unit has to keep stepping up in time until it satisfies either one of the exit conditions. Again, the control unit should be informed of the condition of exit. The remaining rays parameters are computed at the time of exit and returned to the control unit.

4.3.4 Process Constant Bend II

Input : x, y, z, k_x, k_y, k_z

Output : x, y, z, k_x, k_y, k_z and condition of exit

This unit tracks the propagation of the ray in the cladding and jackets as described by the formulas presented in Section 2.5. The control unit should notify it by passing the correct refractive index and radius of the region. There are two conditions of exit. The first condition applies when $\sqrt{x^2 + y^2}$ is greater than the radius of the region. The second condition of exit occurs when the ray encounters the end of the bend while in that particular region. Again, the control unit should be informed of the condition of exit. The remaining rays parameters are computed at the time of exit and returned to the control unit. The differences between this unit and the aforementioned unit are the exit conditions and that the latter is only for rays reflected off the cladding/primary jacket interface.

4.3.5 Process GRIN Straight

Input : x, y, z, k_x, k_y, k_z

Output : x, y, z, k_x, k_y, k_z

This unit deals with the propagation of the ray in a straight core should the ray remain within it after the bend, see Section 2.3. This unit is necessary as rays that are guided while in the bend may not satisfy the condition of a guided ray in the straight portion of the fiber after exiting the bend. Once the control unit determines that the ray does not satisfy the guided condition of a ray, this unit is called and exits only when the ray hits the core/cladding interface.

4.3.6 Process Constant Straight

Input : x, y, z, k_x, k_y, k_z

Output : x, y, z, k_x, k_y, k_z

The purpose of this unit is to compute the propagation of the rays in a straight constant index media. The formulas are derived in Appendix B. It is called upon by the control unit when encountering rays that remain in either the cladding or jacket after leaving the bent portion of the fiber.

4.3.7 Interpolate

Input : t_1, t_2, r_1, r_2, r_3 (see below for details)

Output : t

The accuracy in the simulation results will depend heavily on the step size used. Greater accuracy calls for smaller step size but the time required for a simulation of this magnitude will increase significantly. However, it can be deduced that accuracy is only critical in determining the time the ray crosses the interface between two regions at $r = r_3$. Since the propagation of the ray is calculated

by stepping up in time, the time (t_1) and radial distance (r_1) at which $r_1 < r_3$ and the time (t_2) and radial distance (r_2) at which $r_2 > r_3$ are known. Hence, the time (t) the ray crosses the interface (r_3) can be interpolated. This unit is called by the five previously mentioned units whenever it is determined that a ray is entering a new region.

4.3.8 Interface

Input : x, y, k_x, k_y, k_z

Output : k_x, k_y, k_z

As mentioned before, the propagation vector of a ray changes once it travels through two mediums of different refractive indices. This unit implements the theory presented in Section 2.6.

4.3.9 Transmission Coefficient

Input : $x, y, k_x, k_y, k_z, n_1, n_2$

Output : Transmission coefficient

The purpose of this unit is to compute the transmission coefficient of a ray travelling from a medium of refractive index n_1 to n_2 . The theory is presented in section 2.7.

4.3.10 The Control Unit (CU)

The CU is the heart of the simulation program. Once the initial ray parameters are passed onto this unit, it takes control of further action to be pursued by the program. The algorithm of this CU is shown in Fig. 4.4 which with a little description will be self-explanatory. The call number corresponds to the number of the particular unit in Fig. 4.3. The print in *italics* indicates a decision is to be made for a subsequent action. The letters next to some calls (e.g. cladding,

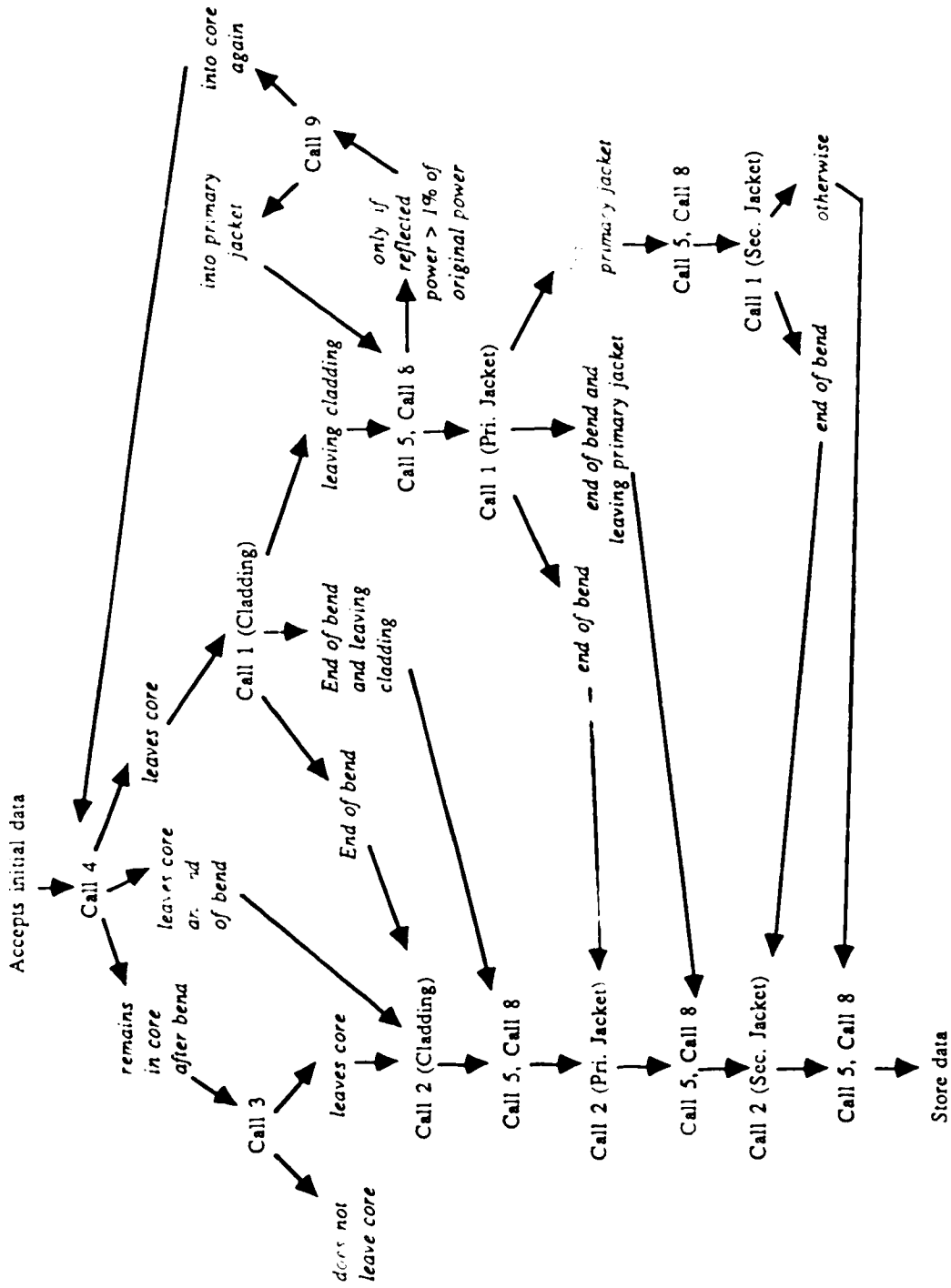


Fig. 4.4 Algorithm of the Control Unit

primary jacket) indicates to that particular unit as to which region the ray is propagating in. Propagation in the cladding and jacket are identical except for the refractive index and radius. Recall, that this distinction is required by that unit. Besides making decisions, the CU only computation is the amount of power radiated to the exterior after passing through the two interfaces. This is done after the two transmission coefficients are determined. The parameters of the lost rays right at the exterior of the jacket together with its remaining power are written to an external file.

4.4 Software for observing radiation patterns

With the simulation program determining the parameters of all the rays leaving the fiber, another software program was written to analyze the data. The program plots the radiation pattern of a bent fiber. It will not be discussed in terms of algorithm or structure but only of functionality.

The program is used to observe the radiating pattern for a specific radius of bend which utilizes the data generated from the simulation program. The location (y and z coordinates) and radius of the observation plane (see Fig. 4.5), which represents the detector must be specified by the user. The x coordinate need not be specified as the plane will be placed symmetrically on the x-axis. Furthermore, the detector is always placed perpendicular to the z-axis. This came about after viewing several simulated radiation patterns which were found to exhibit some parallelism to the z-axis. Radiating plots in the y-z and x-y planes can be observed simultaneously. A picture of such a pattern is shown in Fig. 4.6. The green lines represents the

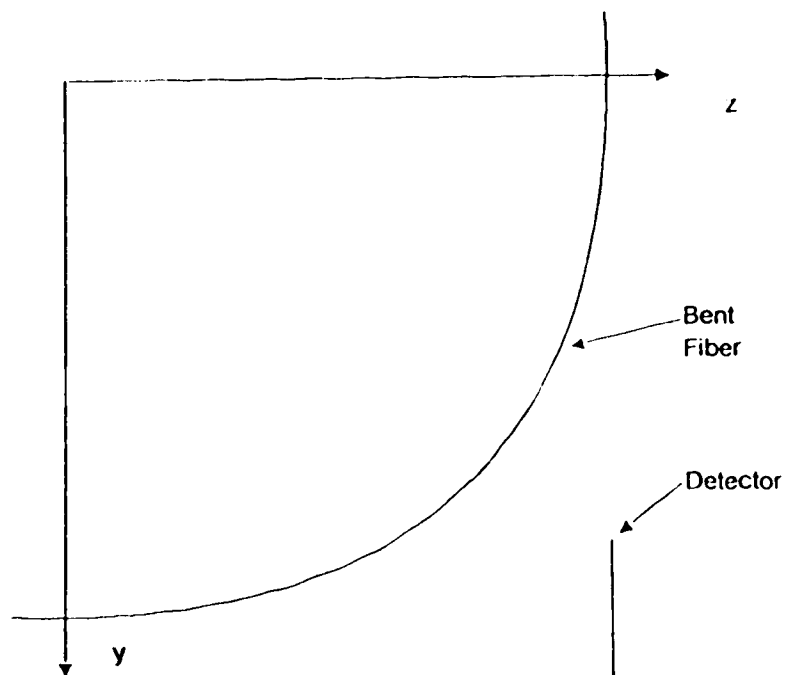


Fig. 4.5 Coordinate system used in observing the radiating patterns

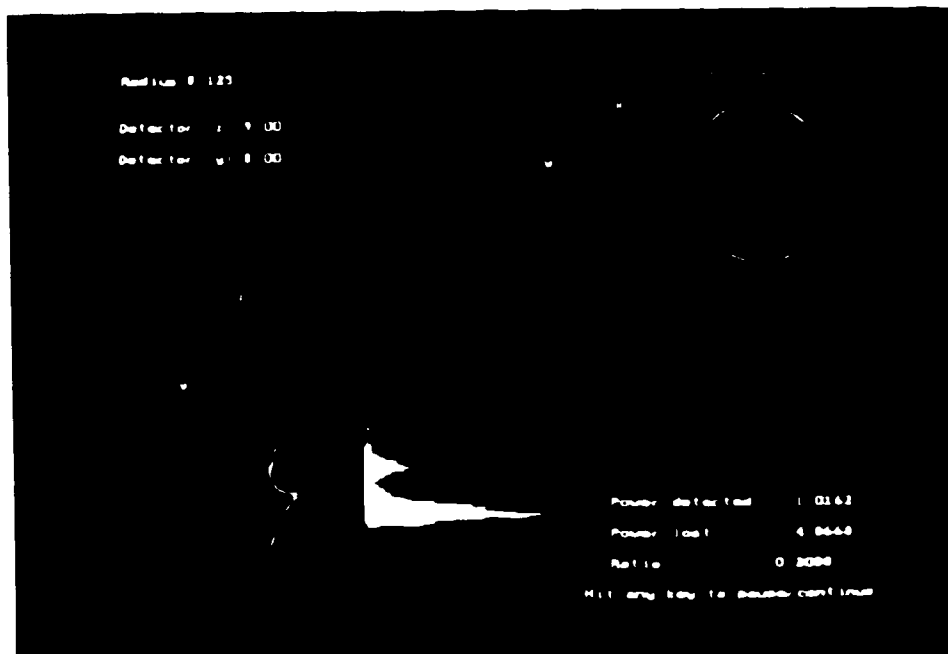


Fig. 4.6 Computer simulated radiation pattern

fiber while the colour red represents the rays leaving the fiber to the observation plane (in white). A histogram of the rays reaching the detectors is drawn in yellow. It is useful in a sense that the location of the greatest intensity can be easily identified. The circle in white represents the detector looking at it on the xy plane. The rays on yz plane can be drawn by either suppressing k_x or selecting rays with $k_x = 0$.

Chapter 5

Comparison of Experiment and Theory

5.1 Introduction

Comparison of experimental results with the theoretical analysis on bending losses and radiation patterns are presented in this chapter. Two laser sources at $0.825 \mu\text{m}$ and one source at $1.3 \mu\text{m}$ were used in the experiment. All three sources with fiber pigtailed were butt-coupled to the multimode fiber. The fiber has a numerical aperture¹ (N.A.) of 0.2 with a $50/125/205/250 \mu\text{m}$ core/cladding/primary/secondary jacket diameter. The cladding of the fiber is made of pure silica and the refractive indices of the primary and secondary jacket are 1.54 and 1.53 at $0.589 \mu\text{m}$ respectively [38]. It must be noted that the refractive index of pure silica changes with wavelength (eqn. (2.2.32) of Ref. [19]). The refractive indices of the jackets (made from acrylate) are not expected to change much with a change in wavelength except for the third and fourth decimal place [38]. Immersion fluid of refractive indices 1.50 and 1.538 at $0.825 \mu\text{m}$ were used as the external fluid to couple light present in the jacket to the exterior. In determining the radiation pattern, only the $0.825 \mu\text{m}$ laser source was used as the pin detector is made of silicon.

In the computer simulation, the value of L (see eqn. (3.27)) was chosen to be 18 (an arbitrary value). Therefore, there are 61560 rays in total for $\lambda = 0.825 \mu\text{m}$ (maximum principal mode number of 19) and 25272 rays in total for $\lambda = 1.3 \mu\text{m}$ (maximum principal mode number of

¹Numerical aperture is defined as $\sqrt{n_1^2 - n_2^2}$

12). The dependence of the simulation results on the value L will be investigated. The step size used to increment the global time clock was 0.1 ps. This is approximately 1/60 the period of the ray.

The chapter opens by presenting the theoretical and experimental results of bending losses. In section 5.3, the radiation patterns will be discussed. The chapter concludes with a discussion on any discrepancy that may exist between experimental and simulation results.

5.2 Bending losses

To theoretically predict the bending losses for a fiber with an arbitrary modal power distribution (MPD), the following steps are performed:

1. Perform the slit experiment as discussed in Section 3.3 and curvefit the data to ease the procedure of numerically integrating eqn. (3.22).
2. Perform the inverse Abel transform to obtain the near-field pattern (NFP) as discussed in Section 3.3.
3. Obtain the MPD from the NFP as discussed in Section 3.2.
4. Determine the power of each ray from the MPD as discussed in Section 3.4 and feed results to the simulation program.

For each source used in the experiment, the raw data from the slit experiment and the best-fit curve, the near-field pattern, the modal power distribution and bending losses are presented.

The experimental setup to measure the bending losses is shown in Fig. 5.1. In measuring the loss, the fiber is bent around rods of different radii ranging from 2 to 10 mm in radius (the radius of

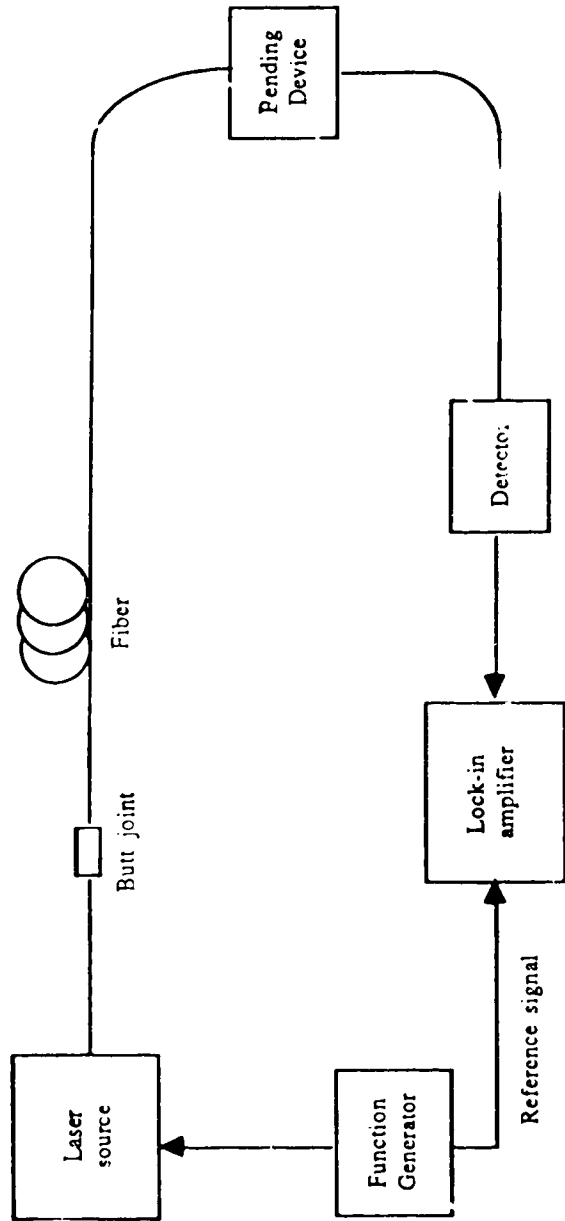


Fig. 5.1 Experimental setup to measure bending losses

curvature of the bend is hereafter referred to as R). Therefore the actual R is the radius of the rod plus 125 μm (taking into account the radius of the fiber). The power loss factor is defined as

$$P_L = \frac{P_{w_0} - P_w}{P_{w_0}} \quad (5.1)$$

where P_w and P_{w_0} is the throughput power with and without the induced bend respectively. Due to the difficulty encountered in designing a device to measure bending losses as a function of angle of bend for a specific radius, all measurements were done for a 90° bend.

In the measurement of loss, there are two sources of uncertainty, instrument error and power level fluctuations. The instrument uncertainty is given as 0.05% of the maximum scale reading, P_{max} [39]. Using eqn. (5.1), this gives a percentage relative uncertainty in P_L of

$$\frac{\Delta P_L}{P_L} = \frac{(0.05\%) (P_{w_0} - P_w) / (P_{\text{max}})}{P_L (P_w / P_{\text{max}})^2} \quad (5.2)$$

For example, typical measured values are $R = 7 \text{ mm}$, $P_{w_0} / P_{\text{max}} = 0.364$, and $P_w / P_{\text{max}} = 0.354$. Then $\Delta P_L / P_L = 10\%$. As the loss decreases, the instrument uncertainty increases even more. The power level fluctuations are random and difficult to measure. The combined effect of these two sources of uncertainty can be estimated by repeating a set measurements and comparing the results. When this was done, the uncertainty in the loss over the whole range was found to be in the range of 15%. Hence a relative experimental uncertainty of 15% is assumed in all the loss measurements.

5.2.1 Laser I (0.825 μm)

For this source, two cases were considered. The first case involves just direct bending losses with no attempt to alter the MPD. However, the second case involves wrapping the fiber 5 times around a 12 mm diameter mandrel. Since wrapping a fiber around a mandrel would eliminate the higher order modes, one would expect a lower power distribution for the higher order modes and thus less bending loss.

The raw data from the slit experiment, the NFP and the MPD for the first case are shown in Figs. 5.2 to 5.4. Since a coherent source was used, the NFP did not resemble eqn. (3.15) indicating the fact that the modes are not equally excited. This is further supported by the fact that the peak power distribution occurred at $m = 7$ and decreases with increasing principal mode number. The bending losses for different R are shown in Fig. 5.5. The simulation results are plotted on the same figure and evidently there is a very sharp contrast in the two curves. Fig. 5.6 shows an expanded comparison between the two curves for larger values of R . Discussions on what may cause the discrepancy between experimental and theoretical results will be pursued after all the experimental and simulation results for all sources are presented.

A sample of the simulation results for various R are tabulated in Tables 5.1 to 5.4. The last column is the ratio of power loss over total power for a particular principal mode number. It must be noted that the number of rays and number of rays lost are independent of the MPD. This is because the trajectory of the ray in the fiber is independent of its power. Furthermore, the power loss ratio is also independent of the MPD and is roughly equal to the ratio of rays lost within the first period of oscillation over the number of rays

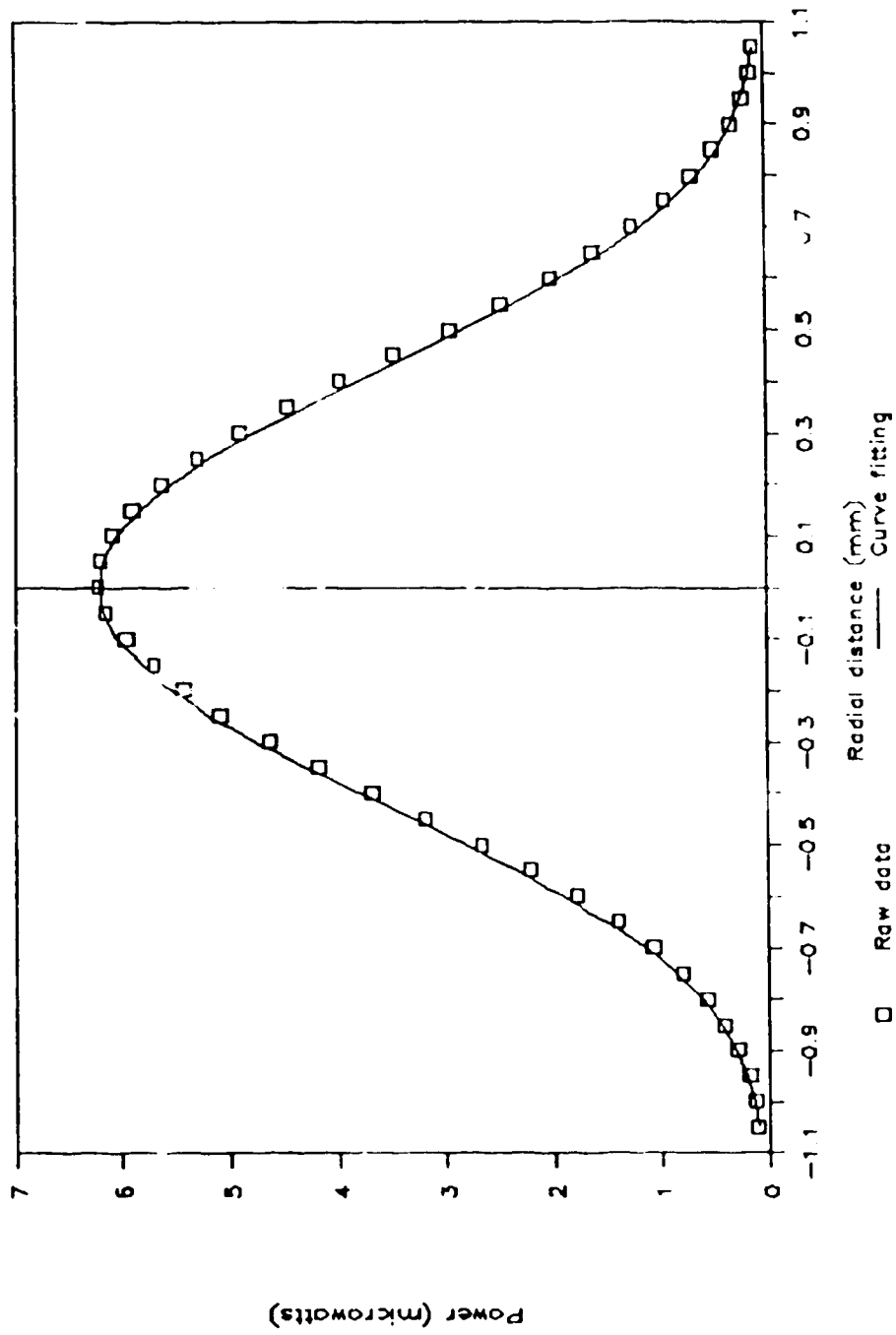


Fig. 5.2 Experimental and curve-fitted results from the slit experiment for the first of the two 0.625 μm laser sources

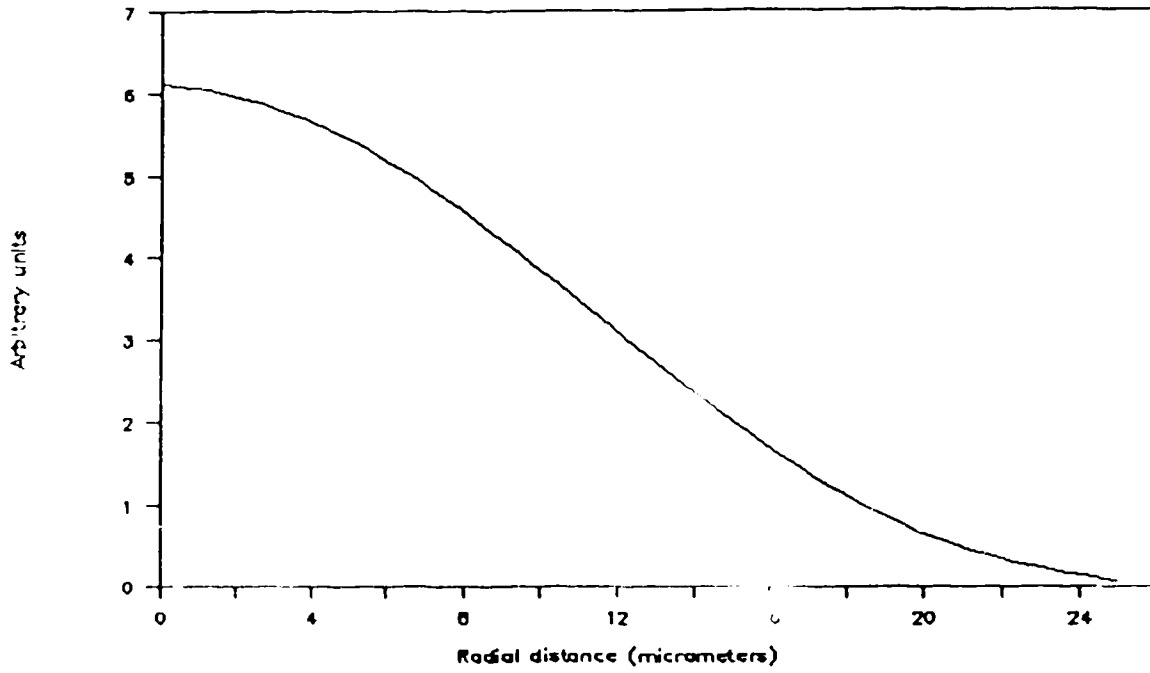


Fig. 5.3 The near-field pattern derived from Fig. 5.2

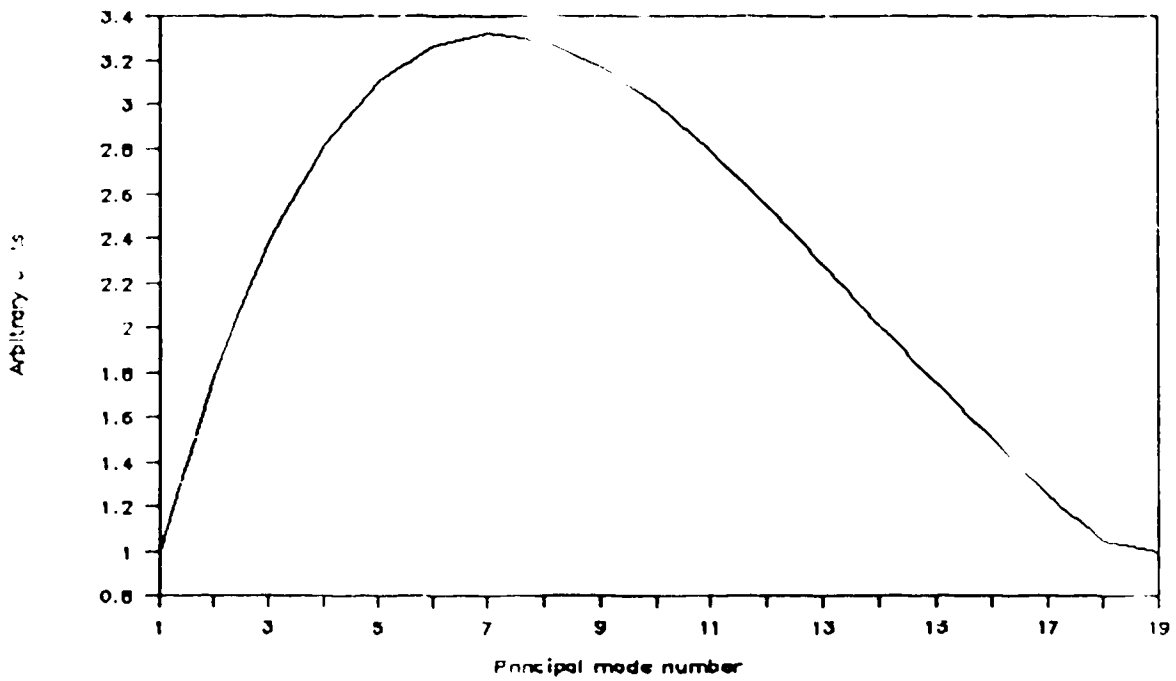


Fig. 5.4 The modal power distribution derived from Fig. 5.3

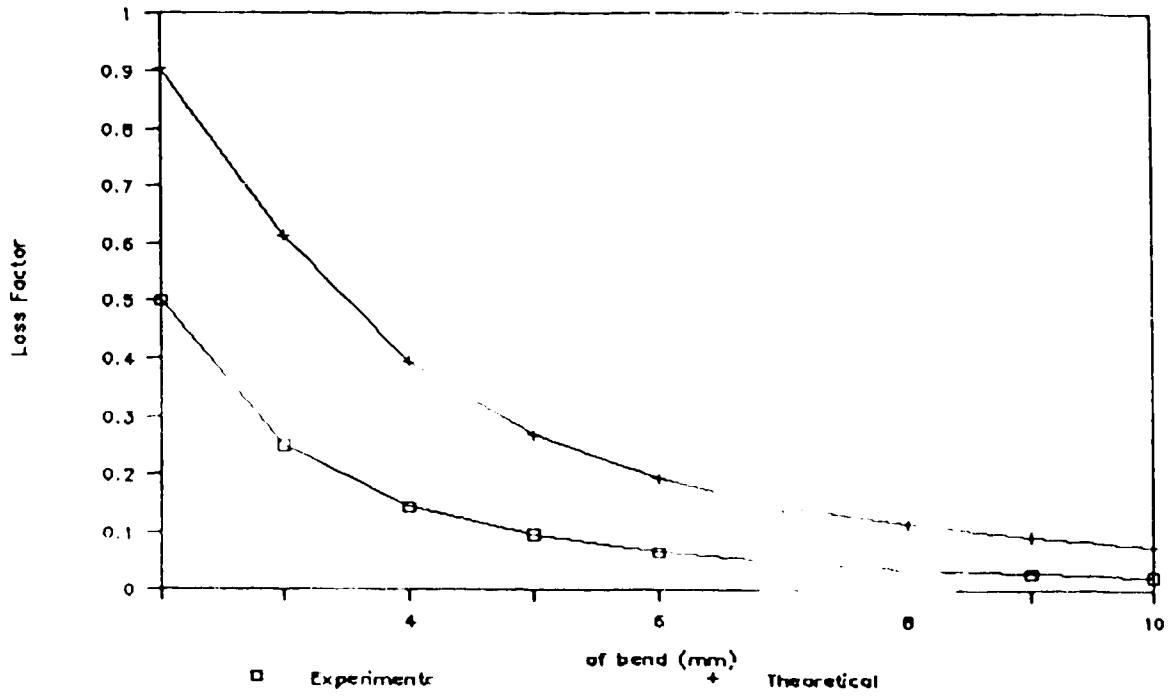


Fig. 5.5 Experimental and theoretical bending losses for modal power distribution in Fig. 5.4. Experimental uncertainty is 4% in all loss measurements.

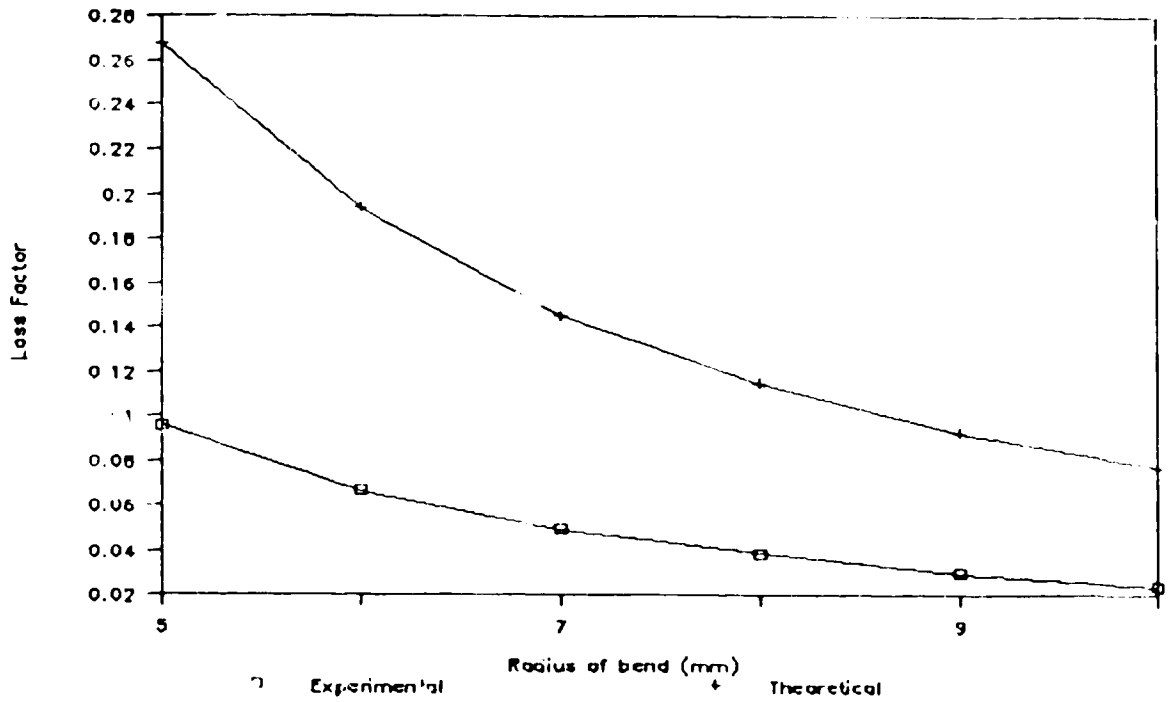


Fig. 5.6 Exploded comparison from Fig. 5.5

in	Number of Rays	Total Power	Number of Rays lost	Power loss	Ratio
1	324	1	0	0	0
2	648	1.782	0	0	0
3	972	2.380	0	0	0
4	1296	2.815	0	0	0
5	1620	3.106	0	0	0
6	1944	3.269	0	0	0
7	2268	3.325	0	0	0
8	2592	3.289	164	0.0453	0.014
9	2916	3.177	694	0.168	0.053
10	3240	3.007	1772	0.332	0.111
11	3564	2.791	2780	0.433	0.155
12	3888	2.547	4552	0.576	
13	4212	2.284	6060	0.635	0.8
14	4536	2.013	7502	0.659	0.327
15	4860	1.753	9452	0.705	0.402
16	5184	1.506	12020	0.709	0.471
17	5508	1.255	14156	0.672	0.535
18	5832	1.051	17562	0.647	0.615
19	6156	0.995	23433	0.721	0.724
		43.346		6.302	0.75

Table 5.1 Simulation results for $R = 7.125$ $\lambda = 0.825 \mu\text{m}$

m	Number of Rays	Total Power	Number of Rays lost	Power loss	Ratio
1	324	1	0	0	0
2	648	1.782	0	0	0
3	972	2.380	0	0	0
4	1296	2.815	0	0	0
5	1620	3.106	0	0	0
6	1944	3.269	0	0	0
7	2268	3.325	0	0	0
8	2592	3.289	0	0	0
9	2916	3.177	72	0.0172	0.005
10	3240	3.007	644	0.136	0.045
11	3564	2.791	1770	0.274	0.098
12	3888	2.547	3032	0.376	0.148
13	4212	2.284	5124	0.494	0.216
14	4536	2.013	7081	0.555	0.276
15	4860	1.753	8848	0.596	0.340
16	5184	1.506	11008	0.617	0.410
17	5508	1.255	13908	0.611	0.486
18	5832	1.051	17123	0.603	0.574
19	6156	0.995	22670	0.685	0.689
		43.346		4.486	0.104

Table 5.2 Simulation results for $R = 8.125$ $\lambda = 0.825 \mu\text{m}$

m	Number of Rays	Total Power	Number of Rays lost	Power loss	Ratio
1	324	1	0	0	0
2	648	1.782	0	0	0
3	972	2.380	0	0	0
4	1296	2.815	0	0	0
5	1620	3.106	0	0	0
6	1944	3.269	0	0	0
7	2268	3.325	0	0	0
8	2592	3.289	0	0	0
9	2916	3.177	0	0	0
10	3240	3.007	147	0.0275	0.009
11	3564	2.791	860	0.129	0.046
12	3888	2.547	2174	0.260	0.102
13	4212	2.284	3570	0.355	0.155
14	4536	2.013	6011	0.446	0.222
15	4860	1.753	8255	0.498	0.284
16	5184	1.506	10182	0.543	0.361
17	5508	1.255	13471	0.553	0.440
18	5832	1.051	16443	0.551	0.525
19	6156	0.995	23737	0.654	0.657
		43.346		4.018	0.093

Table 5.3 Simulation results for $R = 9.125$ $\lambda = 0.825 \mu\text{m}$

m	Number of Rays	Total Power	Number of Rays lost	Power loss	Ratio
1	324	1	0	0	0
2	648	1.782	0	0	0
3	972	2.380	0	0	0
4	1296	2.815	0	0	0
5	1620	3.106	0	0	0
6	1944	3.269	0	0	0
7	2268	3.325	0	0	0
8	2592	3.289	0	0	0
9	2916	3.177	0	0	0
10	3240	3.007	0	0	0
11	3564	2.791	358	0.0465	0.017
12	3888	2.547	1356	0.149	0.058
13	4212	2.284	2720	0.252	0.111
14	4536	2.013	5059	0.361	0.179
15	4860	1.753	7071	0.426	0.243
16	5184	1.506	9998	0.477	0.317
17	5508	1.255	13371	0.510	0.406
18	5832	1.051	16800	0.520	0.494
19	6156	0.995	23582	0.623	0.625
		43.346		3.364	0.0776

Table 5.4 Simulation results for $R = 10.125 \text{ mm}$ $\lambda = 0.325 \text{ }\mu\text{m}$

representing that particular principal mode number. This is due to two reasons. First, all rays belonging to the same principal mode number have equal power. Secondly, rays reflected off the cladding/primary jacket interface can be considered as losses too as it is very unlikely for rays reentering the core to fulfill the conditions of a guided ray in a bent fiber. It also can be noted that for increasing values of R , the power loss comes from modes of higher principal numbers. Hence for large values of R , the power in the higher order modes play a significant role in deciding the bending loss.

For the second case of wrapping the fiber around the mandrel, experimental data are presented in Figs. 5.7 to 5.9. From Fig. 5.7, the power measured through the slit is lower than the first case indicating that some power has been removed from the core. The NFP drops off at a slightly faster rate than the first case and diminishes to zero at the edge of the core. Comparing the two MPDs, the peak distribution has shifted from $m = 7$ to $m = 6$, and less power is present in the higher order modes. Figs. 5.10 and 5.11 depict the bending losses and as expected, they are lower than the previous case. Again, sharp contrast is evident when compared to the simulation results.

5.2.2 Laser $1.3 \mu\text{m}$

The same two procedures were applied to the fiber when the $1.3 \mu\text{m}$ laser source was used to excite the fiber. The results for the first case are shown in Figs. 5.12 to 5.16. Tables 5.5 to 5.8 shows a sample of the simulations results.

With the fiber wrapped around the mandrel, the experimental

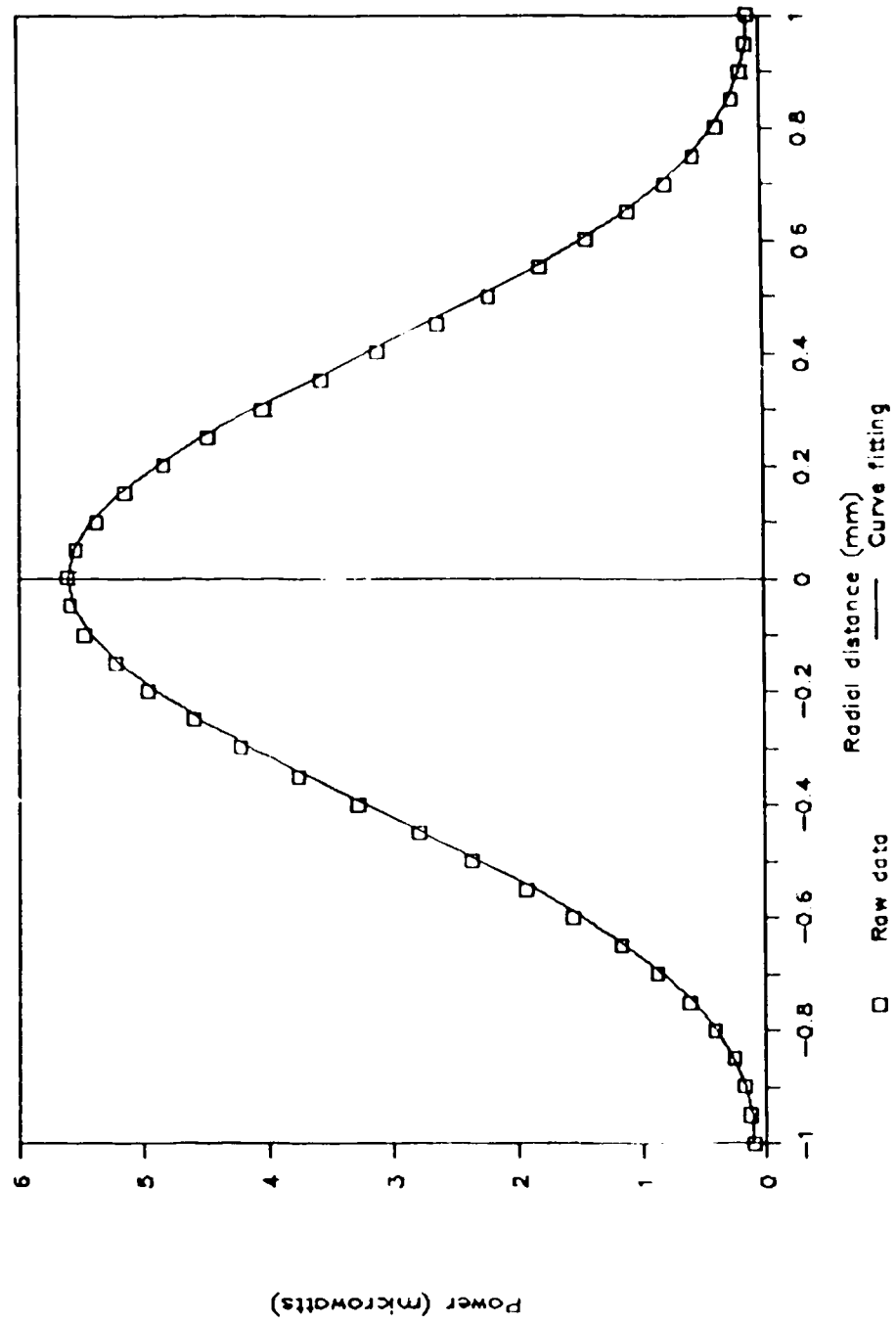


Fig. 5.7 Experimental and curve-fitted results from the slit experiment for the first of the two 0.825 μm laser sources. Fiber was wrapped around a mandrel

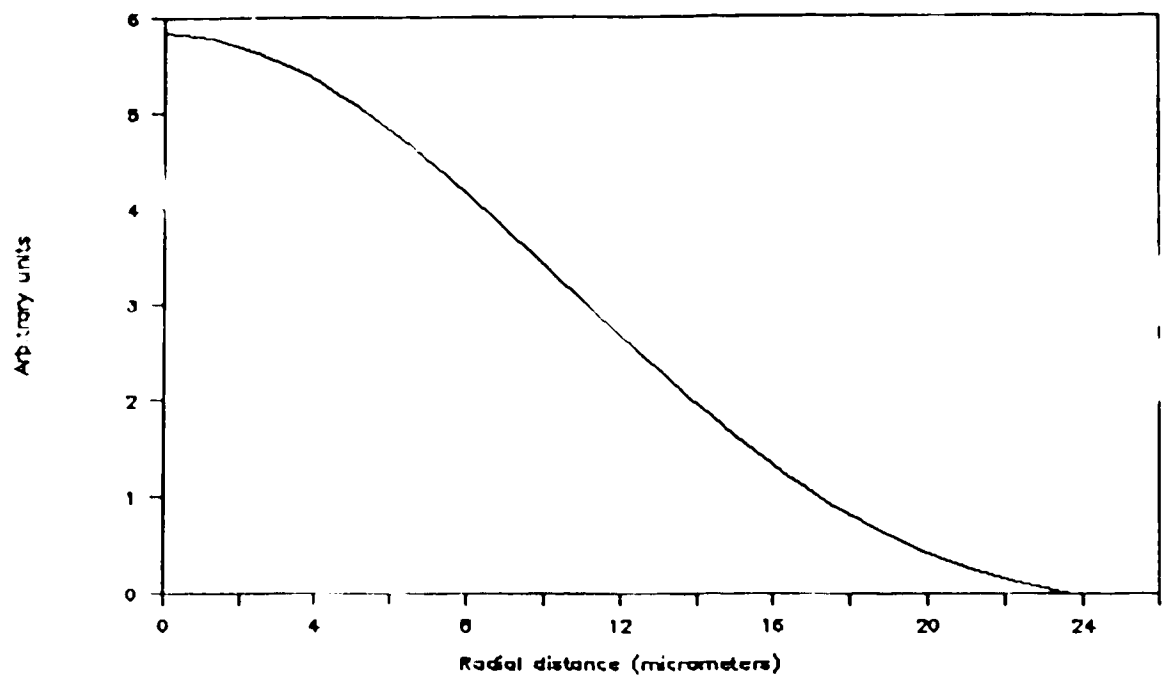


Fig. 5.8 The near-field pattern derived from Fig. 5.7

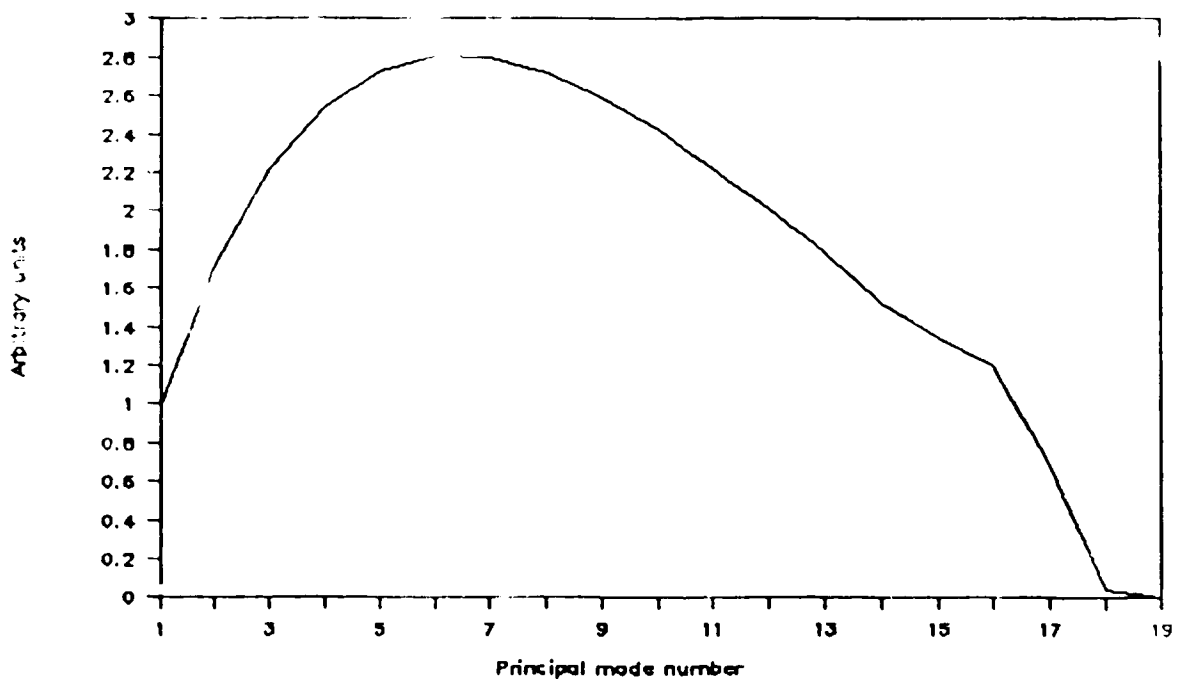


Fig. 5.9 The modal power distribution derived from Fig. 5.8

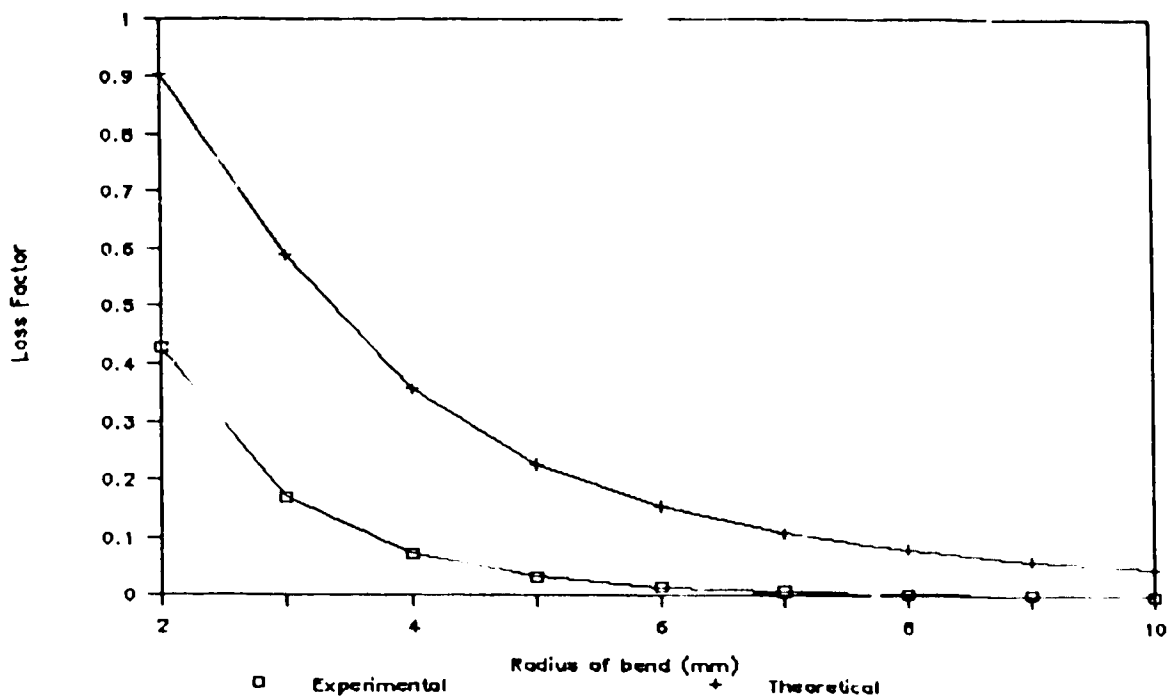


Fig. 5.10 Experimental and theoretical bending losses for modal power distribution in Fig. 5.4. Experimental uncertainty of 15% in all loss measurements.

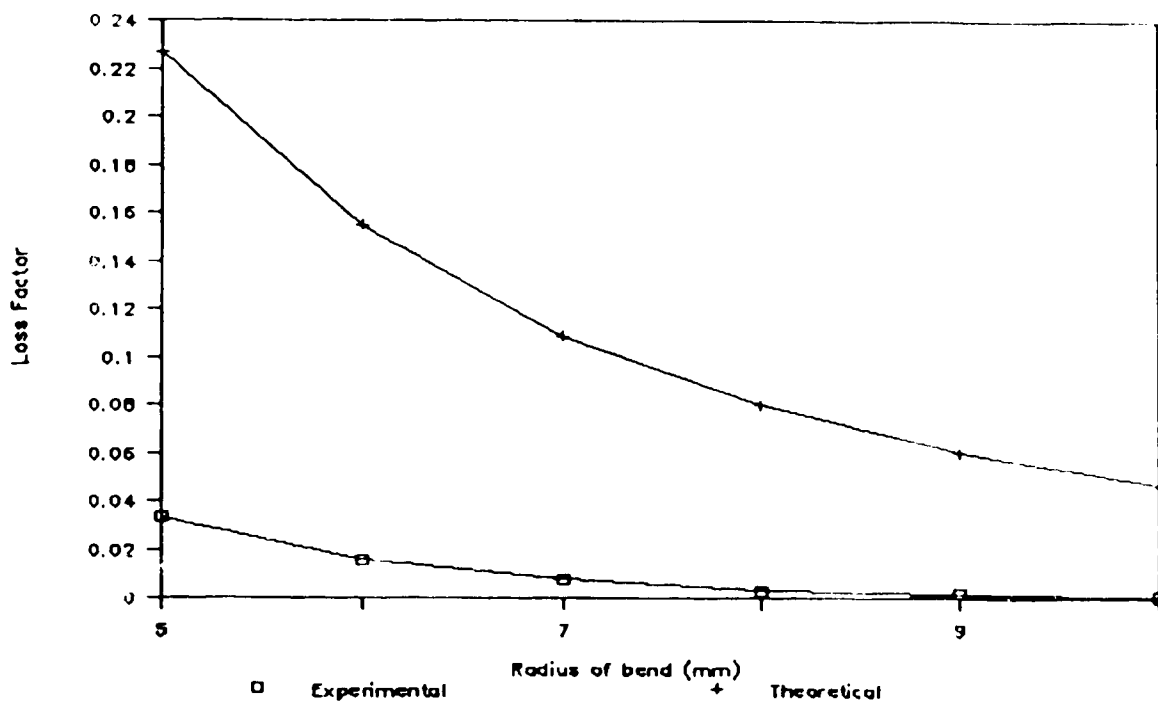


Fig. 5.11 Exploded comparison from Fig. 5.10

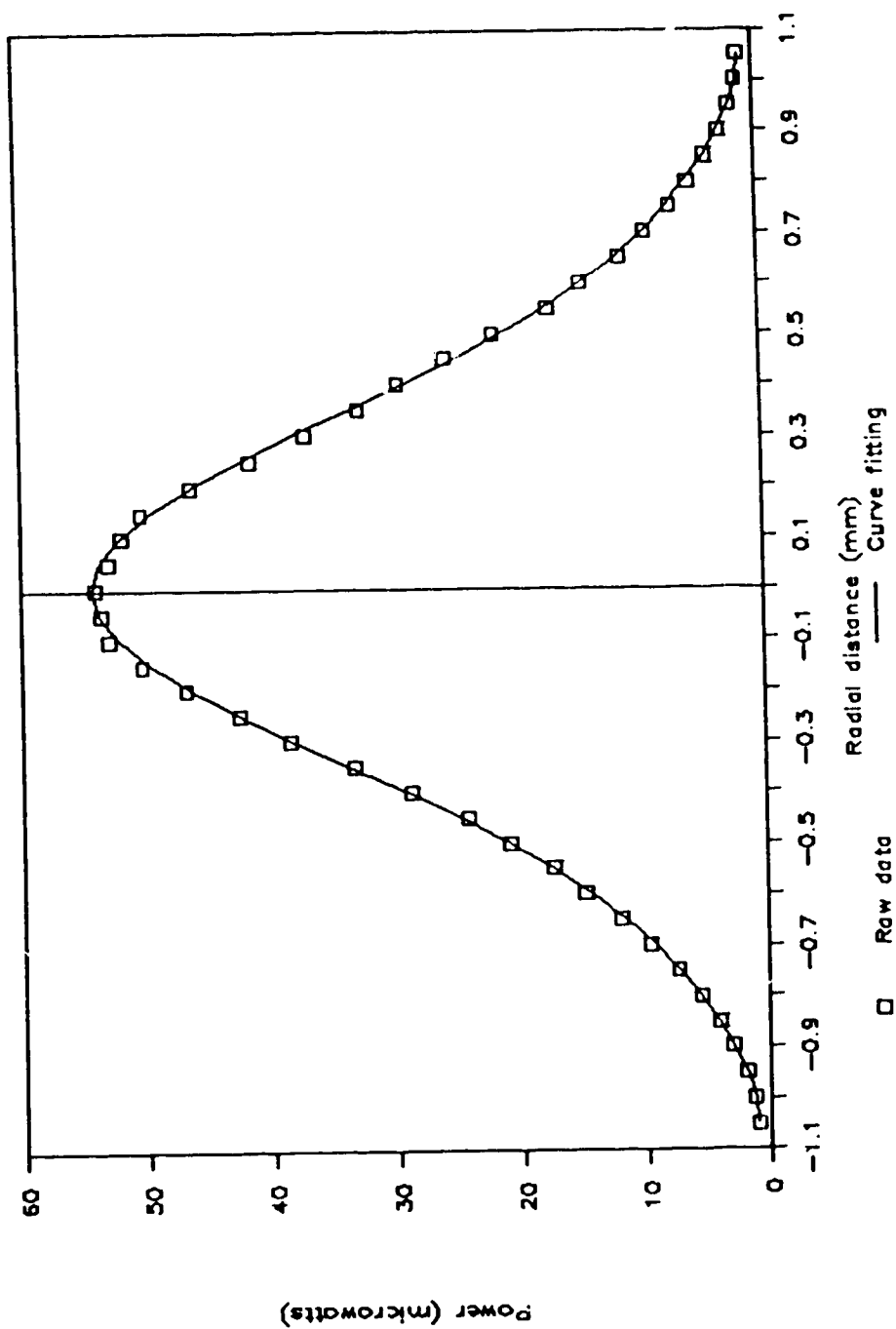


Fig. 5.12 Experimental and curve-fitted results from the slit experiment for the 1.3 μm laser source

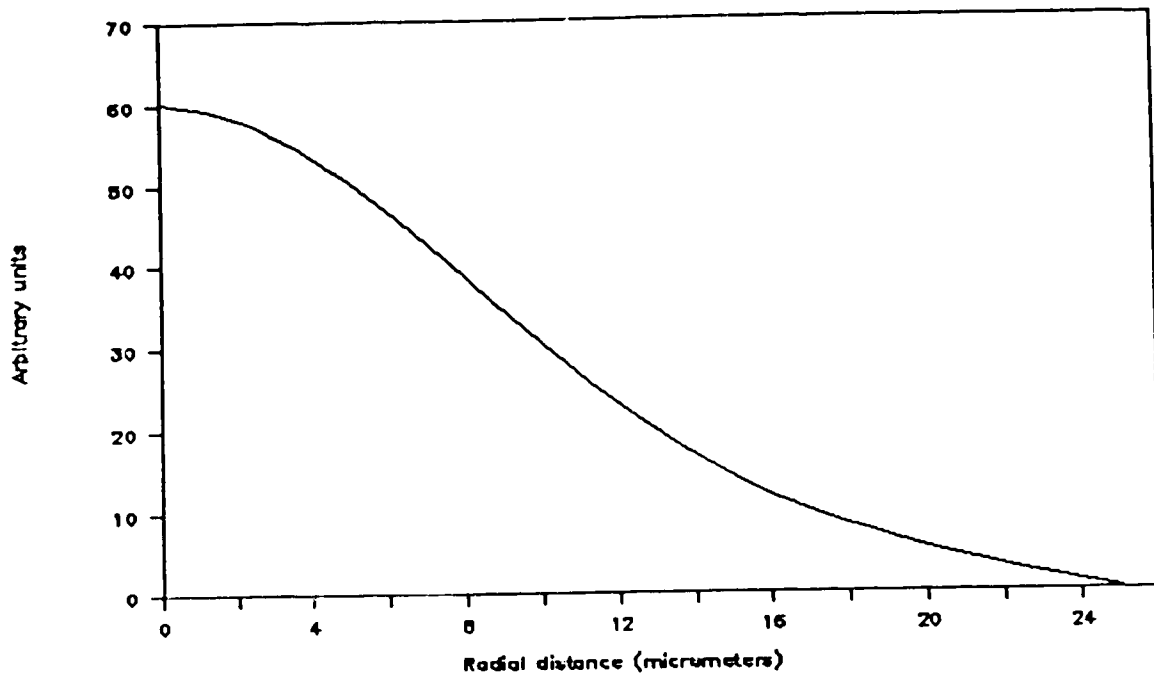


Fig. 5.13 The near-field pattern derived from Fig. 5.12

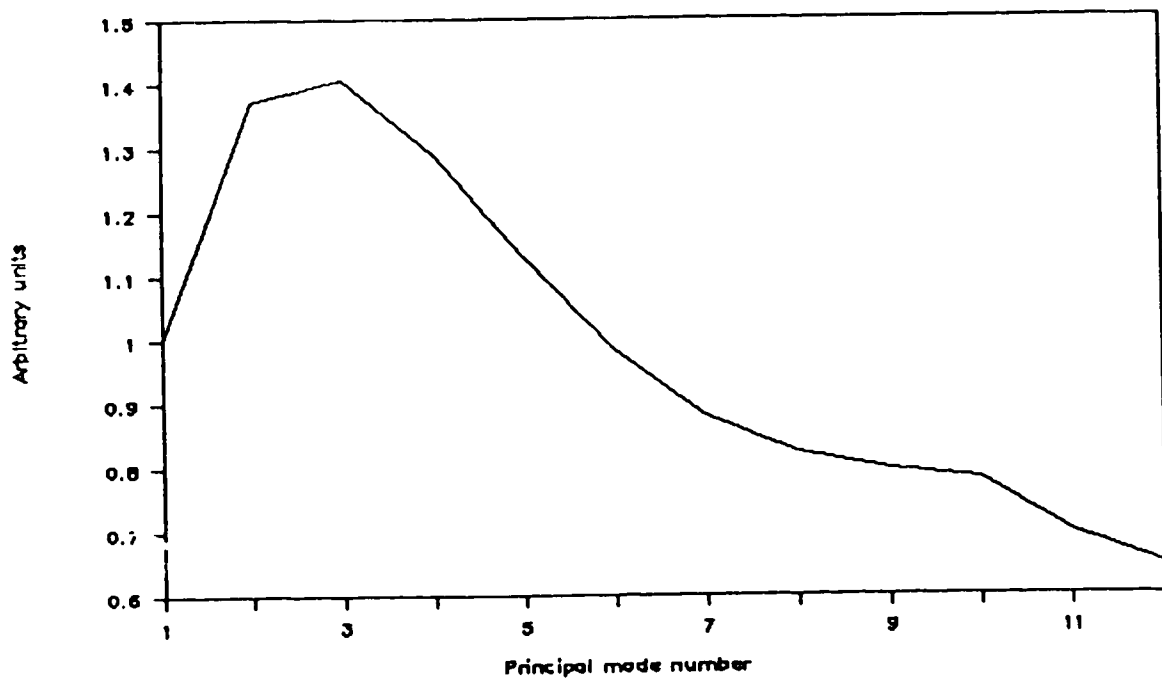


Fig. 5.14 The modal power distribution derived from Fig. 5.13

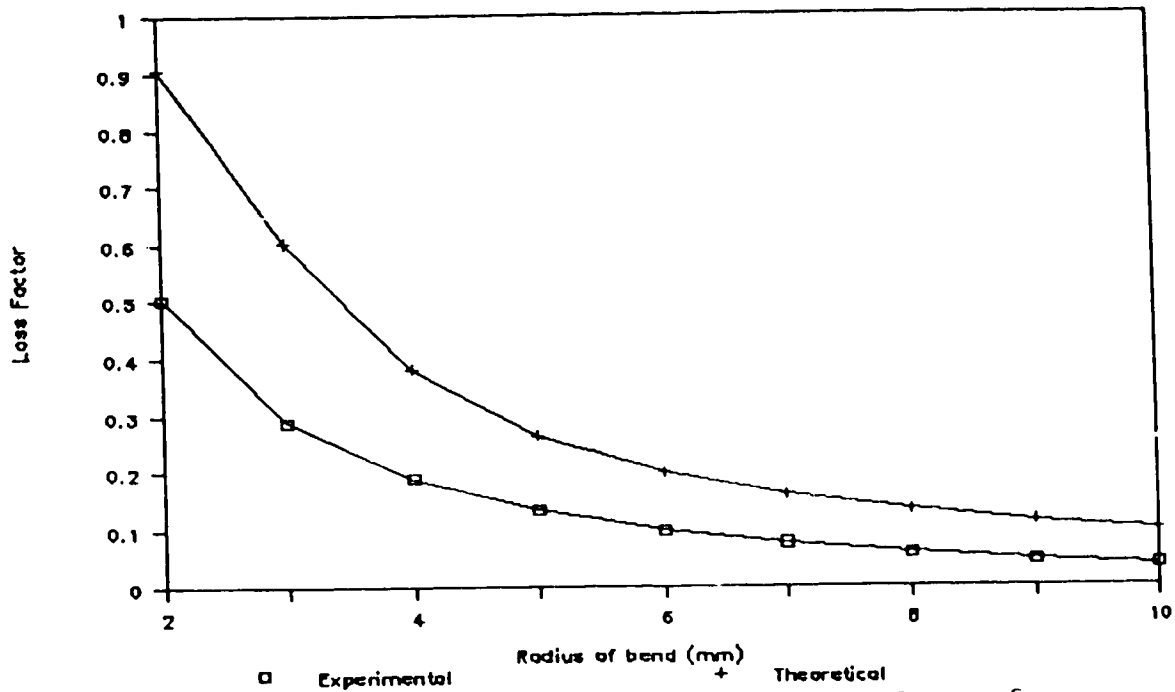


Fig. 5.15 Experimental and theoretical bending losses for modal power distribution in Fig. 5.4. Experimental uncertainty of 15% in all loss measurements.

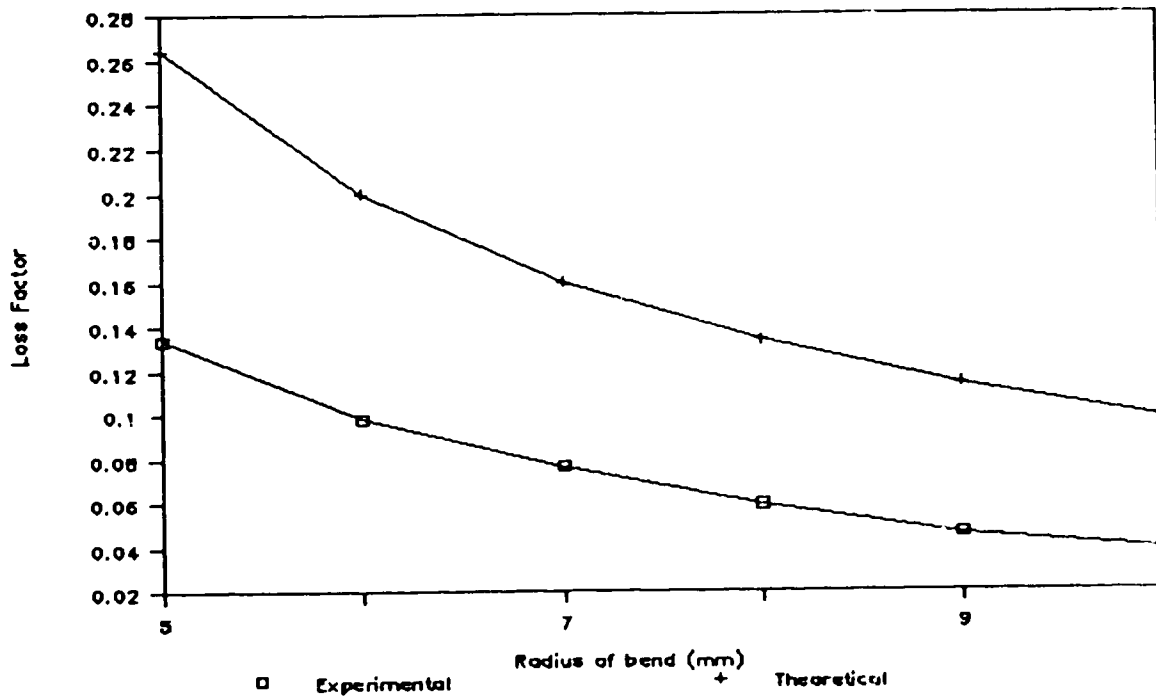


Fig. 5.16 Exploded comparison from Fig. 5.15

m	Number of Rays	Total Power	Number of Rays lost	Power loss	Ratio
1	324	1	0	0	0
2	648	1.371	0	0	0
3	972	1.408	0	0	0
4	1296	1.291	0	0	0
5	1620	1.130	28	0.0042	0.004
6	1944	0.984	713	0.0742	0.075
7	2268	0.881	1746	0.135	0.153
8	2592	0.826	3438	0.209	0.253
9	2916	0.799	5056	0.270	0.337
10	3240	0.784	7072	0.350	0.447
11	3564	0.699	9768	0.391	0.559
12	3888	0.648	14156	0.460	0.709
		11.822		1.893	0.160

Table 5.5 Simulation result for $R = 7.125 \text{ mm}$, $\lambda = 1.3 \text{ }\mu\text{m}$

m	Number of Rays	Total Power	Number of Rays lost	Power loss	Ratio
1	324	1	0	0	0
2	648	1.371	0	0	0
3	972	1.408	0	0	0
4	1296	1.291	0	0	0
5	1620	1.130	0	0	0
6	1944	0.984	200	0.020	0.020
7	2268	0.881	1144	0.088	0.100
8	2592	0.826	2628	0.152	0.184
9	2916	0.799	4780	0.226	0.283
10	3240	0.784	6644	0.305	0.389
11	3564	0.699	9366	0.354	0.506
12	3888	0.648	14324	0.345	0.671
		11.822		1.580	0.134

Table 5.6 Simulation result for $R = 8.125 \text{ mm}$, $\lambda = 1.3 \text{ } \mu\text{m}$

m	Number of Rays	Total Power	Number of Rays lost	Power loss	Ratio
1	324	1	0	0	0
2	648	1.371	0	0	0
3	972	1.408	0	0	0
4	1296	1.291	0	0	0
5	1620	1.130	0	0	0
6	1944	0.984	0	0	0
7	2268	0.881	528	0.040	0.045
8	2592	0.826	1912	0.110	0.133
9	2916	0.799	4098	0.185	0.232
10	3240	0.784	6332	0.268	0.342
11	3564	0.699	9440	0.328	0.469
12	3888	0.648	14995	0.416	0.641
		11.822		1.346	0.114

Table 5.7 Simulation result for $R = 9.125 \text{ mm}$, $\lambda = 1.3 \text{ }\mu\text{m}$

m	Number of Rays	Total Power	Number of Rays lost	Power loss	Ratio
1	324	1	0	0	0
2	648	1.371	0	0	0
3	972	1.408	0	0	0
4	1296	1.291	0	0	0
5	1620	1.130	0	0	0
6	1944	0.984	0	0	0
7	2268	0.881	196	0.012	0.014
8	2592	0.826	1346	0.074	0.089
9	2916	0.799	3299	0.149	0.187
10	3240	0.784	6018	0.227	0.289
11	3564	0.699	9359	0.305	0.436
12	3888	0.648	14766	0.394	0.607
		11.822		1.160	0.098

Table 5.8 Simulation result for $R = 10.125 \text{ mm}$ $\lambda = 1.3 \text{ }\mu\text{m}$

results are shown in Figs. 5.17 to 5.21. As expected with the mandrel wrap, the MPD indicates a lower concentration of power for higher order modes. This resulted in lower bending losses for the fiber as shown in Figs. 5.20 and 5.21.

5.2.3 Laser II 0.825 μm

For the last laser source no attempts to alter the MPD were made. The results are shown in Figs. 5.22 to 5.26. In this case, there is a greater power concentration in the higher order modes unlike the previous two sources. With such a MPD, the bending losses are expected to be greater than before for the same R and this is shown to be true in Figs. 5.25 and 5.26.

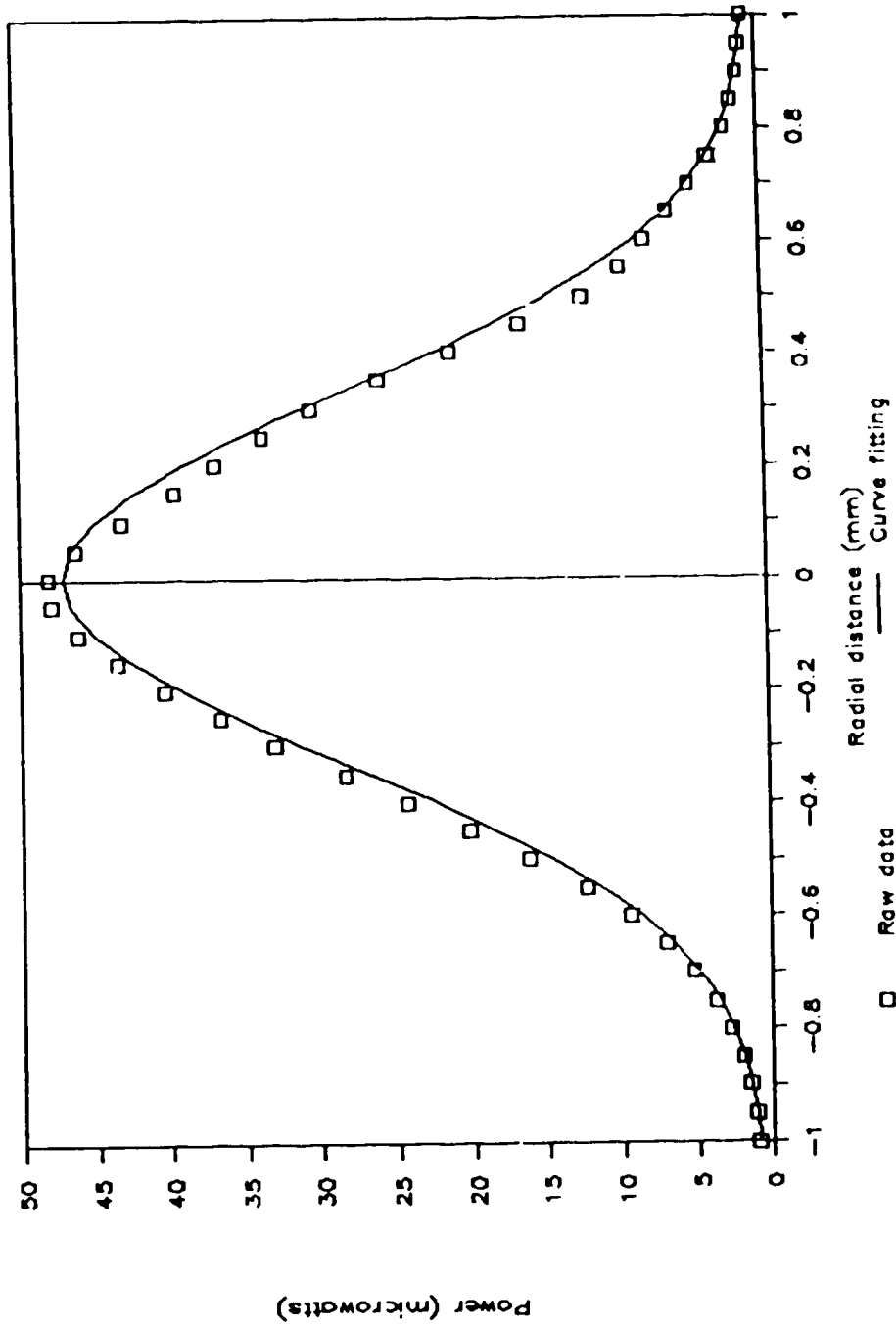


Fig. 5.17 Experimental and curve-fitted results from the slit experiment for the 1.3 μm laser source. Fiber was wrapped around a mandrel

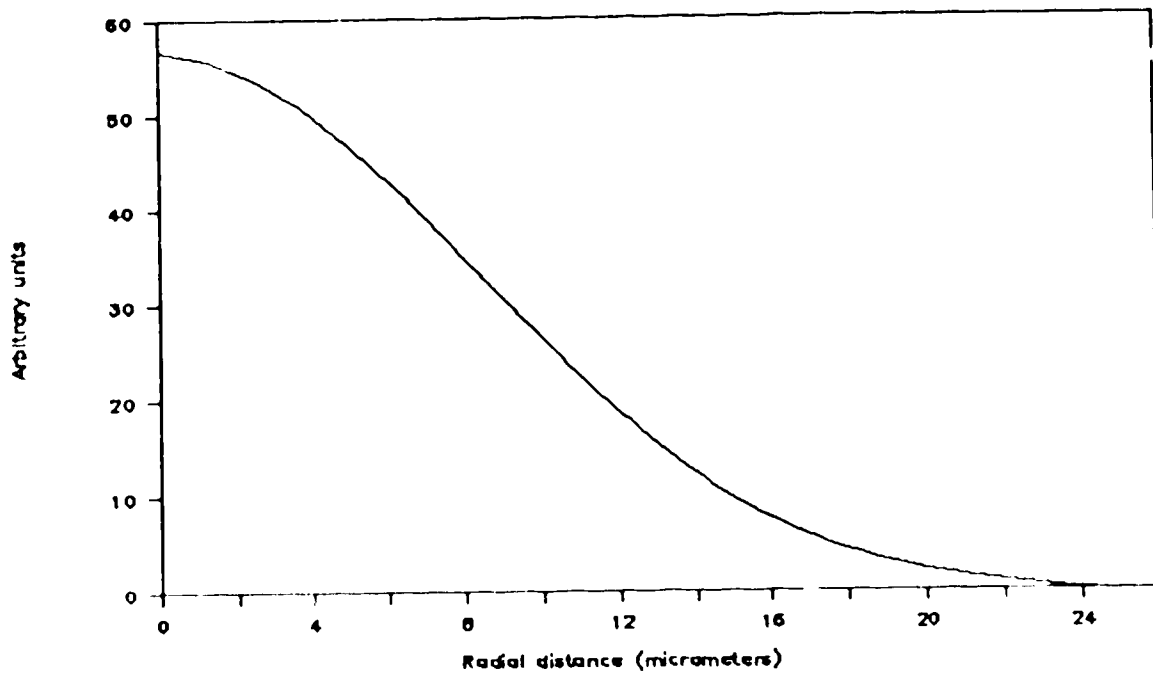


Fig. 5.18 The near-field pattern derived from Fig. 5.17

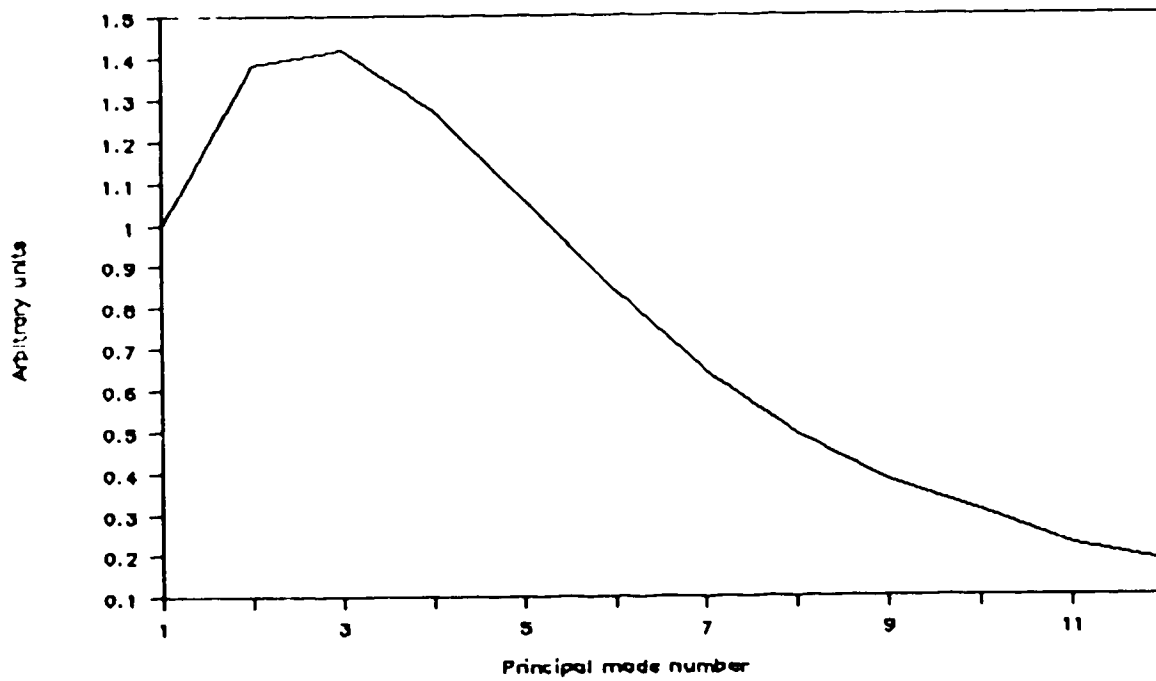


Fig. 5.19 The modal power distribution derived from Fig. 5.18

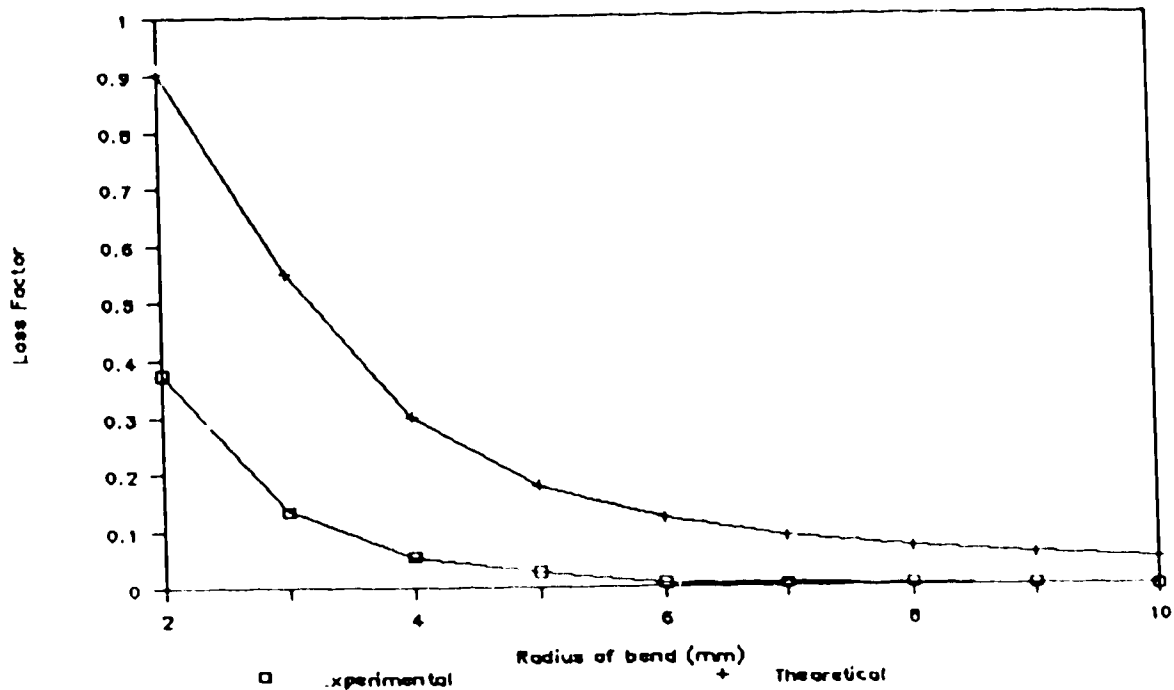


Fig. 5.20 Experimental and theoretical bending losses for modal power distribution in Fig. 5.4. Experimental uncertainty of 15% in all loss measurements.

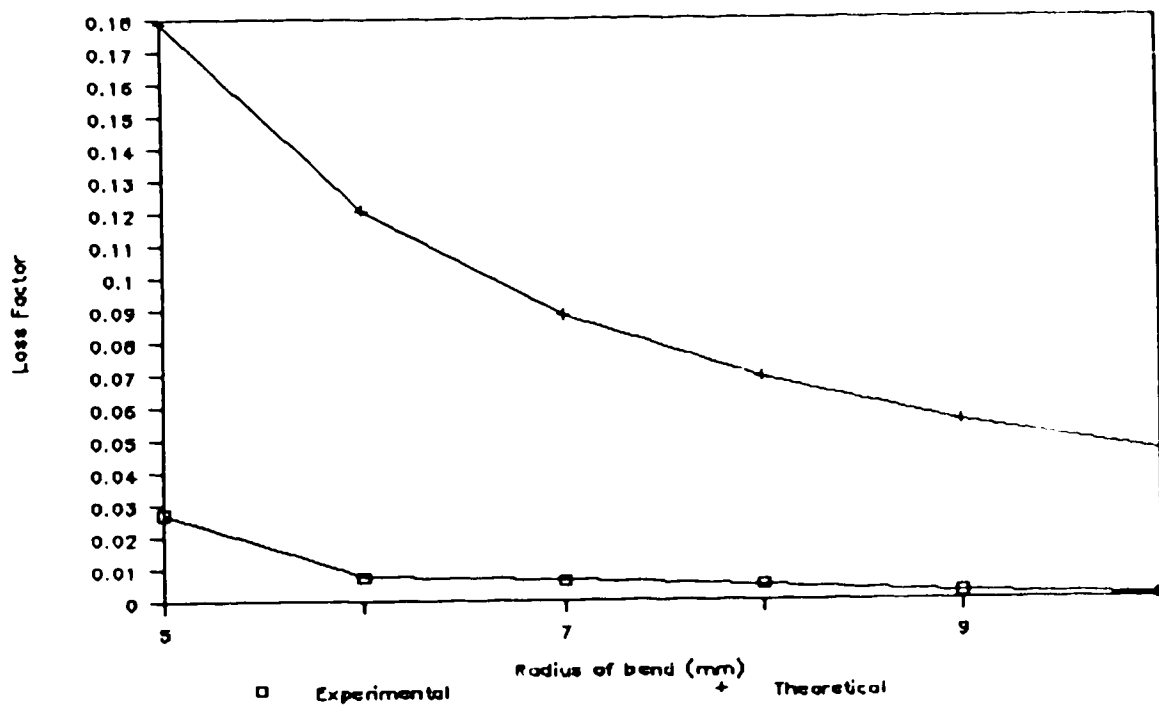


Fig. 5.21 Exploded comparison from Fig. 5.20

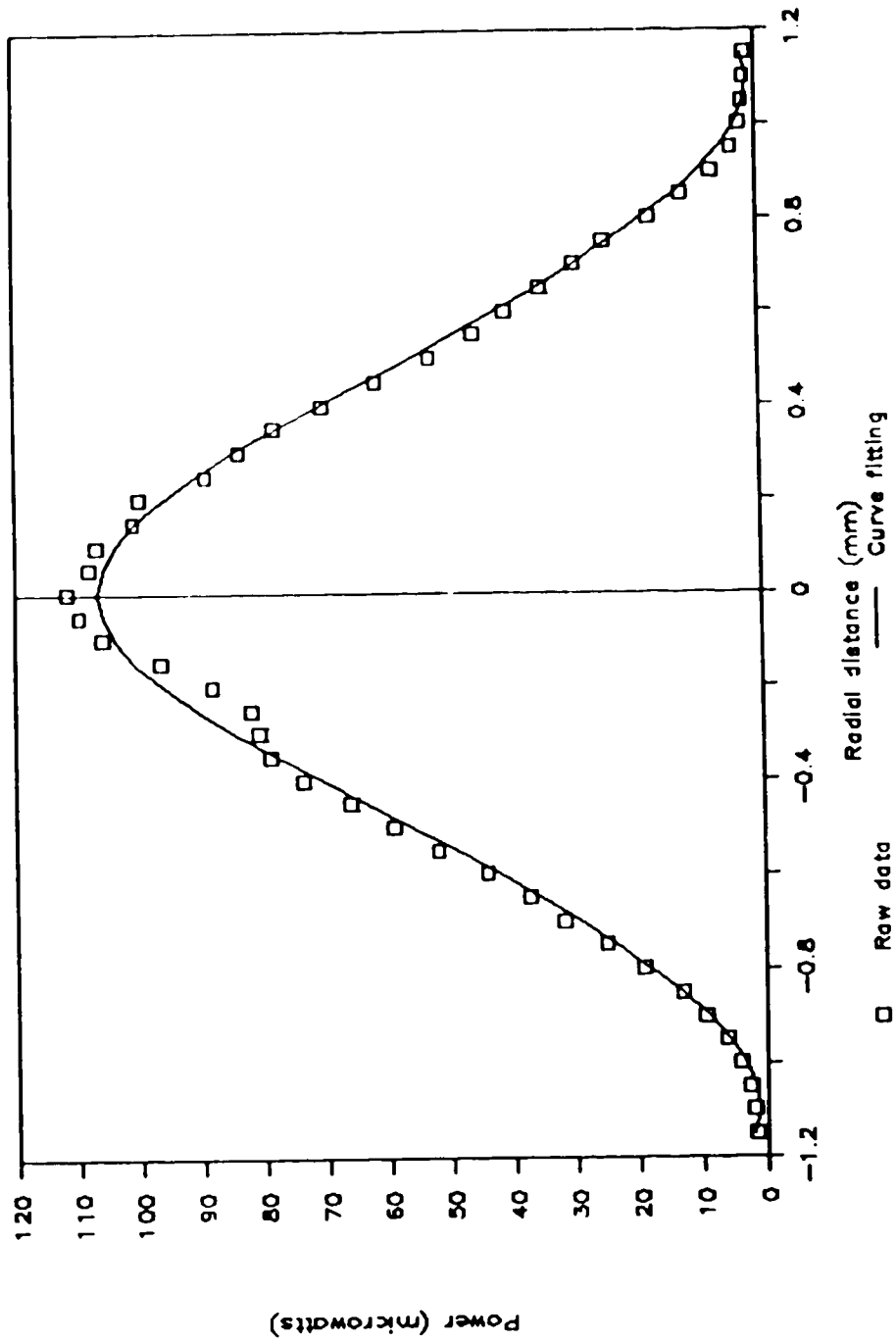


Fig. 5.22 Experimental and curve-fitted results from the slit experiment for the second of the two $0.825 \mu\text{m}$ laser sources

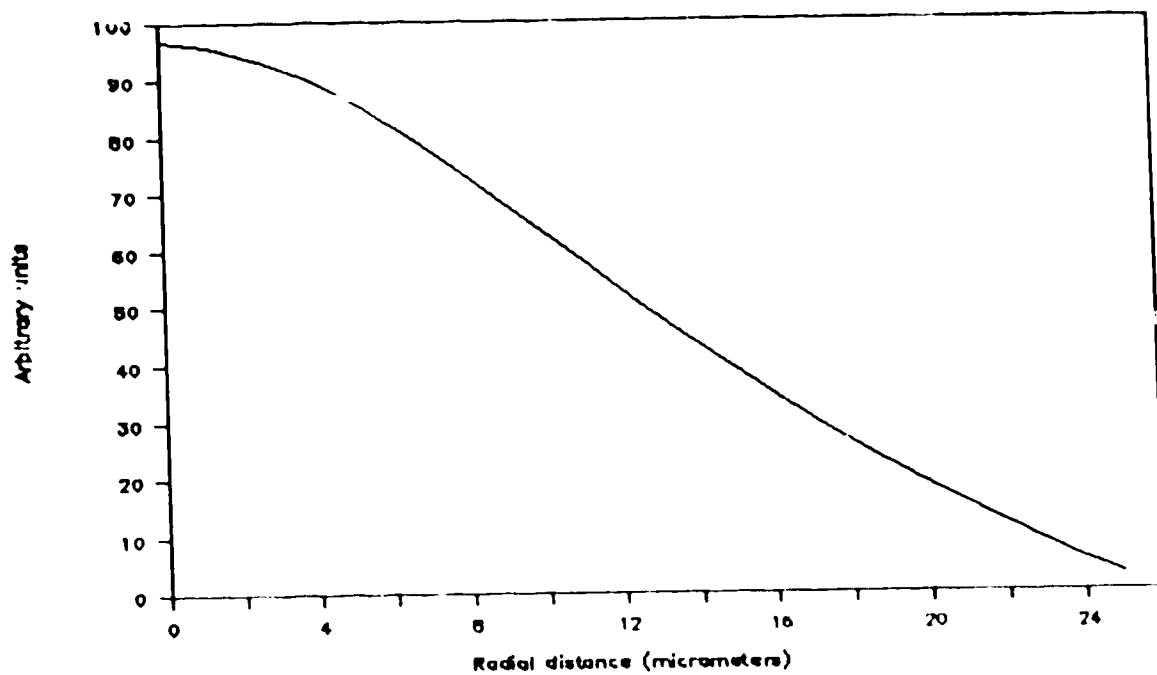


Fig. 5.23 The near-field pattern derived from Fig. 5.22

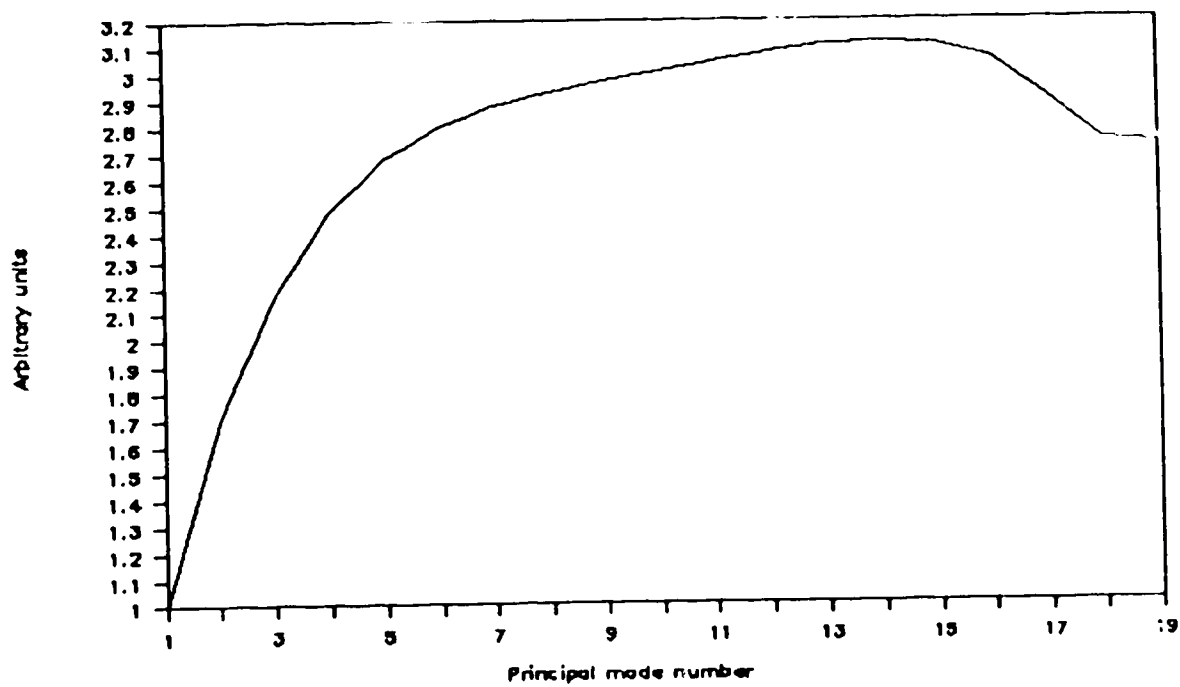


Fig. 5.24 The modal power distribution derived from Fig. 5.23

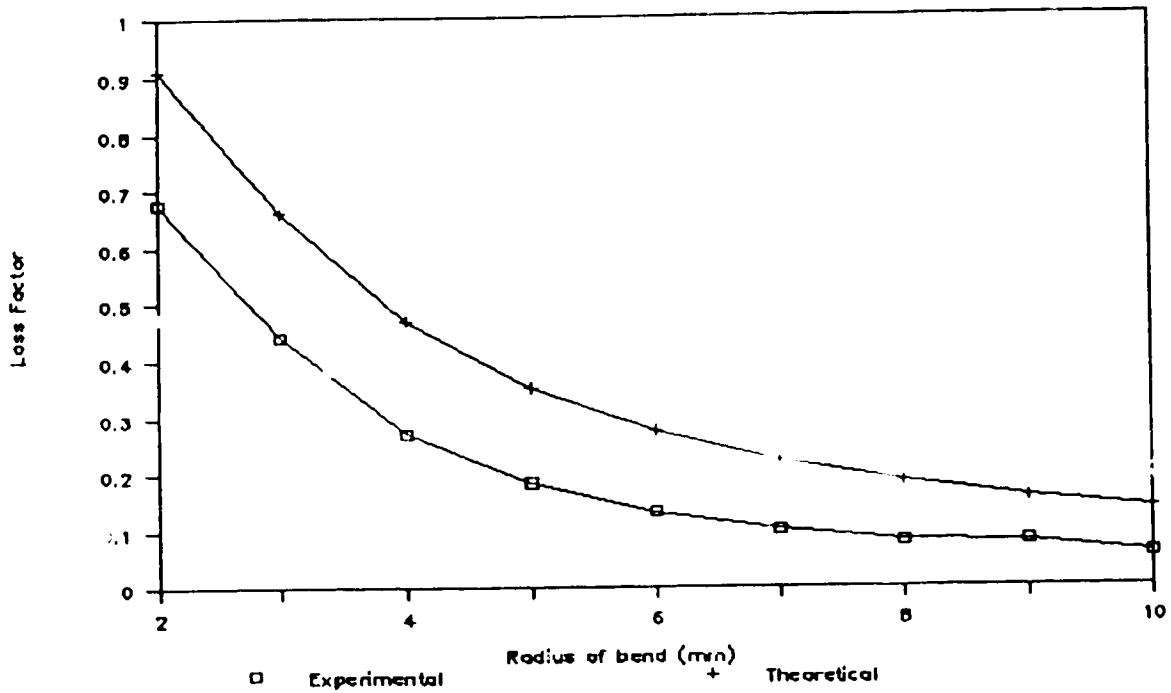


Fig. 5.25 Experimental and theoretical bending losses for modal power distribution in Fig. 5.4. Experimental uncertainty of 15% in all loss measurements.

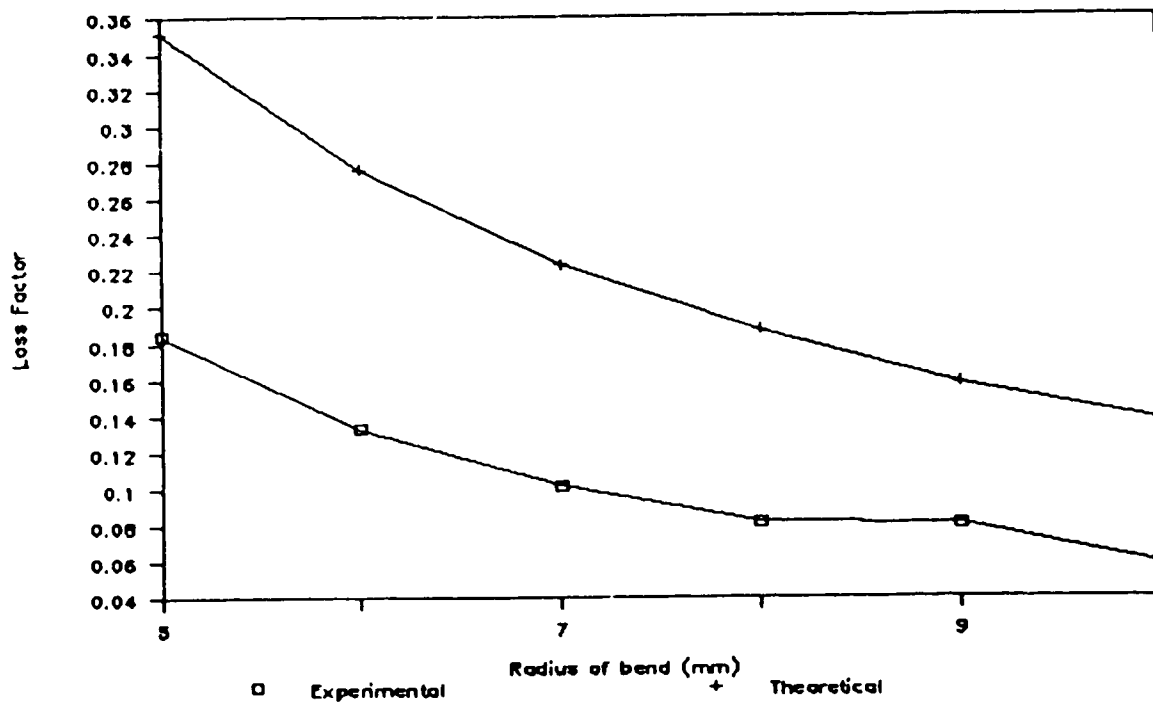


Fig. 5.26 Exploded comparison from Fig. 5.25

5.2.4 Theoretical comparison with a lambertian source

In this section, the simulated bending losses for all 5 cases are compared to the case of a fiber excited with a lambertian source. From Chapter 3, it was shown that the near-field pattern of a multimode parabolic graded-index fiber excited by a lambertian source has the same profile as the refractive index. Therefore, the MPD increases linearly with the principal mode number. Fig. 5.27 and 5.28 show the comparison for the 0.825 μm and 1.3 μm laser sources respectively. It is beyond any doubt that in predicting the bending losses of a multimode mode, it is necessary to take into account the MPD.

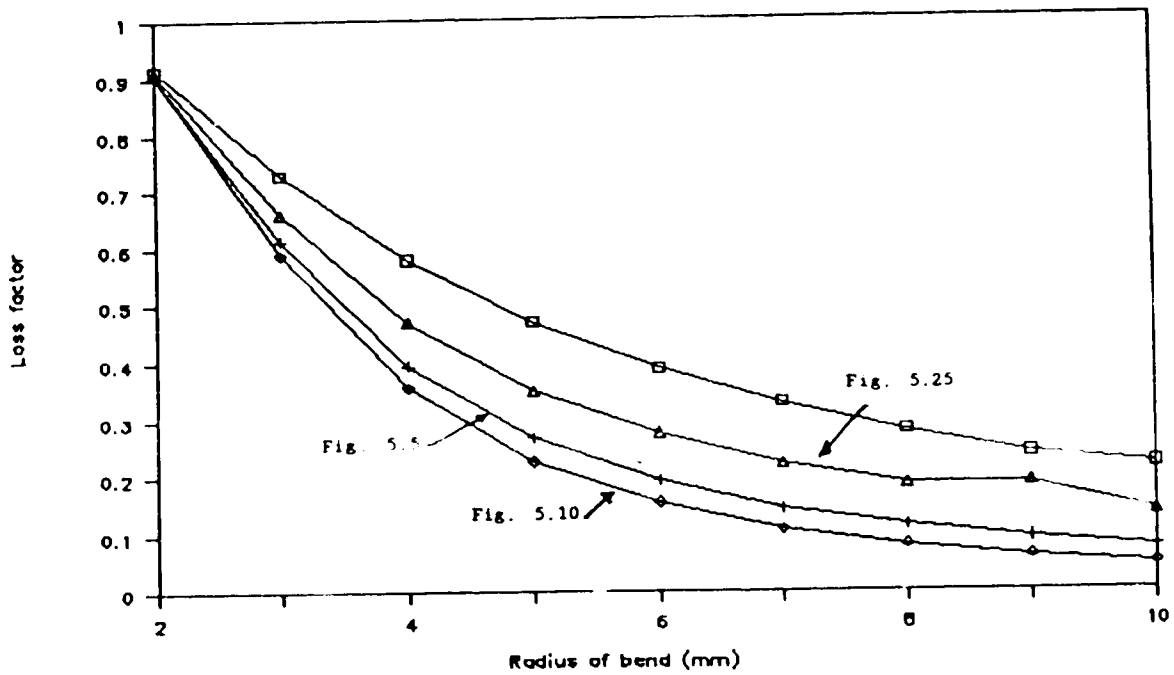


Fig. 5.27 Theoretical comparison with a lambertian source (□) at 0.825 μm

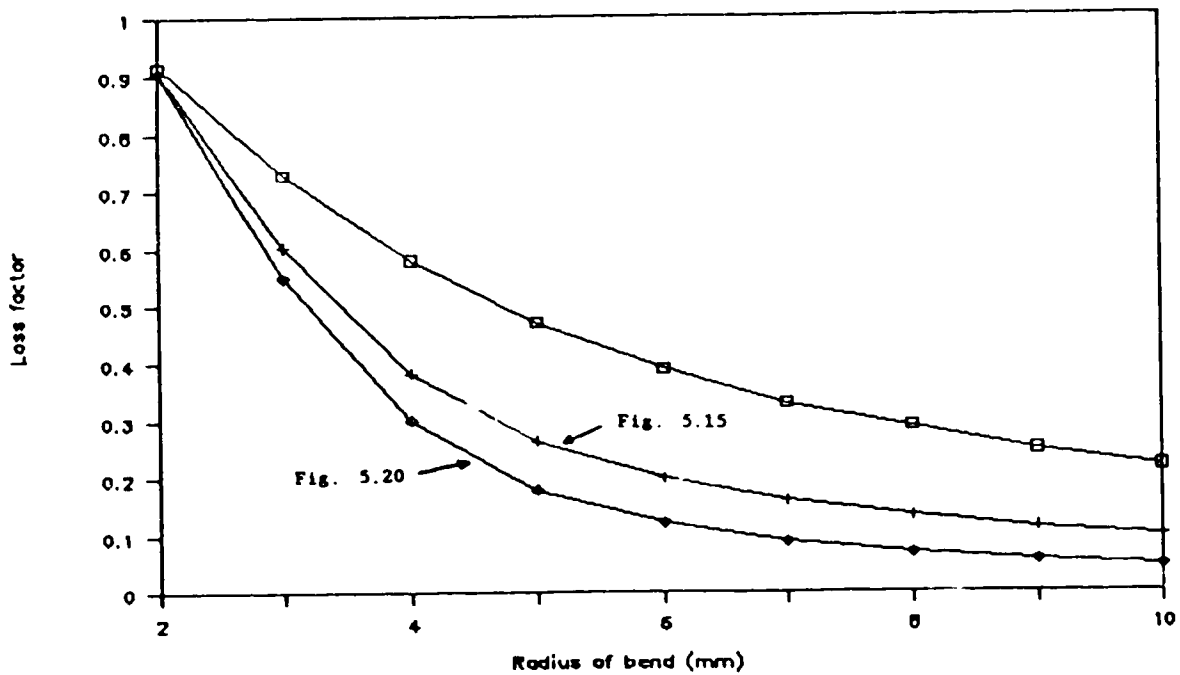


Fig. 5.28 Theoretical comparison with a lambertian source (□) at 1.3 μm

5.3 Radiation patterns

As mentioned previously, only the radiation patterns from a bent fiber excited with a $0.825 \mu\text{m}$ laser source were measured. This is to roughly determine the position of the peak intensity and compare it with theory. Only a one-dimensional radiation pattern measurement was performed. The detector is placed symmetrically around the x axis and parallel to the y axis (see Chapter 4 and coordinate system of Fig. 4.5). Hence for a fixed value of z, the intensity as a function of y can be measured. A two-dimensional scan was not possible due to the nature of the device. It was designed with a height (the x-coordinate) equal to that of the detector. Ideally, the device should have sufficient height to avoid having the diverging beam meet the edges of the device prior to reaching the detector. Therefore, the experimental and theoretical radiation patterns will not exactly portray the same situation. The conventional hermetically-sealed detector packages were not used due to their bulkiness. Instead, unpackaged detectors in chip form were utilised. The detector was mounted on a non-conducting block and wired using silver epoxy. The block was attached to a xyz positioner to provide movement near the bend. The detector was reversed biased at 10 volts with a $10 \text{ k}\Omega$ load resistor (see appendix for data sheets). The experimental setup to measure the radiation pattern is shown in Fig. 5.29. To avoid the effects of convolution, the detector was masked with a pinhole of approximately 0.8 mm in diameter. A slit was not used as a cylindrical radiation pattern is not expected whereby the inverse Abel transform is not applicable.

The radiation patterns measured as a function of y for

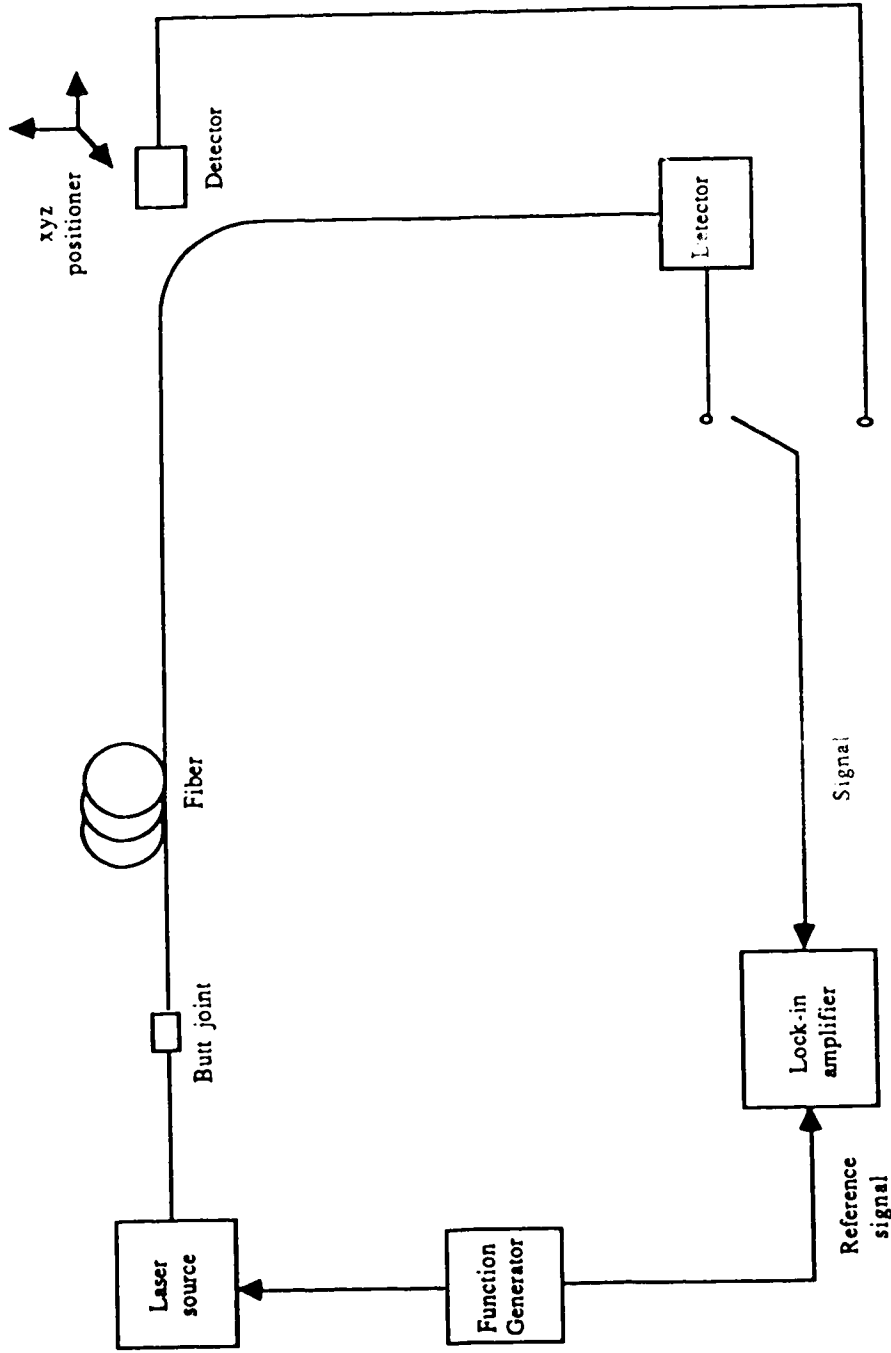


Fig. 5.29 Scanning of the radiation pattern from a bent fiber

$R = 7.125$ mm and 10.125 mm were performed with z set at 8 mm and 11 mm respectively. Figs. 5.30 and 5.31 depict radiation patterns for an external fluid with a refractive index of 1.50 . Both patterns exhibit an initial peak and a few subsequent smaller peaks. The initial peak is expected as the power of initial rays that leave the fiber are the most intense. The subsequent smaller peaks are due to rays reflected off the cladding/primary jacket interface that eventually find their way to the exterior. The initial peak for the case of $R = 7.125$ mm is roughly at $z = 7.54$ mm while for $R = 10.125$ mm, the peak occurs at roughly $z = 10.1$ mm. The corresponding simulated radiation patterns are shown in Figs. 5.32 and 5.33. Both figures exhibit somewhat similar initial peaks followed by another peak or two. Peaks occur at $z = 8.00$ mm and $z = 11.5$ mm for the $R = 7.125$ mm and $R = 10.125$ mm respectively.

The experimental radiation patterns for an external fluid of 1.538 are shown in Figs. 5.34 and 5.35. Compared to the experimental case of 1.50 as the external fluid, the profiles are almost identical except for a positive horizontal shift. As the refractive index of the fluid increases, the angle the refracted ray makes with the radial vector decreases (see Chapter 2), hence the shift. The peak occurs at $z = 8.4$ mm and at $z = 11.3$ mm for $R = 7.125$ mm and $R = 10.125$ mm respectively. The corresponding simulated radiation patterns are shown in Fig. 5.36 and 5.37 with their respective peaks at $z = 8.8$ mm and $z = 12.5$ mm. The simulated radiation patterns, although not depicting the experimental results exactly, are good approximations. Remember that the resolution of the radiation pattern is limited by the size of the pinhole.

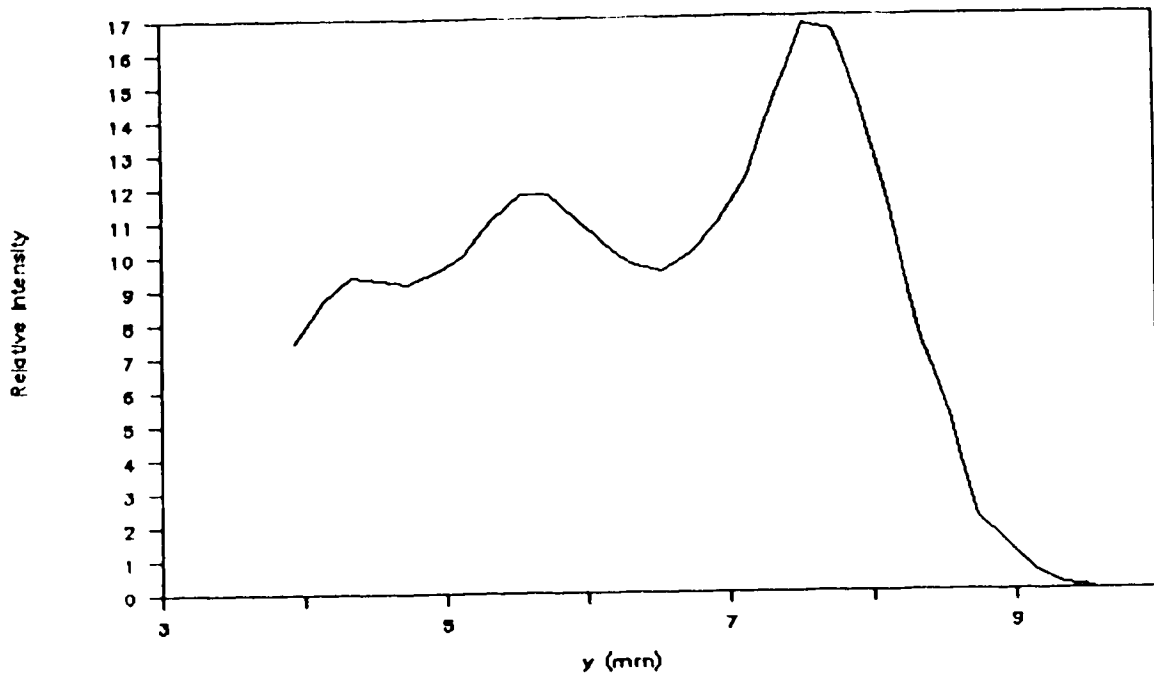


Fig. 5.30 Power as a function of y for $z = 8$ mm (see coordinate system Fig. 4.5) with $R = 7.125$ mm and $n_{\text{fluid}} = 1.50$

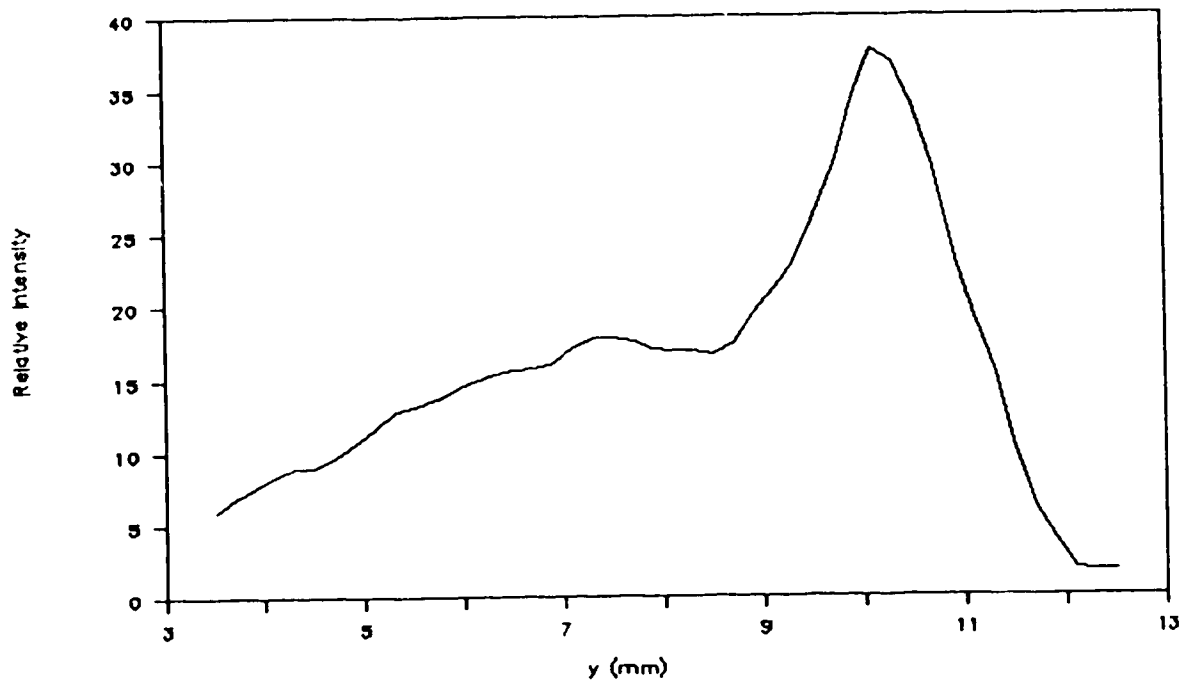


Fig. 5.31 Power as a function of y for $z = 11$ mm (see coordinate system Fig. 4.5) with $R = 10.125$ mm and $n_{\text{fluid}} = 1.50$

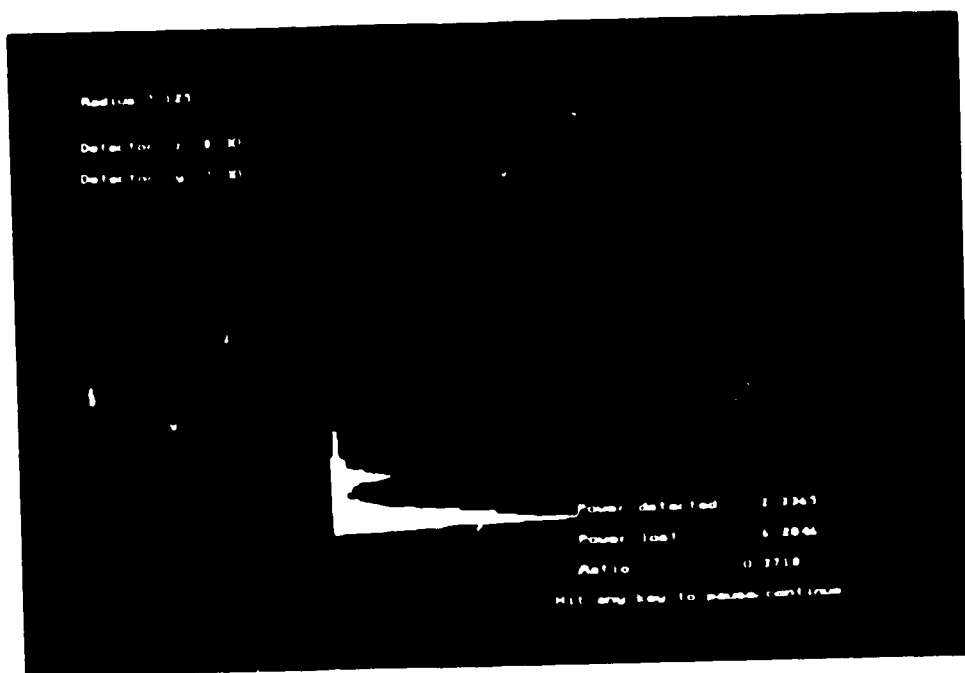


Fig. 5.32 Simulated radiation pattern for same case as in Fig. 5.30

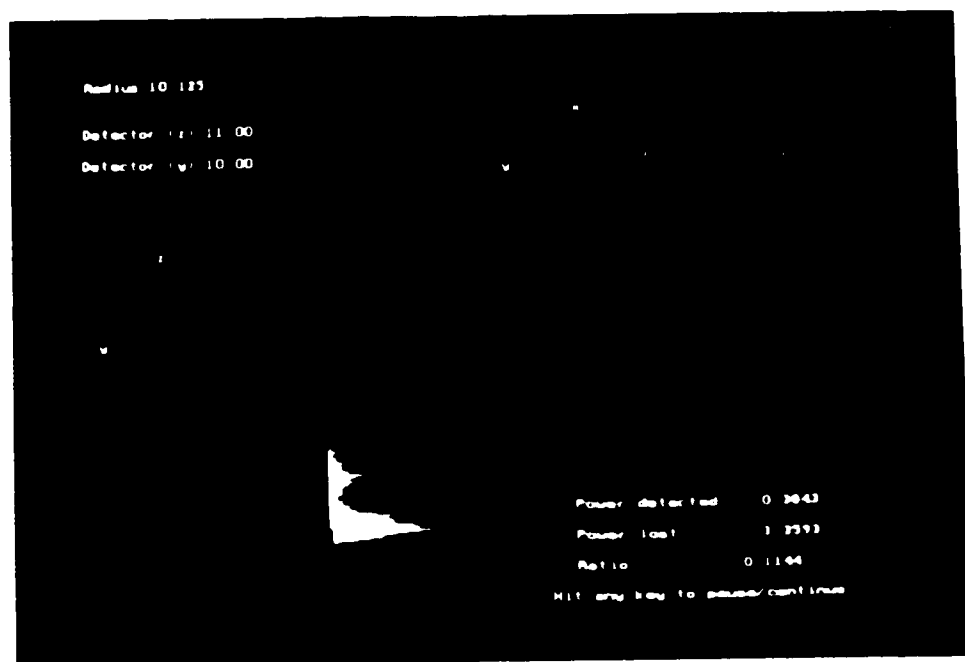


Fig. 5.33 Simulated radiation pattern for same case as in Fig. 5.31

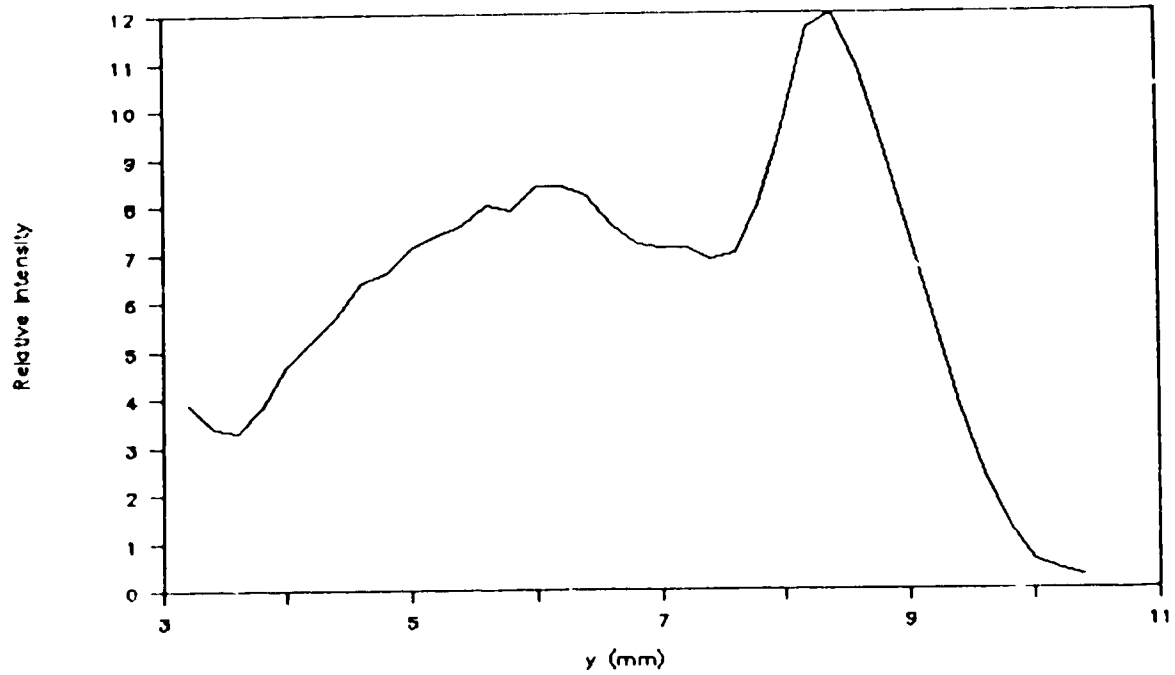


Fig. 5.34 Power as a function of y for $z = 3$ mm with $R = 7.125$ mm and $n_{\text{fluid}} = 1.538$.

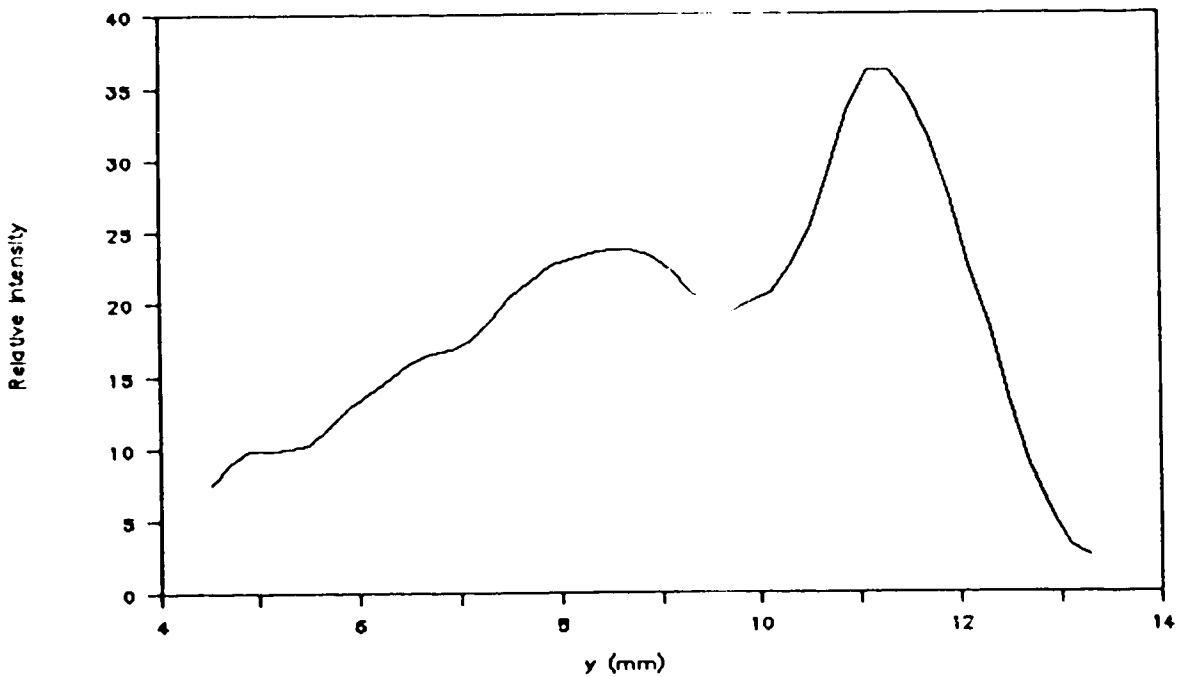


Fig. 5.35 Power as a function of y for $z = 11$ mm with $R = 10.125$ mm and $n_{\text{fluid}} = 1.538$.

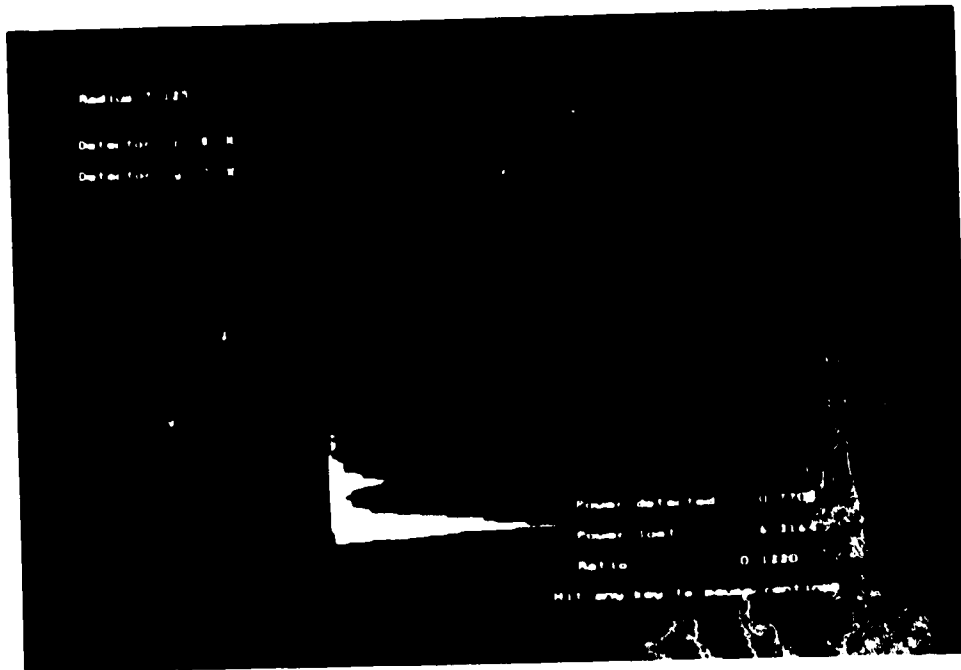


Fig. 5.36 Simulated radiation pattern for same case as in Fig. 5.34

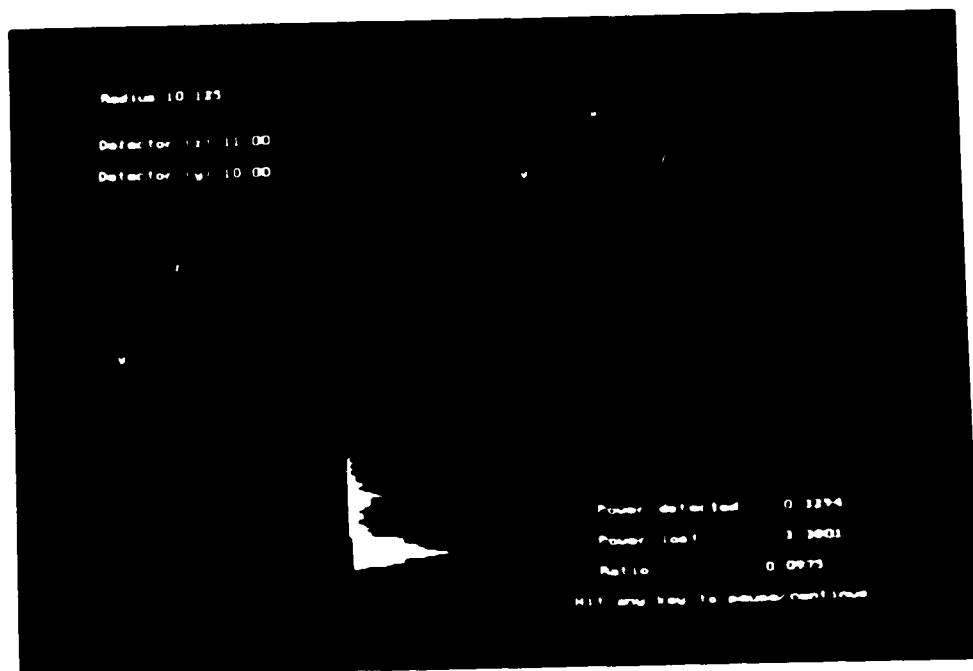


Fig. 5.37 Simulated radiation pattern for same case as in Fig. 5.35

5.4 Discrepancy between experimental and theoretical results

From the results presented in Sections 5.2 and 5.3, major discrepancies between the experimental and simulated bending losses are evident. In this section, the factors that may contribute to the discrepancies are discussed.

Recall that three assumptions were made in developing the simulation program (see Section 4.2). Since leaky rays and tunnelling effects are not taken into consideration, the simulation program should ideally predict a lower loss than experimental results. However, for all cases, the simulation program over-predicts the bending losses.

5.4.1 Numerical accuracy of simulation

First possible explanation for the discrepancy of the bending losses is the number of rays representing a mode may be inadequate. Three methods of increasing the number of rays were investigated:

1. increase the value of L , see eqn. (3.27)
2. increase the number of combinations of i and j , see eqn. (3.26). Instead of using a step size of 1, a smaller step size of 0.25 was used
3. combination of 1 and 2.

In the first case, the value of L was increased to 30. This increases the number of (x, y) and (k_x, k_y) values for each ring in both r and k space. For the MPD shown in Fig. 5.4, the simulation results for $R = 10$ mm is tabulated in Table 5.9. The corresponding simulation result for $L = 18$ is tabulated in Table 5.4. Despite a significant increase in the number of rays representing a mode, there is no significant difference in the simulated bending losses (from 0.0776 to

m	Number of Rays	Total Power	Number of Rays lost	Power loss	Ratio
1	900	1	0	0	0
2	1800	1.782	0	0	0
3	2700	2.380	0	0	0
4	3600	2.815	0	0	0
5	4500	3.106	0	0	0
6	5400	3.269	0	0	0
7	6300	3.325	0	0	0
8	7200	3.289	0	0	0
9	8100	3.177	0	0	0
10	9000	3.007	0	0	0
11	9900	2.791	1106	0.055	0.020
12	10800	2.547	4140	0.165	0.065
13	11700	2.284	8083	0.273	0.119
14	12600	2.013	13770	0.369	0.183
15	13500	1.753	20436	0.432	0.247
16	14400	1.506	27693	0.485	0.322
17	15300	1.255	36890	0.509	0.405
18	16200	1.051	47328	0.524	0.499
19	17100	0.995	64814	0.625	0.628
		43.346		3.434	0.079

Table 5.9 Effects on simulation result for $\varphi = 30$ compared to Table 5.4 for $\varphi = 18$

0.0793). Using method 2, the number of combinations of i and j (see eqn. (3.26)) for a principal mode number was changed to $(4m-1)$ instead of m . This can be accomplished by changing the minimum value of i or j to 0.25 with increments of 0.25 instead of 1. A value of 18 was used for the variable L . This method increases the number of rings in both the r and k space. For the same case in method 1, the bending loss as shown in Table 5.10 was changed to 0.0782, another insignificant difference. Method 3 which combines the above two methods resulted in a bending loss of 0.0783, Table 5.11. All three methods of increasing the number of rays did not result in a significant difference in bending loss. Furthermore, the ratio of power loss for each individual principal mode number is relatively constant despite the increase in number of rays. The number of rays that leave within the first period of oscillation increases linearly with the increase in the number of rays representing a mode. This can be justified by the fact that the rays are selected at equal spacings from the r and k space.

The step size used in the simulation was 0.1 which is roughly $1/60$ the period of the ray. A reduced step size of 0.01 was investigated and that changed the bending loss to 0.0795.

5.4.2 Possible existence of a doping barrier

The possibility that a barrier exists between the core and cladding was investigated. This barrier used to be common in fibers fabricated by the modified chemical vapour deposition method. The existence of this barrier would alter the simulation results significantly as rays that are refracted out of the core will now encounter a region of lower refractive index that can be viewed as a

m	Number of Rays	Total Power	Number of Rays lost	Power loss	Ratio
1	972	1	0	0	0
2	2268	1.782	0	0	0
3	3564	2.380	0	0	0
4	4860	2.815	0	0	0
5	6156	3.106	0	0	0
6	7452	3.269	0	0	0
7	8748	3.325	0	0	0
8	10044	3.284	0	0	0
9	11340	3.177	0	0	0
10	12636	3.007	0	0	0
11	13932	2.791	1436	0.051	0.018
12	15228	2.547	5668	0.160	0.063
13	16524	2.284	11019	0.266	0.116
14	17820	2.013	19522	0.366	0.182
15	19116	1.753	27978	0.425	0.243
16	20412	1.506	38690	0.477	0.317
17	21708	1.255	52311	0.510	0.406
18	23004	1.051	64890	0.517	0.492
19	24300	0.995	92504	0.619	0.622
		43.346		3.391	0.078

Table 5.10 Effects on simulation results for $(4m-1)$ combinations compared to Table 5.4 for m combinations

m	Number of Rays	Total Power	Number of Rays lost	Power loss	Ratio
1	2700	1	0	0	0
2	6300	1.782	0	0	0
3	9900	2.380	0	0	0
4	13500	2.815	0	0	0
5	17100	3.106	0	0	0
6	20700	3.269	0	0	0
7	24300	3.325	0	0	0
8	27900	3.289	0	0	0
9	31500	3.177	0	0	0
10	35100	3.007	0	0	0
11	38700	2.791	3866	0.049	0.017
12	42300	2.547	15700	0.158	0.062
13	45900	2.284	31308	0.270	0.118
14	49500	2.013	54381	0.365	0.181
15	53100	1.753	78607	0.424	0.242
16	56700	1.506	108982	0.481	0.319
17	60300	1.255	144273	0.504	0.401
18	63900	1.051	184880	0.520	0.495
19	67500	0.995	258070	0.624	0.627
		43.346		3.395	0.078

Table 5.11 Effects on simulation results for $(4m-1)$ combinations and $\varphi = 30$ compared to Table 5.4 for m combinations and $\varphi = 18$

potential barrier that a ray must now overcome to enter the cladding. A two inch length of fiber was illuminated with white light and the throughput was observed under a microscope. Since a short piece was used, the entire cross-section of the fiber was illuminated. If a barrier exists, a dark ring between the core and cladding will be present due to the lower refractive index [40]. However no such ring was observed.

5.4.3. Uncertainty of fiber parameters

A factor that may contribute to the discrepancy is the uncertainty of the parameters of the fiber. Recall from Chapter 2, that a ray exhibits an offset from its equilibrium position

$$\Delta y = \left[\frac{k_{oz} c}{n_1 \omega Q} \right]^2 \frac{1}{R} \quad (2.46)$$

Using the fact that $k_{oz} \approx n_1 k_o$, the above equation can be reduced to

$$\Delta y \approx \frac{a^2 [(N.A.)^2 + n_2^2]}{(N.A.)^2 R} \quad (5.3)$$

The offset value is dependent on two fiber parameters (n_2 is constant for a specific wavelength as it is made of pure silica). Only the effects due to the variation of the numerical aperture on the simulation results was studied. From the data sheets (see Appendix E), the N.A. of the fiber has an error of ± 0.015 from its ideal 0.2 value. Consider the case of $R = 2125 \mu\text{m}$ and $n_2 = 1.453$ at $0.825 \mu\text{m}$, the offset value has a span of $4.71 \mu\text{m}$ from $13.725 \mu\text{m}$ and $18.435 \mu\text{m}$. A span of such magnitude which is roughly 19% of the radius of the core, has a significant impact on the simulation results. The effect of the

numerical aperture on the simulation results for both extremes of R are tabulated in Table 5.12 for all 5 cases. However, for all cases the experimental values do not fall within the uncertainty of the simulation results.

Comparison	R	Experimental	Theoretical		
Figure	(mm)		0.200	0.215	0.185
5.5	2.125	0.500	0.905	0.784	0.972
	10.125	0.0240	0.0776	0.0537	0.0932
5.10	2.125	0.427	0.904	0.777	0.972
	10.125	0.00112	0.0476	0.0339	0.0699
5.15	2.125	0.504	0.908	0.773	0.973
	10.125	0.0981	0.0981	0.0522	0.118
5.20	2.125	0.374	0.905	0.756	0.974
	10.125	0.00130	0.0462	0.0247	0.0602
5.25	2.125	0.675	0.911	0.803	0.970
	10.125	0.0591	0.138	0.0987	0.151

Table 5.12 Comparison of experimental and theoretical results with numerical apertures of 0.2, 0.215 and 0.185

5.4.4 Stress-optical effect

Another factor that may contribute to the discrepancy is the stress-optical effect in a bent fiber. It has been reported [41]-[43] that the stress in a bent fiber will modify its refractive index which in turn alters the transmission characteristics. Consider the bent fiber as shown in Fig. 5.38. The change in refractive index can be

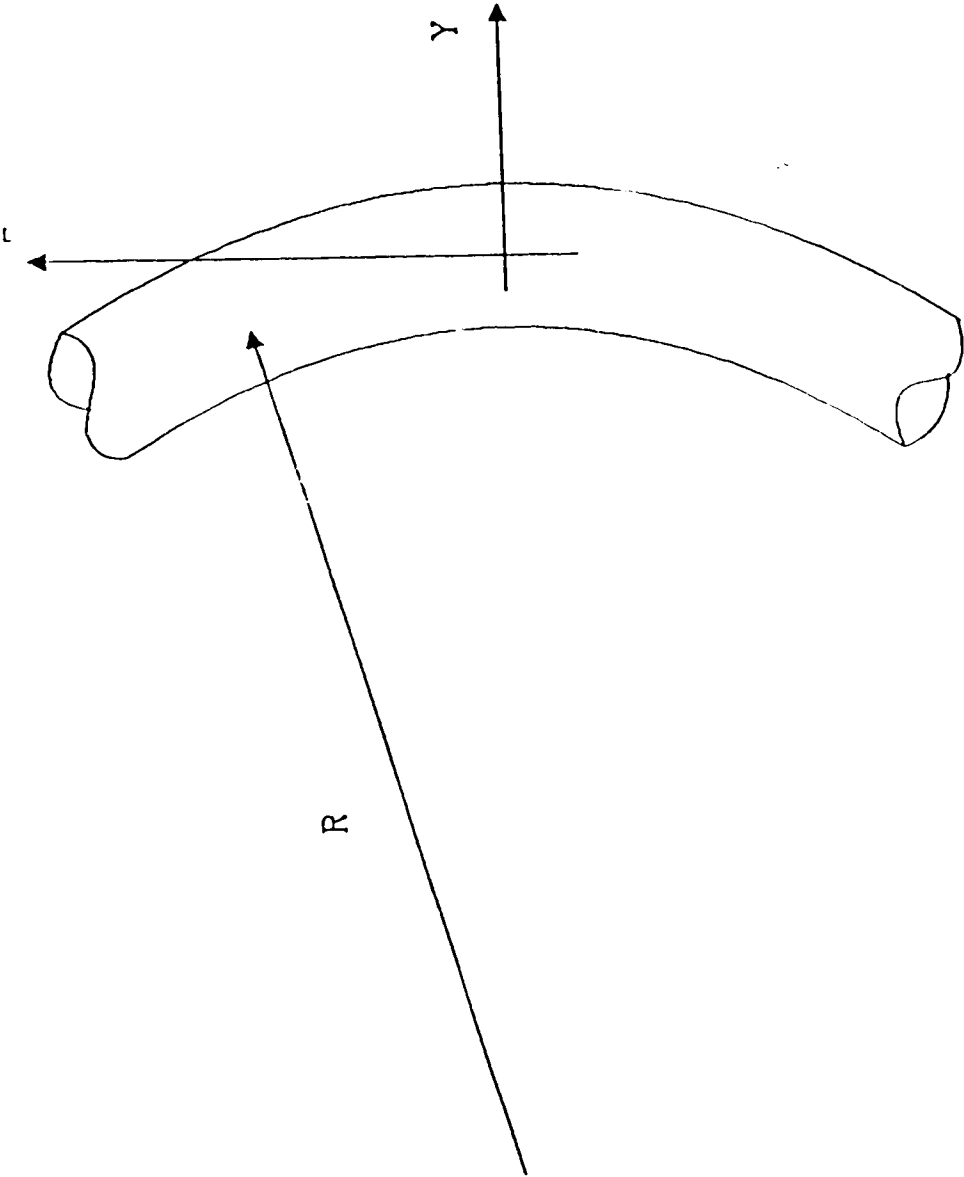


Fig. 5.38 Analysis of strain in a bent optical fiber

evaluated from the strain, ϵ , using the strain-optical coefficients, p_{ij} [43]

$$\begin{bmatrix} \Delta n_x \\ \Delta n_y \\ \Delta n_z \end{bmatrix} = -\frac{n^3}{2} \begin{bmatrix} p_{xx} & p_{xy} & p_{xz} \\ p_{yx} & p_{yy} & p_{yz} \\ p_{zx} & p_{zy} & p_{zz} \end{bmatrix} \begin{bmatrix} \epsilon_x \\ \epsilon_y \\ \epsilon_z \end{bmatrix} \quad (5.4)$$

where $p_{xx} = p_{yy} = p_{zz} = \alpha$ and the cross terms are identical, β [44]. The strain is related to the stress σ by [45]

$$\begin{bmatrix} \epsilon_x \\ \epsilon_y \\ \epsilon_z \end{bmatrix} = \frac{1}{E} \begin{bmatrix} 1 & -\nu & -\nu \\ -\nu & 1 & -\nu \\ -\nu & -\nu & 1 \end{bmatrix} \begin{bmatrix} \sigma_x \\ \sigma_y \\ \sigma_z \end{bmatrix} \quad (5.5)$$

where E is Young's Modulus and ν is Poisson's ratio (not to be confused with the azimuthal mode number). For a simple estimate on the effects of stress on the change of refractive index, the stress in the x -direction is ignored ($\sigma_x = 0$). The stress in the z and y direction are [43]

$$\sigma_z = E \frac{y}{R} \quad (5.6)$$

$$\sigma_y = E \frac{(y^2 - r^2)}{2R^2} \quad (5.7)$$

It is obvious that the dominant of the two stresses is in the z -direction since $R \gg y$. Therefore, the effect of the stress in the y -direction can be neglected. Substituting eqns. (5.5) and (5.6) into eqn. (5.4)

$$\begin{bmatrix} \Delta n_x \\ \Delta n_y \\ \Delta n_z \end{bmatrix} = -\frac{n^3 y}{2R} \begin{bmatrix} -\alpha\nu + \beta(1-\nu) \\ -\alpha\nu + \beta(1-\nu) \\ \alpha - 2\beta\nu \end{bmatrix}. \quad (5.8)$$

Eqn. (5.8) relates the change of refractive index to a dominant stress in the z-direction. Therefore, the effective refractive index as seen by a transverse electromagnetic wave travelling predominantly in the z-direction is

$$n_{\text{eff}}(r) = n(r) - \frac{n^3 y}{2R} \left[-\alpha\nu + \beta(1-\nu) \right]. \quad (5.9)$$

The identical result is quoted in Ref. [46].

As shown in Appendix C, the introduction of the stress to the equation does not change the ray propagation equations in a bent fiber. It defines an effective R

$$R_{\text{eff}} = \frac{2R}{2 - n_1^2 \theta} \quad (5.10)$$

where

$$\theta = -\alpha\nu + \beta(1-\nu). \quad (5.11)$$

For fused silica, the values of α , β and ν are [44]

$$\alpha = 0.121$$

$$\beta = 0.270$$

$$\nu = 0.170.$$

With these values, $R_{\text{eff}} = 1.28R$ and $1.277R$ for $\lambda_0 = 0.825 \mu\text{m}$ and $1.3 \mu\text{m}$ respectively. Figs. 5.39 - 5.43 depict the new simulation results with R_{eff} for all 5 cases. Without doubt, the introduction of R_{eff} reduced

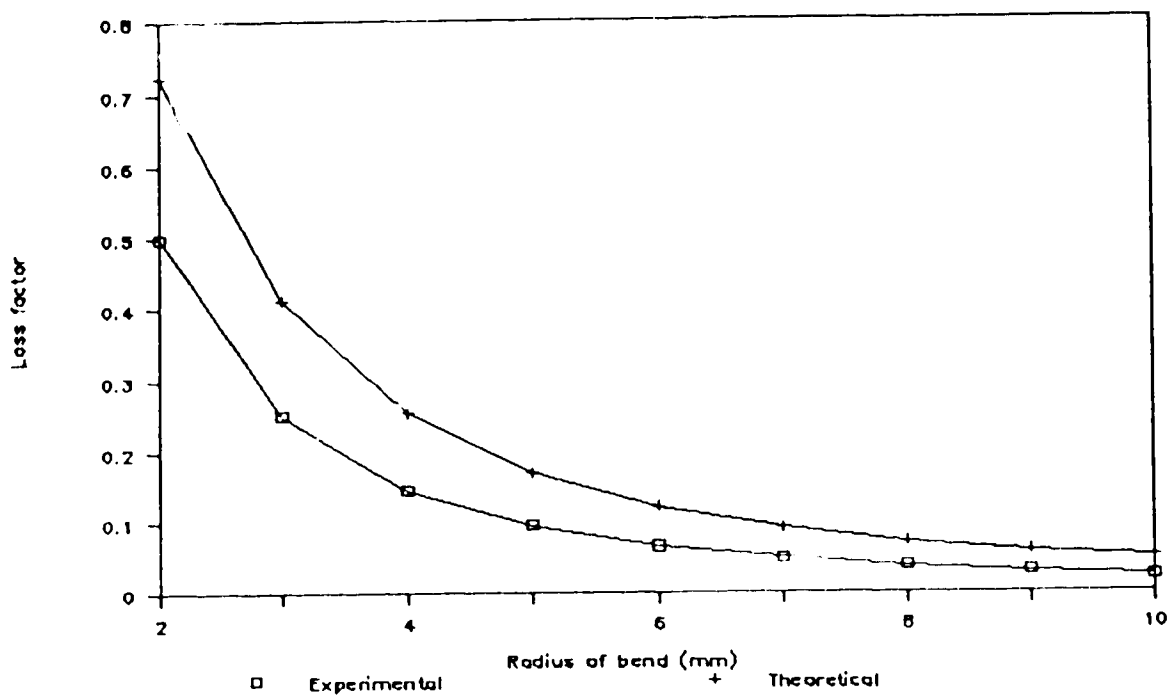


Fig. 5.39 Experimental and revised theoretical bending losses for MPD shown in Fig. 5.4

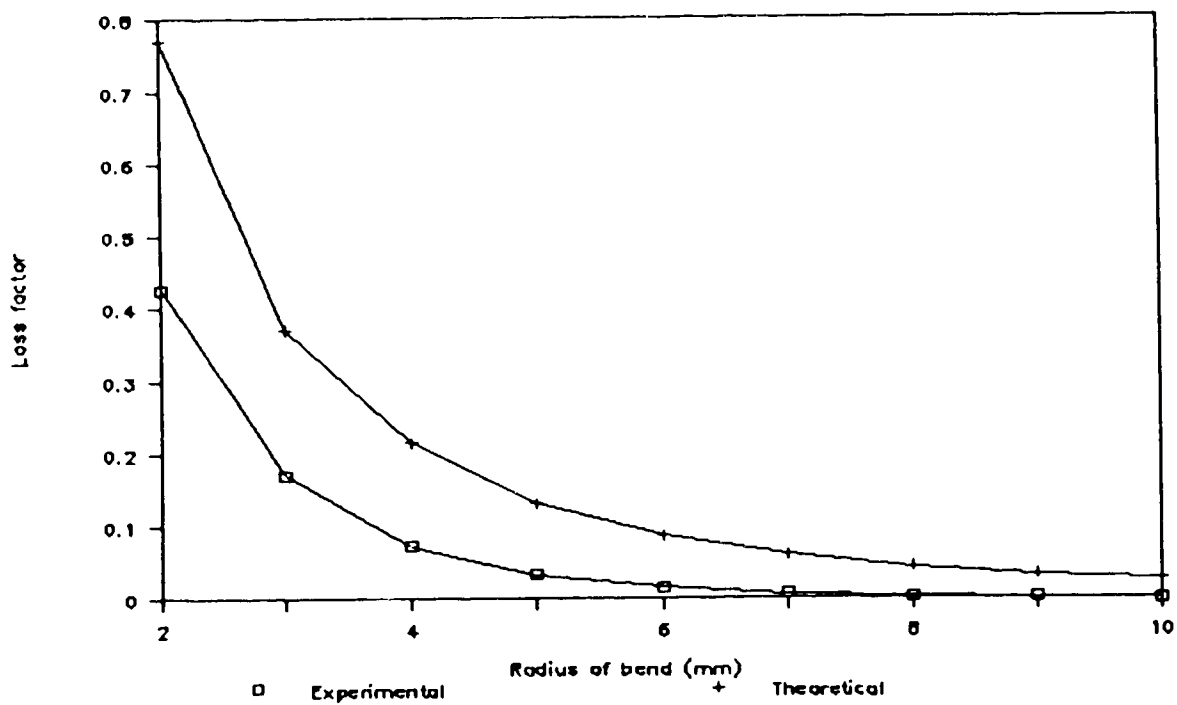


Fig. 5.40 Experimental and revised theoretical bending losses for MPD shown in Fig. 5.9

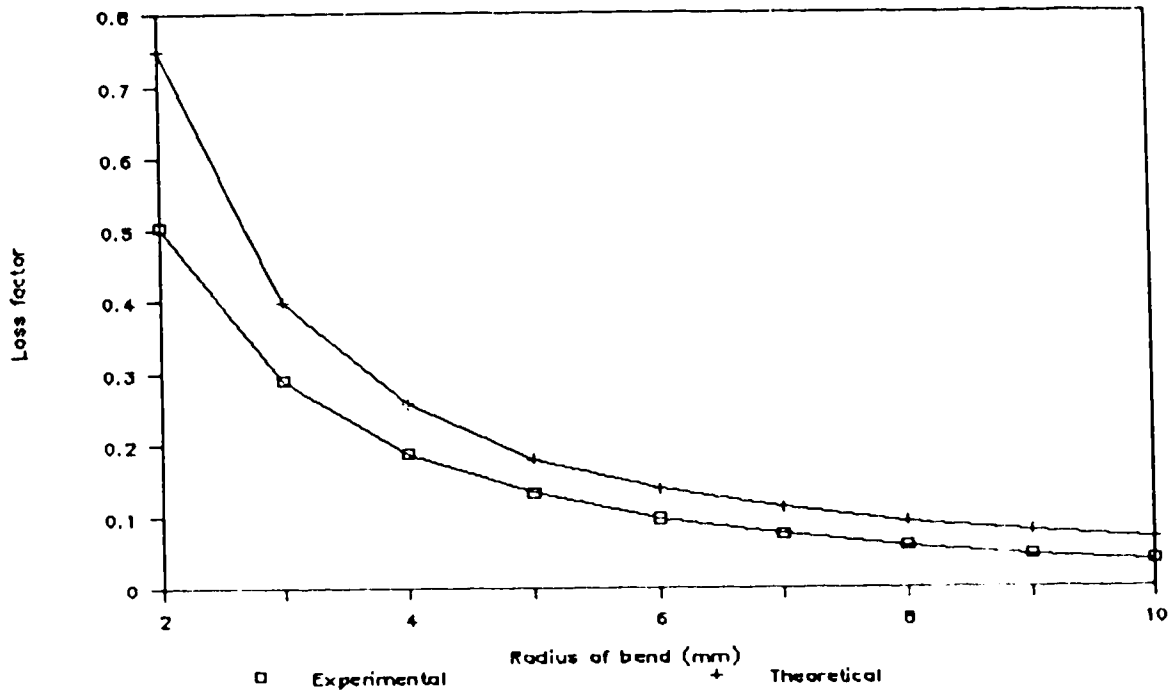


Fig. 5.41 Experimental and revised theoretical bending losses for MPD shown in Fig. 5.14

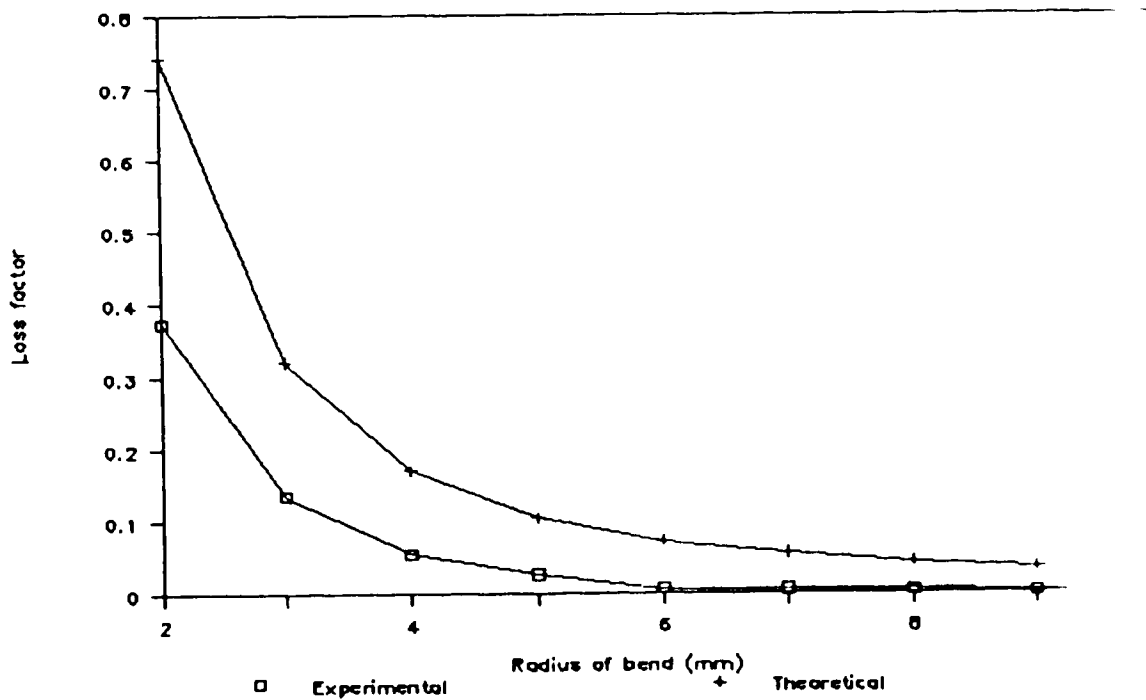


Fig. 5.42 Experimental and revised theoretical bending loss for MPD shown in Fig. 5.19

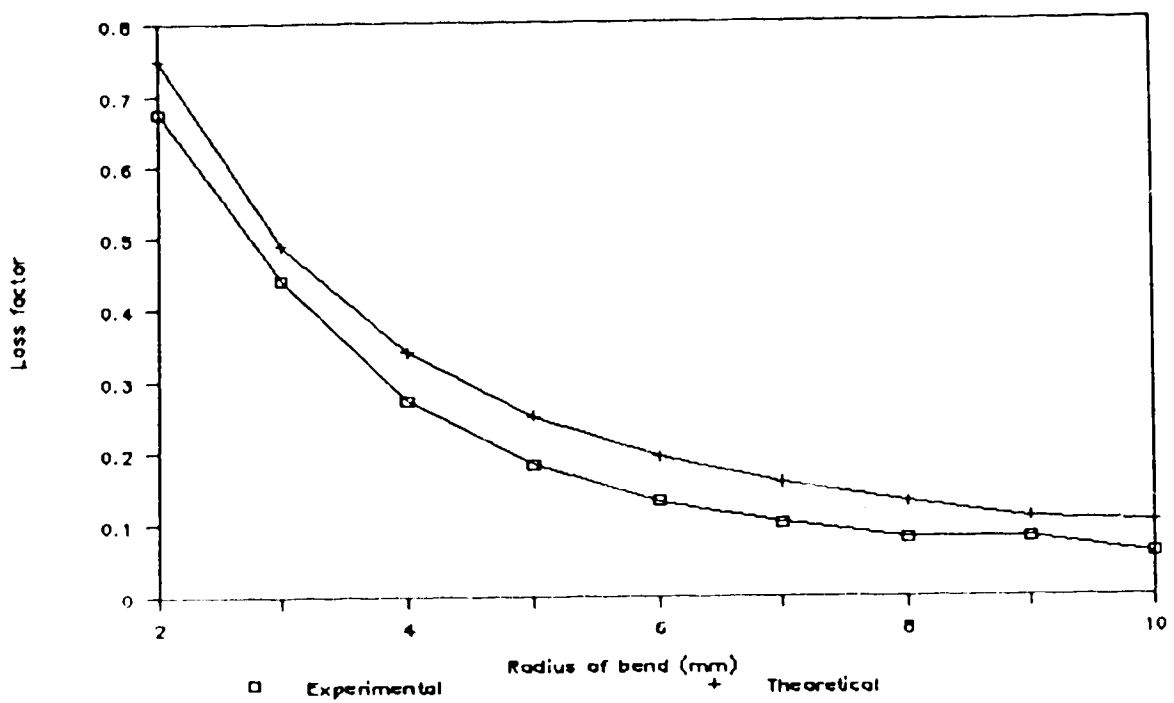


Fig. 5.43 Experimental and revised theoretical bending losses for MPD shown in Fig. 5.24

the simulation results significantly and are more comparable to the experimental results than before.

5.4.5 Measurement of the modal power distribution

There is one more factor worth discussing that could explain any remaining discrepancy and that is error in measuring the modal power distribution (MPD). Two things can be noted from Figs. 5.39 - 5.43. First, the sharper contrast in comparison for cases where the mandrel wrap was applied and secondly, the increasing difference in bending losses for increasing values of R in all 5 cases. With the mandrel wrap applied, the MPD at higher principal mode number region was found to be reduced which resulted in a drop in simulated power loss. However, this reduction was not significant enough to make the results more comparable. For increasing values of R where the discrepancies increase in all 5 cases, recall that the power loss comes from modes in the higher principal mode number region. This could only mean that errors are present in the MPD, especially in the higher principal mode number region. The errors are not that significant for smaller R because in this situation the bending losses are dominated by losses in the lower principal mode number region which has more power than the higher principal mode number region.

The source of error in the higher principal mode region may be due to the fact that curve-fitting was performed prior to performing the inverse Abel transform. Some critical information may have been lost in the process. However, at the present time, the curve-fitting procedure seems to be the best alternative.

Another source of error may be due to the uncertainty in the

magnification factor of the lens. Underestimating the nominal magnification of 40 would result in too much power being assigned to the higher order modes when eqn. (3.20) is used, and consequently the loss would be overestimated. By using a gaussian approximation for the near-field pattern, each 1% error in the magnification has been estimated to result in a 5% error in the loss. For example, if the magnification is 41 instead of 40, the loss will be 12.5% too large. Combined with the 15% experimental uncertainty in the measurement of loss (see Section 5.2), the simulation and experiments are actually in reasonable agreement.

Chapter 6

Prototypes

6.1 Introduction

With the introduction of R_{eff} , the simulation results as shown in the previous chapter are in better agreement with the experimental results. Accuracy is not the key issue as the whole simulation model is an approximation. The simulation program and the other software developed to observe the radiating patterns are simple tools to reasonably model the radiation of light from a bent fiber. The design of the prototypes would have involved much more guesswork without them.

This chapter deals with the design, implementation and testing of variable tapping device taking into consideration the results obtained theoretically and experimentally. The chapter opens by discussing the design considerations taken into account in the development of the prototype. In sections 6.3 and 6.4, the designs of the prototypes are presented together with a summary of their performances.

6.2 Design considerations

As shown in the previous chapter, the bending losses depend on the modal power distribution (MPD) of the fiber. Therefore, it is essentially impossible to design a prototype that will provide a guaranteed range of tapping ratios as the MPD varies from system to system. The goal is to implement a tapping device with the adjustable but not guaranteed tapping ratio feature.

The insertion loss of the tap is defined as

$$10 \log \frac{P_{w_0}}{P_w} \quad (6.1)$$

where

P_{w_0} - throughput power without the tap

P_w - throughput power with the tap.

The tapping efficiency is defined as

$$\eta = \frac{P_t}{P_{w_0} - P_w} \quad (6.2)$$

where P_t is the power detected by the detector chip. The main factor that affects the tapping efficiency is the location of the detector. From the radiating plots shown in the previous chapter, it is imperative that the detector chip be placed as close as possible to the bend before the radiating beam diverges significantly. Considering the size of the commercially available detector chips and the width of the radiating beam, it would be impossible to obtain a 100% tapping efficiency. The best alternative is to place the detector at the position of maximum radiated intensity.

The two variables that affect the bending losses are the length and the radius of the bend (hereafter referred to as R). To vary both simultaneously would not be a practical situation as it would be difficult to implement such a device with this feature. Furthermore, minimizing the number of variables would lead to simpler designs and fewer moving parts. The simpler alternative is to keep one of the two variables fixed while the other is varied. Consider the first case of fixing R and varying the length of the bend. Recall that propagation of a ray in the core is periodic and if a ray does not leave the core

within the first period, it will remain in the bend throughout. Since a ray repeats itself at approximately every 1.2 mm (see Chapter 4), it is necessary to vary the length within this limit to obtain variable bending losses. This is rather impractical. Furthermore, with this method, it is essentially impossible to place the detector chip close to the bend without intrusion from the fiber as the most intense radiating beams are more or less parallel to the z axis (see Figs. 5.30 - 5.37). The other alternative is to keep the angle fixed while varying R . Taking into account the size of the detector chip, it was decided that the space provided by a 90° bend will be sufficient. A perfect tapping efficiency cannot be achieved as the wide radiating beam will not fall within the limits of the detector.

The remaining factor to be decided is the range of R . The range of R is fairly arbitrary. As was shown in the previous chapter, the bending losses vary for a specific R depending on the MPD. However, there are two factors to remember. It is important not to bend the fiber so tightly that stress cracking develops during the lifetime of the fiber. Furthermore, insertion losses within 10% are desired. With those factors in mind, it was decided that R (not including the radius of the fiber) should vary between 7 mm and 10 mm.

In designing the prototypes, the MPD shown in Fig. 5.4 was used. As mentioned before, the most intense radiation occurs at the start of the radiation range and it is independent of the MPD. Therefore, it is only logical to place the detector at a location that will capture all the initial radiated power for optimum tapping efficiency. Obviously, the location of optimum detection will vary for different R and that requires repositioning each time the radius is changed. The simulated

radiation patterns for $R = 7.125 - 10.125 \text{ mm}$ are shown in Figs. 6.1 - 6.4. The refractive index of 1.50 was assumed in the exterior. The positions of the detector were selected such that the z-position is the same for all 4 cases while optimizing the tapping efficiency. For all cases, the tapping efficiencies were averaged around 0.73 with the following positions:

Radius (mm)	Z (mm)	Y (mm)	η
7.125	6.5	7	0.77
8.125	6.5	8	0.74
9.125	6.5	9	0.72
10.125	6.5	10	0.70

Table 6.1 Positions and simulated tapping efficiencies for various radius of curvature

6.3 Prototype I

The basic operating principle behind this prototype is to bend the fiber around discs of different radii to vary the insertion loss. However, to avoid the repositioning of the detector each time a different disc is utilized, the discs are made with a fixed z-origin and varying y-origin for all discs, see Fig. 6.5. Hence, the starting points of the bend for different R relative to the detector are always fixed. The prototype is made from acrylic and is shown in Fig. 6.6. With the same experimental setup as in Fig. 5.29, the prototype was tested using the second of the two $0.825 \mu\text{m}$ laser source. The performance of the device is tabulated in Table 6.2. A wide range of insertion is obtainable from the prototype and the tapping efficiency

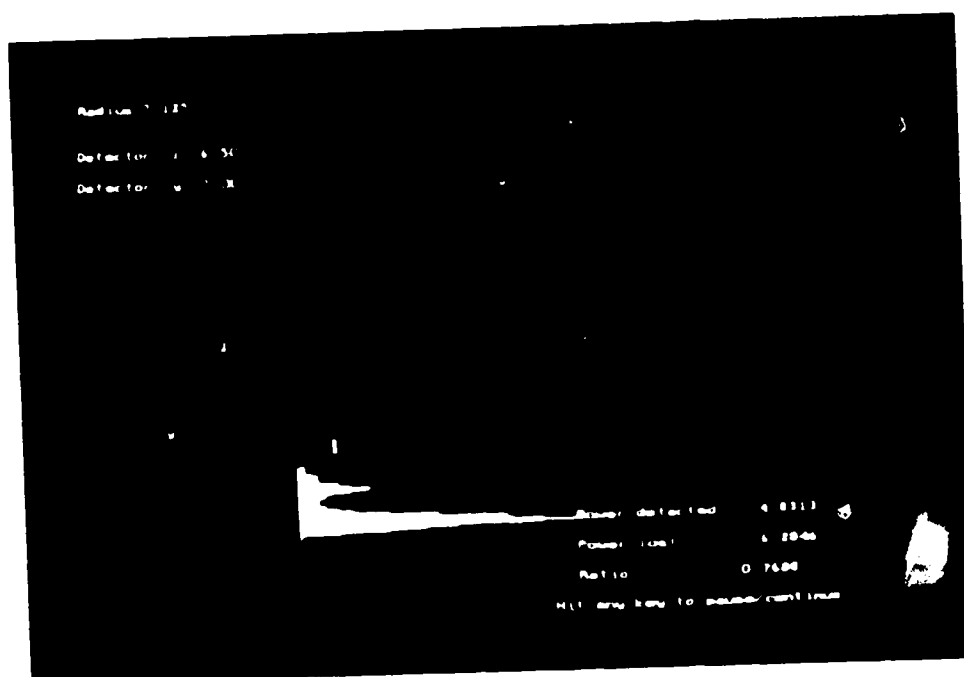


Fig. 6.1 Simulated radiation pattern for $R = 7.125$ mm with the detector at $z = 6.5$ mm and $y = 7$ mm



Fig. 6.2 Simulated radiation pattern for $R = 8.125$ mm with the detector at $z = 6.5$ mm and $y = 8$ mm

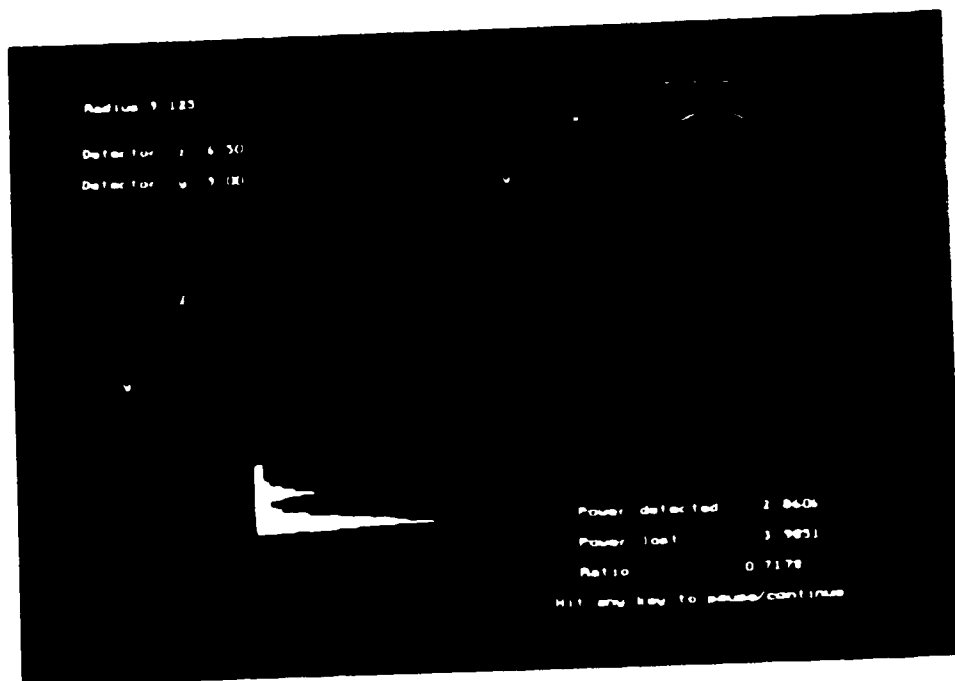


Fig. 6.3 Simulated radiation pattern for $R = 9.125$ mm with the detector at $z = 6.5$ mm and $y = 9$ mm

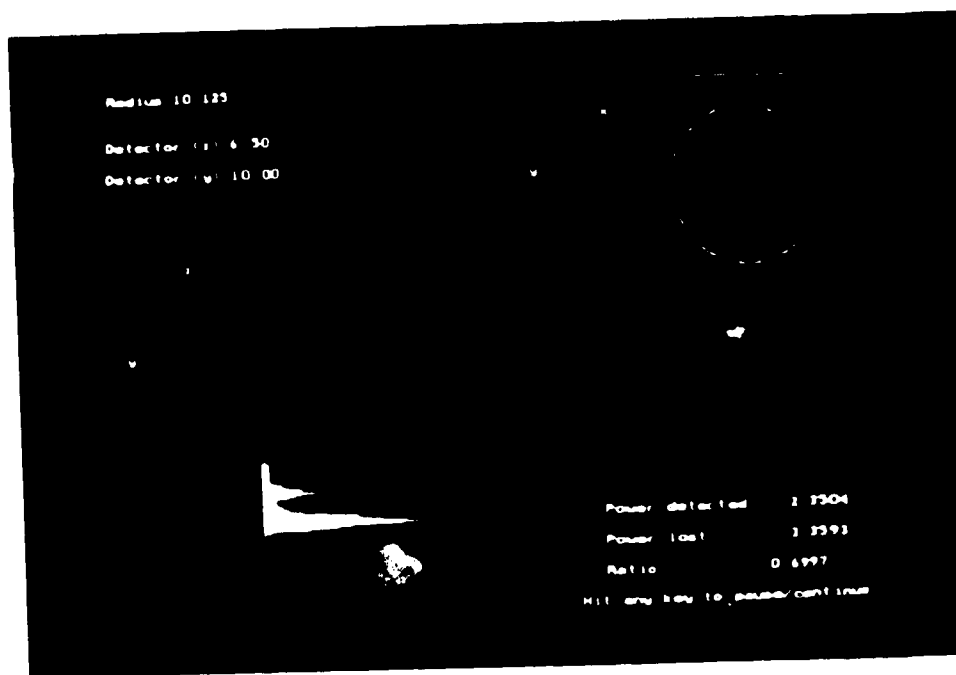


Fig. 6.4 Simulated radiation pattern for $R = 10.125$ mm with the detector at $z = 6.5$ mm and $y = 10$ mm

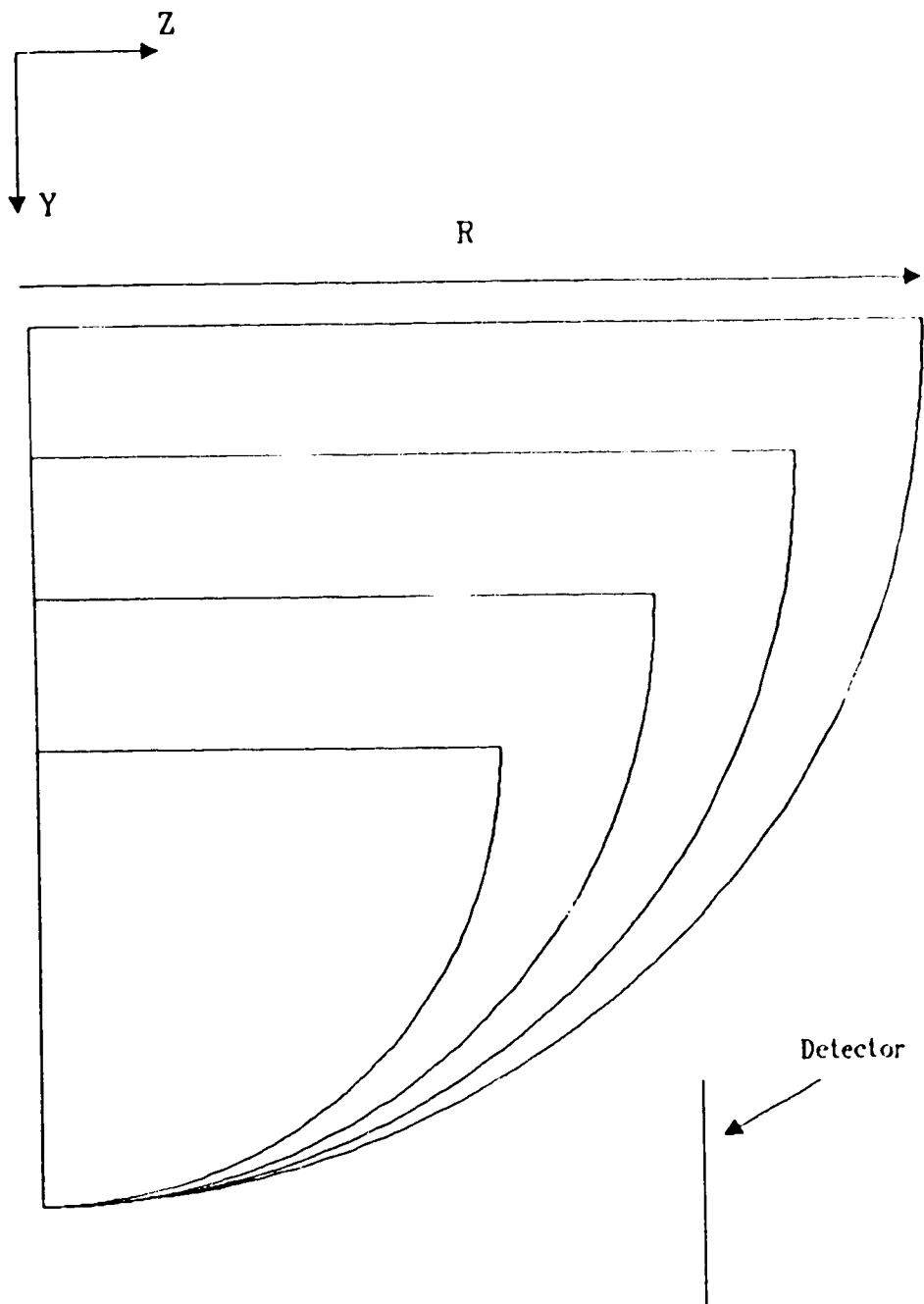


Fig. 6.5 Discs with different radius of curvature. They are constructed with a fixed z -origin and varying y -origin with respect to the detector

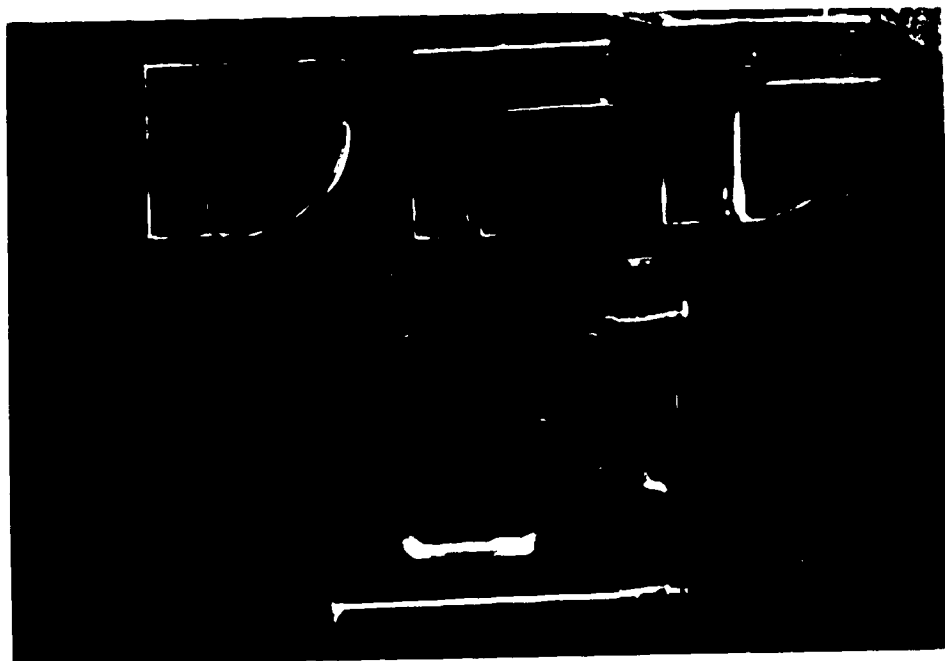


Fig. 6.6 Prototype I with the different discs magnified 1.8X

is fairly constant.

Disc radius (mm)	Insertion loss (dB)	Tapping efficiency
7	0.134	0.43
8	0.091	0.53
9	0.083	0.49
10	0.013	0.46

Table 6.2 Performance of prototype I

6.4 Prototype II

For the second prototype the inconvenience of changing discs is eliminated. Both ends of the fiber are fixed and it is bent around a disc with a radius of 7 mm. The insertion loss is varied by moving the upper portion of the fiber holder up or down, see Fig. 6.7. The detector is positioned at the same location as the previous prototype. It is expected that the insertion loss will increase as more fiber is fed into a fixed amount of space and bend the fiber more. The predicted optimum position for the detector is not valid as the radius of curvature is no longer constant. The prototype is also made of acrylic and is shown in Fig. 6.8. The performance of the device is tabulated in Table 6.3.

Insertion loss (db)		Tapping efficiency
Minimum	0.129	0.325
Maximum	0.206	0.430

Table 6.3 Performance of prototype II

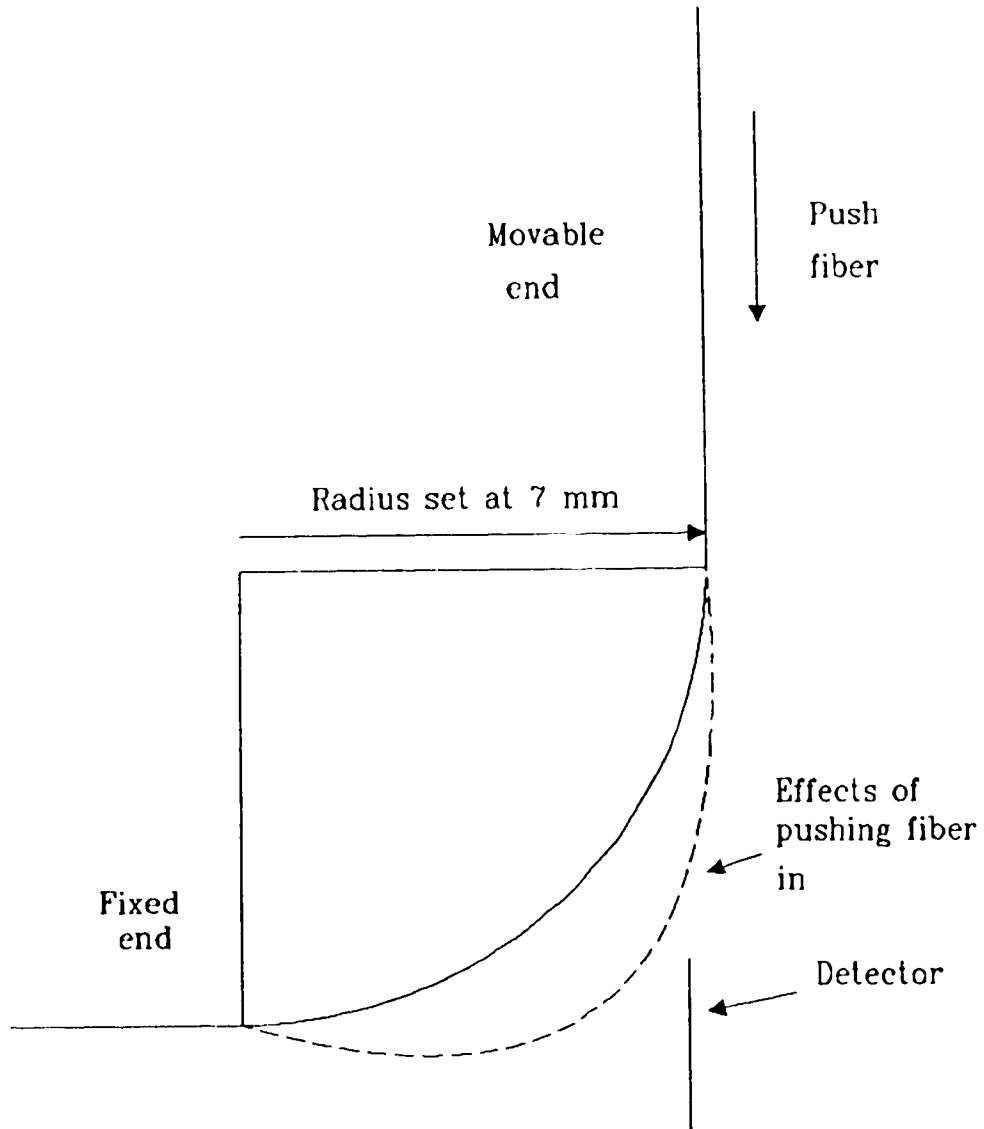


Fig. 6.7 Basic operating principal of prototype II

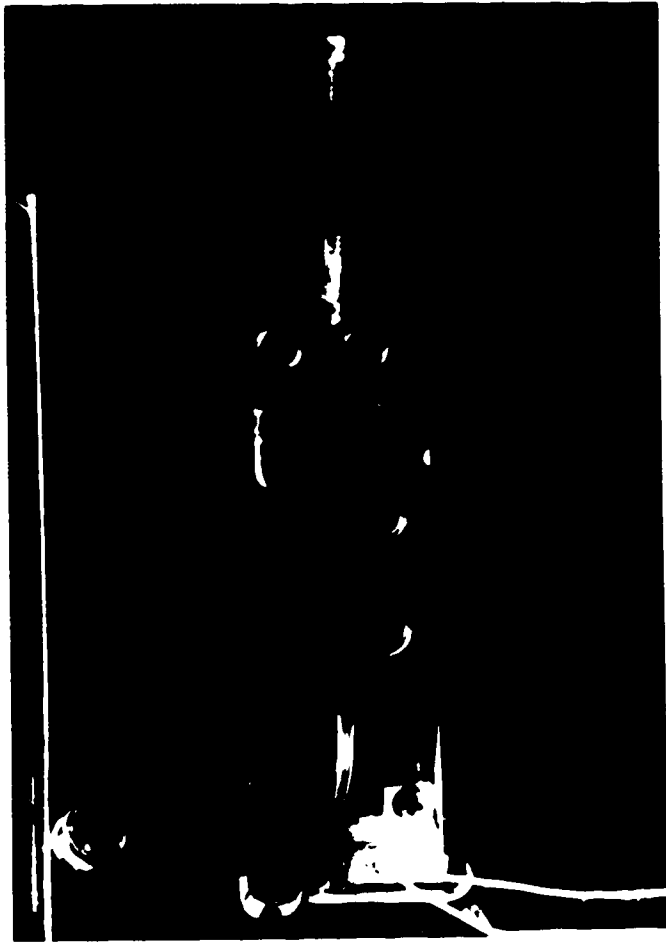


Fig. 6.8 Prototype II magnified 1.8X

The second prototype was also tested with a fiber with a $5 \mu\text{m}$ core radius which is single mode at $0.825 \mu\text{m}$. The performance is tabulated in Table 6.4.

Insertion loss (db)		Tapping efficiency
Minimum	0.0621	0.61
Maximum	0.7370	0.34

Table 6.4 Performance of prototype II with $0.825 \mu\text{m}$ single mode fiber

Without any doubt, non-intrusive tapping on single mode fibers is also possible. However, the performance of this prototype with single mode fiber cannot be explained as the theory has not been pursued.

Chapter 7

Summary

This thesis is concerned with the modelling and experimental verification of losses and radiation patterns of a bent multimode fiber taking into account the modal power distribution. With that model, two prototypes have been successfully implemented to non-intrusively tap optical power from a live fiber.

In previously published literature on bending losses in multimode fiber, the modal power distribution of the fiber was not taken into account. The general approach was to assume a lambertian source was used to excite the fiber. However, in practical situations, it was shown that not all modes are equally excited when the laser was the source. Taking into account the modal power distribution, the theoretical bending losses were still significantly different when compared to the experimental results.

Three major factors that may contribute to the discrepancies were discussed. It has been shown that the parameters of the fiber are important in the simulation results. A change in the numerical aperture affects the simulation results. Perhaps the most important factor of the three is the change in refractive index of the fiber caused by the induced strain when bending the fiber. This change in refractive index could very well explain the discrepancy that was mentioned by Ref. [12]. In previously published literature on theoretical bending losses, this effect was not taken into account [5]-[11]. The final factor is the modal power distribution. Since the bending losses for large radius of curvature are dominated by modes in

the higher principal region, the near-field pattern towards the core and cladding interface is very critical. A better method of obtaining the near-field pattern should be investigated, perhaps projecting it onto a vidicon of a measuring TV-system which digitizes the data [25].

The software to analyze the data generated from the simulation program provided some insight as to what sort of radiation pattern to expect for a given radius of curvature and modal power distribution. Although not describing the experimental situation exactly, it provided a reasonable tool to aid in the designing of the prototypes.

Two prototypes have been designed and tested. Non-intrusive optical fiber tapping is possible with multimode and single mode fiber. They both provide a wide range of low insertion losses. It must be noted that the following summary of their performances are not guaranteed for all systems as the bending losses depend on the modal power distribution. The summary was obtained under a particular test condition. The insertion loss of the first prototype has a range of 0.013 to 0.134 db with tapping efficiencies varying from 0.43 to 0.53. The second prototype has been tested to provide an insertion loss varying from 0.129 to 0.206 db with tapping efficiencies of 0.325 and 0.430 for multimode fiber system. For single mode fiber, the insertion loss varied from 0.0621 to 0.737 db with tapping efficiencies of 0.61 to 0.34. Both prototypes, other than being variable, are easy to install and remove without any damage or disruption to the system.

Some suggestions for future research work are :

1. explore other possibilities other than fluid to couple light present in the jacket into the exterior.

2. use inter-digitated detectors for their larger area and speed [47].
3. use better packaging with built-in circuitry and suppression of external light.
4. pursue theory for bending loss in single mode fiber using the propagating beam method.

REFERENCES

- [1] F. Gfeller, U. Bapst, "Optical-fibre tap with low insertion loss," *Electron. Lett.*, vol. 15 no. 15, pp. 448-450, July 1979.
- [2] T. Ozeki, B. Kawasaki, "Optical directional coupler using tapered sections in multimode fibres," *Appl. Phys. Lett.*, vol. 28, pp. 528-529, 1976.
- [3] C. Miller, "Connectorless taps for coated single mode or multimode optical fibres," *European Conference on Optical Communications*, 21-24 September 1982, Cannes, France.
- [4] E. Harstead, S. Elby, P. Prucnal, "Low-loss high-impedance integrated fiber-optic tap," *Optical Fiber Communications Conference* 25-28 January 1988, New Orleans, Louisiana.
- [5] C. Winkler, J. Love, A. Ghatak, "Loss calculations in bent multimode optical waveguides," *Opt. Quant. Elect.* 11, pp. 173-183, 1979.
- [6] J. Arnaud, M. Rousseau, "Ray theory of randomly bent multimode optical fibers," *Opt. Lett.*, vol. 3 no.2, pp.63-65, August 1978.
- [7] D. Gloge, "Bending loss in multimode fibers with graded and ungraded core index," *Appl. Opt.*, vol. 11 no. 11, pp. 2506-2513, November 1972.
- [8] M. Artiglia, G. Coppa, P. Di Vita, H. Kalinowski, M. Potenza, "Bending loss characterization in single-mode fibers," 13th. *European Conference on Optical Fiber Communications*, Helsinki, pp. 437-443, 1987.
- [9] D. Marcuse, "Curvature loss formula for optical fibers," *J. Opt. Soc. Am.*, vol. 66 no. 3, pp. 216-220, March 1976.
- [10] K. Petermann, R. Kühne, "Upper and lower limits for the microbending loss in arbitrary single-mode fibers," *J. Lightwave Technol.*, vol. LT-4 no. 1, pp. 2-7, January 1986.

- [11] P. Geittner, H. Lydtin, F. Weling, D. Wiechert, "Bend loss characteristics of single mode fibers," 13th. European Conference on Optical Fiber Communications, Helsinki, pp. 97-108, 1987.
- [12] O. Wright, D. Largeau, "Fibre-optic differential pressure sensor," J. Phys. E. (GB), vol. 20 no. 1, pp. 46-51, 1987.
- [13] D. Marcuse, Light Transmission Optics. New York : Van Nostrand Reinhold Company Inc., 1982.
- [14] R. Liboff, Introductory Quantum Mechanics. California : Holden-Day Inc., 1980.
- [15] A. Cherin, An Introduction to Optical Fibers. New York : McGraw-Hill Book Company, 1983.
- [16] M. Barnoski, Fundamentals of Optical Fiber Communications. New York : Academic Press Inc., 1981.
- [17] Dr. J.N. McMullin, University of Alberta, Private Communication, 1988.
- [18] J. Arnaud, "Hamilton's theory of beam mode propagation," Progress in Optics XI Editor E. Wolf, North Holland 1973.
- [19] J. Gowar, Optical Communication Systems. New Jersey : Prentice-Hall International Inc., 1984.
- [20] J. Jackson, Classical Electrodynamics. New York : John Wiley & Sons Inc., 1975.
- [21] R. Olshansky, S. Oaks, "Differential mode attenuation measurement in graded-index fibers," Appl. Opt., vol.17 no.11, pp. 1830-1835, June 1978.
- [22] L. Jeunhomme, J. Pocholle, "Selective mode excitation of graded index optical fibers," Appl. Opt., vol.17 no 3, pp. 463-468, February 1978.
- [23] A. Agarwal, G. Evers, U. Unrau, "New and simple method for selective mode group excitation in graded-index optical fibers," Electron. Lett., vol.19 no. 17, pp. 694-695, August 1983.

- [24] D. Peckham, C. Lovelace, "Multimode optical fiber splice loss : Relating system and laboratory measurements," J. Lightwave Technol., vol.LT-5 no.11, pp. 1630-1635, November 1987.
- [25] A. Agarwal, U. Unrau, "Comparative study of methods to produce stationary mode power distribution for optical fiber measurements", J. Opt. Commun., pp. 126-133, March 1983.
- [26] D. Gloge, Bell System. Tech. J. 55, pp. 1767 ,1972.
- [27] Y. Daido, E. Miyauchi, T. Iwarma, T. Otsuka, "Determination of modal power distribution in graded-index optical waveguides from near-field patterns and its application to differential mode attenuation measurement," Appl. Opt., vol. 18 no. 13, pp. 2207-2213, July 1979.
- [28] O. Leminger, G. Grau, "Nearfield-intensity and modal power distribution in multimode graded-index fibres," Electron. Lett., vol.16, pp. 678-679, 1980.
- [29] K. Kitayama, M. Tatedo, S. Seikai, N. Uchida, "Determination of mode power distribution in a parabolic-index optical fiber : theory and application," IEEE J. Quantum Electron., vol. QE-15 no. 10, pp. 1161-1165, October 1979.
- [30] D. Rittich, "Practicability of determining the modal power distribution by measured near and far fields," J. Lightwave Technol., vol. LT-3 no.3, pp. 652-661, June 1985.
- [31] G. Grau, O. Leminger, "Relations between near-field and far-field intensities, radiance, and modal power distribution of multimode graded-index fibers," Appl. Opt., vol.20 no. 3, pp. 457-459, pp. 457-459, February 1981.
- [32] S. Piazzolla, G. De Marchis, "Analytical relations between modal power distribution and near-field intensity in graded-index fibres," Electron. Lett., vol. 15 no. 22, pp. 721-722, 1979.
- [33] D. Gloge, E. Marcatili, "Multimode theory of graded-core fiber," Bell Syst. Tech. J., 52, pp. 1563-1578, 1973.

- [34] A. Mickelson, M. Eriksrud, "Mode-continuum in optical fiber," Opt. Lett., vol. 7 no. 11, pp. 572-574, November 1982.
- [35] D. Paguette, W. Wiese, "Data processing system for the automatic transformation of observed plasma intensities into their radial distribution," Appl. Opt., vol. 3, pp. 291-296, 1964.
- [36] Melles Griot, Optics Guide 3, pp. 310-312.
- [37] A. Snyder, J. Love, "Reflection at a curved dielectric interface - Electromagnetic tunneling," IEEE Trans. MTT-23, pp. 134-141, January 1975.
- [38] Mr. Scott Cartington and Kirk Weinstein, Optics Engineers at Corning Glass Works, Private Communication, 1988.
- [39] Ithaco Dynatrac Model 397EO Operating Manual
- [40] D. Marcuse, Principles of Optical Fiber Measurements. New York : Academic Press, Inc., 1981.
- [41] H.C. Lefevre, "Single-mode fibre fractional wave devices and polarisation controllers," Electron. Lett., vol. 16 no. 20, pp. 778-780, 1980.
- [42] Y. Namihiro, M. Kudo, Y. Mushiake, "Effect of mechanical stress on the transmission characteristics of optical fiber," Electron. and Communications in Japan, vol. 60-C no. 7, pp. 107-115, 1977.
- [43] R. Ulrich, S. Rashleigh, W. Eickhoff, "Bending-induced birefringence in single-mode fibers," Opt. Lett., vol. 5 no. 6, pp. 273-275, June 1980.
- [44] D.A. Pinnow, "Elasto-optic Materials," in Handbook of Lasers, R.J. Presley, Ed. Cleveland, OH: CRC, 1971.
- [45] C.W. Scherer, Relaxation in Glass and Composites. New York : John Wiley & Sons, Inc., 1986.
- [46] H. Taylor, "Bending effects in optical fibers," J. Lightwave Technol., vol. LT-2 no.5, pp. 617-628, 1984.
- [47] Dr. I. MacDonald, Alberta Telecommunications Research Centre, Private Communication, 1988.

Appendix A

Ray Propagation in a Bent Parabolic Graded-Index Fiber

The formulas for the propagation of a ray in a bent graded-index fiber as summarized in Chapter 2 are derived in this appendix. The derivation is based on the local rotating coordinate system as shown in Fig. 2.7. Recall from Section 2.3 the two general ray equations:

$$\frac{d\vec{r}}{dt} = \frac{c^2 \vec{k}}{n^2(\vec{r}) \omega} \quad (\text{A.1})$$

$$\frac{d\vec{k}}{dt} = \frac{\omega}{2n^2(\vec{r})} \nabla_{\vec{r}} n^2(\vec{r}). \quad (\text{A.2})$$

The position vector \vec{r} is now defined as

$$\vec{r} = x \hat{x} + (R+y) \hat{r} \quad (\text{A.3})$$

and using the following transformation

$$\hat{r} = \theta \hat{\theta} \quad (\text{A.4})$$

$$\hat{x} = \hat{y} \quad (\text{A.5})$$

$$\hat{\theta} = \hat{z} \quad (\text{A.6})$$

on eqn. (A.1)

$$\dot{x} = \frac{c^2 k_x}{n^2(\vec{r}) \omega} \quad (\text{A.7})$$

$$\dot{y} = \frac{c^2 k_y}{n^2(\vec{r}) \omega} \quad (\text{A.8})$$

$$(R+y)\dot{\theta} = \frac{c^2 k_z}{n^2(\vec{r}) \omega} \quad (\text{A.9})$$

where $\dot{x} = \frac{dx}{dt}$ and so on.

The wave vector \vec{k}

$$\vec{k} = k_x \hat{x} + k_y \hat{y} + k_z \hat{z} \quad (\text{A.10})$$

and using the transformations

$$\hat{y} = \theta \hat{\theta} \quad (\text{A.11})$$

$$\hat{\theta} = -\theta \hat{y} \quad (\text{A.12})$$

on eqn (A.2)

$$k_x = -\frac{2\Delta\omega n_1^2}{n^2(\vec{r}) a^2} x \quad (\text{A.13})$$

$$k_y = k_z \theta = -\frac{2\Delta\omega n_1^2}{n^2(\vec{r}) a^2} y \quad (\text{A.14})$$

$$k_z + k_y \theta = 0. \quad (\text{A.15})$$

Defining the variables

$$dr = \frac{n_1^2 dt}{n^2(\vec{r})} \quad (\text{A.16})$$

$$Q^2 = \frac{2\Delta}{a^2} \quad (\text{A.17})$$

$$v = \frac{c}{n_1} \quad (\text{A.18})$$

and rewriting eqns. (A.7) to (A.9) and eqns. (A.13) to (A.15) with $\frac{d}{dr}$ replaced by ' (prime)

$$x' = \frac{v^2 k_x}{\omega} \quad (\text{A.19})$$

$$k_x' = -Q^2 \omega x \quad (\text{A.20})$$

$$y' = \frac{v^2 k_y}{\omega} \quad (\text{A.21})$$

$$k_y' - k_z \theta' = -Q^2 \omega y \quad (\text{A.22})$$

$$(R+y)\theta' = \frac{v^2 k_z}{\omega} \quad (\text{A.23})$$

$$k'_z + k_y \theta' = 0. \quad (\text{A.24})$$

Note that eqns. (A.19) and (A.20) are identical to eqns. (2.32) and (2.33) in the straight fiber case indicating that the bend in the y-z plane does not affect the propagation of the ray in the x-direction.

Hence

$$x = x_0 \cos(Qvr) + \frac{vk_{ox}}{\omega Q} \sin(Qvr) \quad (\text{A.25})$$

$$k_x = k_{ox} \cos(Qvr) - \frac{Q\omega x_0}{v} \sin(Qvr). \quad (\text{A.26})$$

Substituting eqns. (A.21) and (A.23) into eqn. (A.24)

$$\frac{k'_z}{k_z} + \frac{y'}{R+y} = 0 \quad (\text{A.27})$$

$$k_z (R+y) = \text{Constant} \quad (\text{A.28})$$

$$k_z = \frac{k_{oz} (R+y_0)}{R+y}. \quad (\text{A.29})$$

Substituting eqns. (A.27) and (A.23) into eqn. (A.22)

$$k'_y = \frac{k_{oz}^2 v^2}{\omega} \frac{(R+y_0)^2}{(R+y)^3} - Q^2 \omega y \quad (\text{A.30})$$

and note that as $R \rightarrow \infty$ (a straight fiber), eqn. (A.30) returns to the same equation as eqn. (2.33) (with y replacing x).

Using eqn. (A.30) into eqn. (A.21)

$$y'' = \frac{v^4 k_{oz}^2}{\omega^2} \frac{(R+y_0)^2}{(R+y)^3} - Q^2 v^2 y \quad (\text{A.31})$$

and rewriting the L.H.S of the above equation as

$$y'' = \frac{d}{dy} \left[\frac{y'^2}{2} \right] \quad (\text{A.32})$$

while the R.H.S as

$$= \frac{1}{2} \frac{d}{dy} \left[\frac{v^4 k_{oz}^2 (R+y_o)^2}{\omega^2 (R+y)^2} - (Qvy)^2 \right]. \quad (\text{A.33})$$

Hence eqn. (A.31) can be rewritten as

$$y'^2 = \frac{v^4 k_{oz}^2 (R+y_o)^2}{\omega^2 (R+y)^2} - (Qvy)^2 + C_1 \quad (\text{A.34})$$

where

$$C_1 = \frac{v^4}{\omega^2} \left\{ k_{oy}^2 + k_{oz}^2 \right\} + (Qvy_o)^2. \quad (\text{A.35})$$

Manipulating the above two equations

$$y'^2 = \frac{v^4}{\omega^2} \left\{ E + F + G \right\} \quad (\text{A.36})$$

where

$$E = k_{oy}^2 + (Qy_o n_1 k_o)^2 \quad (\text{A.37})$$

$$F = k_{oz}^2 \left[1 - \frac{(R+y_o)^2}{(R+y)^2} \right] \quad (\text{A.38})$$

$$G = - (Qn_1 k_o y)^2. \quad (\text{A.39})$$

To approximate the solution, the term within brackets in eqn. (A.38) is expanded to the first order

$$\left[1 - \frac{(R+y_o)^2}{(R+y)^2} \right] \approx 1 - \left[1 + \frac{2y_o}{R} \right] \left[1 - \frac{2y}{R} \right]$$

$$\propto \frac{2(y-y_0)}{R} . \quad (\text{A.40})$$

Rewriting eqn. (A.38)

$$F = - \frac{2k_{oz}^2 y_0}{R} + \frac{2k_{oz}^2 y}{R} . \quad (\text{A.38})$$

Completing the square on eqn. (A.36)

$$y'^2 - \frac{v^2}{n_1^2 k_o^2} \gamma^2 - v^2 Q^2 \left[y - \frac{k_{oz}^2}{R n_1^2 k_o^2 Q^2} \right]^2 \quad (\text{A.41})$$

where

$$\gamma^2 = \frac{k_{oz}^4}{R^2 n_1^2 k_o^2 Q^2} + k_{oy}^2 + \left[Q y_0 n_1 k_o \right]^2 - \frac{2k_{oz}^2 y_0}{R} . \quad (\text{A.42})$$

The solution to eqn. (A.41) is

$$y = \frac{k_{oz}^2}{n_1^2 k_o^2 Q^2 R} + \frac{\gamma}{n_1 k_o Q} \sin(Qvr + \phi) \quad (\text{A.43})$$

where ϕ depends on the initial conditions.

Recall eqn. (A.21) where

$$k_y = \frac{y' \omega}{v^2} \quad (\text{A.21})$$

and since the solution for y has been presented, the wave vector in the y -direction can be determined, using eqn. (A.43) in eqn. (A.21)

$$k_y = \gamma \cos(Qvr + \phi) . \quad (\text{A.44})$$

To complete the set of equations, the propagation constant in the z -direction can be determined by

$$k_z = \left[(k_o n_1)^2 \left(1 - 2\Delta \frac{x^2 + y^2}{a^2} \right) - k_x^2 - k_y^2 \right]^{1/2} \quad (\text{A.45})$$

and the distance travelled around the bend can be estimated by

$$\theta = \frac{r c}{n_1 R} . \quad (\text{A.46})$$

Thus by using eqns. (A.25), (A.26), (A.43), (A.44), (A.45) and (A.46) the propagation of a ray in a bent parabolic graded-index fiber can be determined.

Appendix B

Ray Propagation in a Bent Constant Index Media

Recall from Section 2.3, the two general ray equations:

$$\frac{d\vec{r}}{dt} = \frac{c^2 \vec{k}}{n^2(\vec{r}) \omega} \quad (\text{B.1})$$

$$\frac{d\vec{k}}{dt} = \frac{\omega}{2n^2(\vec{r})} \nabla_{\vec{r}} n^2(\vec{r}) . \quad (\text{B.2})$$

The derivation is similar to the derivation in Appendix A for a parabolic graded-index media, however in this case

$$\nabla_{\vec{r}} n^2(\vec{r}) = 0. \quad (\text{B.3})$$

Following the same procedure as before, six equations similar to eqns. (A.19) to (A.24) is derived,

$$x' = \frac{c^2 k_x}{n^2 \omega} \quad (\text{B.4})$$

$$k'_x = 0 \quad (\text{B.5})$$

$$y' = \frac{c^2 k_y}{n^2 \omega} \quad (\text{B.6})$$

$$k'_y - k_z \theta' = 0 \quad (\text{B.7})$$

$$(R+y)\theta' = \frac{c^2 k_z}{n^2 \omega} \quad (\text{B.8})$$

$$k'_z + \theta' k_y = 0 \quad (\text{B.9})$$

where n is the refractive index of the media and $x' = \frac{dx}{dt}$.

From eqns. (B.4) and (B.5),

$$k_x = \text{Constant} = k_{ox} \quad (\text{B.10})$$

$$x = \frac{c^2 k_{ox}}{n^2 \omega} t + C_1 \quad (\text{B.11})$$

where C_1 is the integration constant.

Using eqns. (B.6) and (B.8) into eqn. (B.9)

$$\frac{k'_z}{k_z} + \frac{y'}{(R+y)} = 0 \quad (\text{B.12})$$

$$k_z = \frac{k_{oz} (R+y_o)}{(R+y)} \quad (\text{B.13})$$

Differentiating eqn. (B.6) again and using eqns. (B.7), (B.8) and (B.13) results in a second order differential equation,

$$y'' = \frac{v^4 (R+y_o)^2}{\omega^2 (R+y)^3} k_{oz}^2 \quad (\text{B.14})$$

Applying the same procedure as in the derivation of eqns. (A.32) to (A.40) in Appendix A,

$$y'^2 = \frac{v^2}{n^2 k_o^2} \delta^2 + \frac{2v^2 k_{oz}^2}{n^2 k_o^2 R} y \quad (\text{B.15})$$

where

$$\delta^2 = k_{oy}^2 - \frac{2k_{oz}^2 y_o}{R} \quad (\text{B.16})$$

Solving eqn. (B.15)

$$y = \left[\frac{v^2 k_{oz}^2}{2Rn^2 k_o^2} (t+C_2)^2 - \frac{\delta^2 R}{2k_{oz}^2} \right] \quad (\text{B.17})$$

where C_2 depends on the initial condition. Substituting the solution for y into eqn. (B.6)

$$k_y = \frac{k_{oz}^2 \omega}{n^2 k_o^2 R} (t + C_2) \quad (B.18)$$

To complete the set of equations, the wave vector in the z -direction can be determined by

$$k_z = \left[(k_o n_1)^2 \left(1 - 2\Delta \frac{x^2 + y^2}{a^2} \right) - k_x^2 - k_y^2 \right]^{1/2} \quad (B.19)$$

and the distance travelled around the bend can be estimated (as $R \gg a$) by using the straight line approximation

$$\left[(x_2 - x_1)^2 + (y_2 - y_1)^2 + (z_2 - z_1)^2 \right]^{1/2} = \frac{ct_1}{n} \quad (B.20)$$

where variables with subscripts '1' and '2' denote initial position and final position of the ray and t_1 represents the time the ray spends in that media. Thus using eqns. (B.10), (B.11), (B.17) to (B.20), the ray propagation in a curved constant index media can be determined.

It can be shown that as $R \rightarrow \infty$ (straight fiber case), eqns. (B.17) and (B.18) will become

$$y = \frac{c^2 k_{oy}}{n^2 \omega} t + y_o \quad (B.21)$$

$$k_y = \text{Constant} = k_{oy} \quad (B.22)$$

which is the basic ray equation in a medium of refractive index n .

Appendix C

Effect of Stress on the Ray Propagation in a Bent Fiber

From eqn. (5.9), the effective refractive index due to a dominant stress factor in the z-direction is

$$n_{\text{eff}}(r) = n(r) - \frac{n^3 y}{2R} \left[-\alpha\beta + \beta(1-\nu) \right]. \quad (5.9)$$

To obtain an analytical solution, eqn. (5.9) can be rewritten as

$$n_{\text{eff}}^2(r) \approx n^2(r) - n_1^4 \theta \frac{y}{R} \quad (6.1)$$

where

$$\theta = -\alpha\beta + \beta(1-\nu). \quad (6.2)$$

Following the same procedure as in Appendix A, a similar equation to eqn. (A.30) can be derived

$$k'_y = \frac{k_{oz}^2 v^2 (R+y_o)^2}{\omega (R+y)^3} - Q^2 \omega y - \frac{\omega n_1^2 \theta}{2R}. \quad (6.3)$$

Proceeding with the new equation for k'_y , the equations as in eqn. (A.36), (A.37) and (A.39) can be derived. The only modification is to eqn. (A.38) which with the approximation (eqn. (A.40)) can be rewritten as

$$F = -\frac{2k_{oz}^2 y_o}{R} \left[1 - \frac{n_1^4 k_o^2 \theta}{2k_{oz}^2} \right] + \frac{2k_{oz}^2 y}{R} \left[1 - \frac{n_1^4 k_o^2 \theta}{2k_{oz}^2} \right]. \quad (6.4)$$

Introducing the variable

$$R_{\text{eff}} \approx \frac{2R}{2 - n_1^2 \theta}, \quad (6.5)$$

eqn. (6.4) can be rewritten as

$$F = \frac{2k_{oz}^2 y_o}{R_{eff}} + \frac{2k_{oz}^2 y}{R_{eff}} \quad (C.6)$$

Eqn. (C.6) is identical to eqn. (A.38) with R_{eff} instead of R . Therefore, the ray propagation equations for a bent fiber are identical with the introduction of the stress. However, the stress introduces an effective radius of curvature.

Appendix D

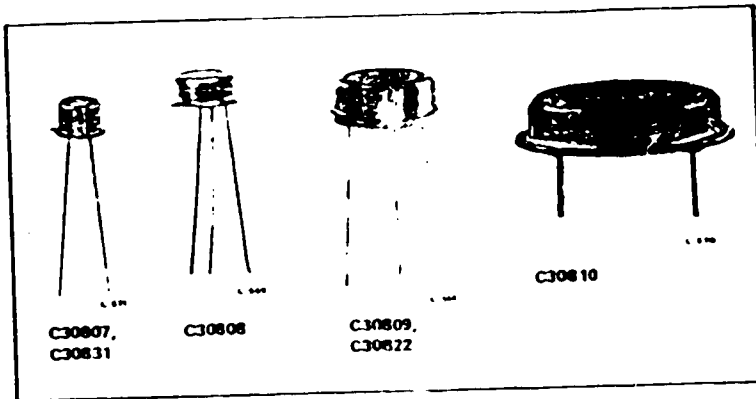
Detector Data Sheets

RCA ElectroOptics
and Devices

Photodiode
Developmental Types

C30807, C30808, C30809,
C30810, C30822, C30831

N-Type Silicon p-i-n Photodetectors



- Broad Range of Photosensitive Surface Areas - 0.2 mm² to 100 mm²
- Low Operating Voltage - V_R = 45 V
- Anti-Reflection Coated to Enhance Responsivity at 900 nm
- Hermetically Sealed Packages
- Spectral Response Range - (10% Points) 400 to 1100 nm

This family of N-type silicon p-i-n photodiodes is designed for use in a wide variety of broad band low light level applications covering the spectral range from below 400 to over 1100 nanometers.

The different types making up this series provide a broad choice in photosensitive areas and in time response characteristics. Each of the types is anti-reflection coated to enhance responsivity at 900 nanometers.

These characteristics make the devices highly useful in HeNe and GaAs laser detection systems and in optical demodulation, data transmission, ranging, and high-speed switching applications.

Maximum Ratings, Absolute-Maximum Values (All Types)

DC Reverse Operating Voltage, V _R	100 max.	V
Photocurrent Density, i _p , at 22° C:		
Average value, continuous operation	5	mA/mm ²
Peak value	20	mA/mm ²
Forward Current, I _F :		
Average value, continuous operation	10 max.	mA
Peak value	100 max.	mA
Ambient Temperature:		
Storage, T _{stg}	-60 to +100	°C
Operating, T _A	-40 to +80	°C
Soldering:		
For 5 seconds	200	°C

Mechanical Characteristics

Photosensitive Surface:

Shape -		Circular
All types		
Area -		
Type C30831	0.2	mm ²
Type C30807	0.8	mm ²
Type C30808	5	mm ²
Type C30822	20	mm ²
Type C30809	50	mm ²
Type C30810	100	mm ²

Optical Characteristics

Field of View ^a
See Figure 5

Approx Full Angle For -	Totally Illuminated Photosensitive Surface	Partially Illuminated Photosensitive Surface	
Type C30831	70	84	deg
Type C30807	62	90	deg
Type C30808	77	120	deg
Type C30822	104	144	deg
Type C30809	74	148	deg
Type C30810	74	140	deg

^a The values specified for field of view are approximate and are critically dependent on the dimensional tolerances of the package component parts.

C30807, C30808, C3080
C30810, C30822, C30831

Electrical Characteristics at $T_A = 22^\circ\text{C}$	At a DC Reverse Operating Voltage (V_R) = 45 Volts ^b , Unless Otherwise Specified									Units
	Type C30810			Type C30822			Type C30831			
	Min.	Typ.	Max.	Min.	Typ.	Max.	Min.	Typ.	Max.	
Breakdown Voltage, V_{BR}	100	-	-	100	-	-	100	-	-	V
Responsivity										
At 900 nm	0.5	0.6	-	0.5	0.6	-	0.5	0.6	-	A/W
At 1060 nm	0.1	0.15	-	0.1	0.15	-	0.1	0.15	-	A/W
Luminous Responsivity (2856 K)	-	8.5	-	-	8.5	-	-	8.5	-	mA/m
Quantum Efficiency:										
At 900 nm	70	83	-	-	83	-	-	83	-	%
At 1060 nm	12	17	-	-	17	-	-	17	-	%
Dark Current, I_d :										
At $V_R = 10\text{ V}$	-	8×10^{-8}	4×10^{-7}	-	1×10^{-8}	5×10^{-8}	-	1×10^{-9}	5×10^{-9}	A
At $V_R = 45\text{ V}$	-	3×10^{-7}	1.5×10^{-6}	-	5×10^{-8}	2.5×10^{-7}	-	1×10^{-8}	5×10^{-8}	A
See Figure 2										
Noise Current, i_n :										
$f = 1000\text{ Hz}$, $\Delta f = 10\text{ Hz}$	-	3×10^{-13}	2.1×10^{-12}	-	1.3×10^{-13}	9×10^{-13}	-	6×10^{-14}	4.2×10^{-13}	A/Hz ^{1/2}
See Figure 3										
Noise Equivalent Power (NEP):										
$f = 1000\text{ Hz}$, $\Delta f = 10\text{ Hz}$	-	4.5×10^{-13}	3.6×10^{-12}	-	2×10^{-13}	1.5×10^{-12}	-	1×10^{-13}	8×10^{-13}	W/Hz ^{1/2}
At 900 nm	-	2×10^{-12}	1.6×10^{-11}	-	8×10^{-13}	7×10^{-12}	-	4×10^{-13}	3.2×10^{-12}	W/Hz ^{1/2}
At 1060 nm	-	70	90	-	17	20	-	2	2.5	pF
Capacitance, C_d										
See Figure 4										
Rise Time, t_r :										
$R_L = 50\ \Omega$, $\lambda = 900\text{ nm}$, 10% to 90% points	-	12	17	-	7	12	-	3	5	ns
Fall Time										
$R_L = 50\ \Omega$, $\lambda = 900\text{ nm}$, 90% to 10% points	-	20	30	-	10	15	-	6	10	ns

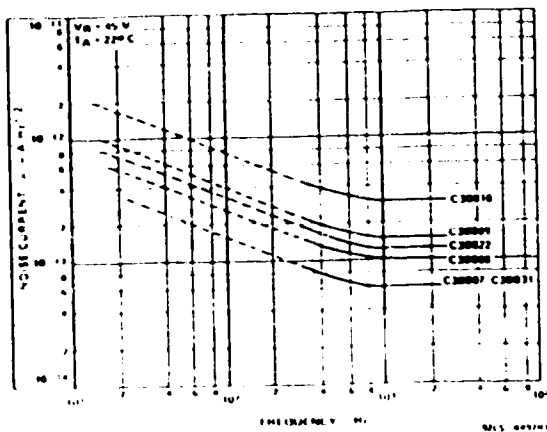


Figure 3 - Typical Noise Current vs Frequency

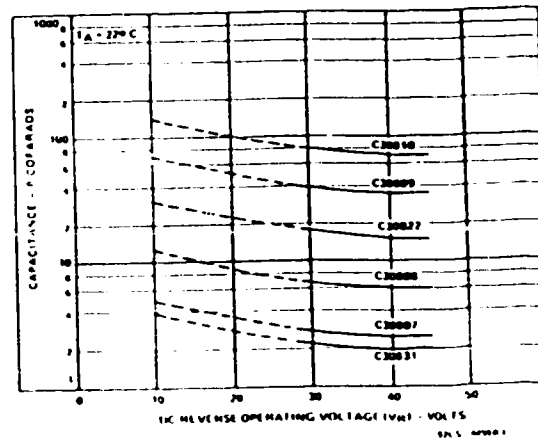


Figure 4 - Typical Photodiode Capacitance vs Operating Voltage

C30807, C30808, C30809,
C30810, C30822, C30831

Electrical Characteristics at $T_A = 22^\circ\text{C}$	At a DC Reverse Operating Voltage (V_R) = 4V (typ), Unless Otherwise Specified						Units			
	Type C30807			Type C30808		Type C30809				
	Min.	Typ.	Max.	Min.	Max.	Min.	Typ.	Max.		
Breakdown Voltage, V_{BR}	100	-	-	100	-	100	-	-	V	
Responsivity:										
At 900 nm	0.5	0.6	-	0.5	0.6	0.5	0.6	-	A/W	
At 1060 nm	0.1	0.15	-	0.1	0.15	0.1	0.15	-	A/W	
Luminous Responsivity (2856 K)	-	8.5	-	-	8.5	-	8.5	-	mA/lm	
Quantum Efficiency:										
At 900 nm	70	83	-	70	83	70	83	-	%	
At 1060 nm	12	17	-	12	17	12	17	-	%	
Dark Current, I_d :										
At $V_R = 10\text{V}$	-	2×10^{-9}	1×10^{-8}	-	5×10^{-9}	2.5×10^{-8}	-	2.5×10^{-8}	1.3×10^{-7}	A
At $V_R = 45\text{V}$	-	1×10^{-8}	5×10^{-8}	-	3×10^{-8}	1.5×10^{-7}	-	7×10^{-8}	3.5×10^{-7}	A
See Figure 2										
Noise Current, i_n :										
$f = 1000\text{ Hz}$, $\Delta f = 1.0\text{ Hz}$	-	6×10^{-14}	4.2×10^{-13}	-	1×10^{-13}	7×10^{-13}	-	1.5×10^{-13}	1.1×10^{-12}	A/Hz ^{1/2}
See Figure 3										
Noise Equivalent Power (NEP):										
$f = 1000\text{ Hz}$, $\Delta f = 1.0\text{ Hz}$	-	1×10^{-13}	8×10^{-13}	-	1.5×10^{-13}	1.2×10^{-12}	-	2×10^{-13}	1.6×10^{-12}	W/Hz ^{1/2}
At 900 nm	-	4×10^{-13}	3.2×10^{-12}	-	6.5×10^{-13}	5.2×10^{-12}	-	1×10^{-12}	8×10^{-12}	W/Hz ^{1/2}
At 1060 nm	-	2.5	3	-	6	10	-	35	45	pF
Capacitance, C_d	-	2.5	3	-	6	10	-	35	45	pF
See Figure 4										
Rise Time, t_r :										
$R_L = 50\ \Omega$, $\lambda = 900\text{ nm}$, 10% to 90% points	-	3	5	-	5	8	-	10	15	ns
Fall Time:										
$R_L = 50\ \Omega$, $\lambda = 900\text{ nm}$, 90% to 10% points	-	6	10	-	8	13	-	15	20	ns

b. The recommended range of reverse operating voltage V_R at $T_A = 22^\circ\text{C}$ is 0 to 50 volts. However, when the devices are operated in the photovoltaic mode, i.e., at $V_R = 0$ volts, some of the electrical characteristics will differ from those shown.

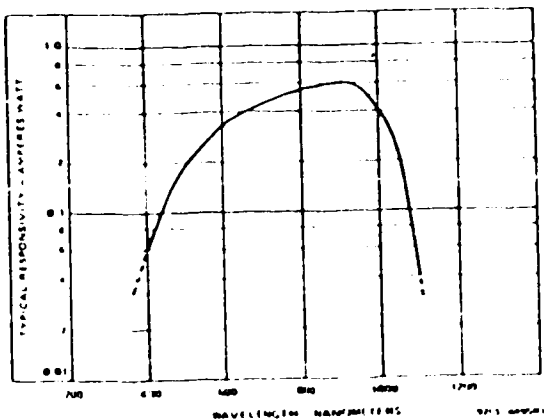


Figure 1 - Typical Spectral Responsivity Characteristic

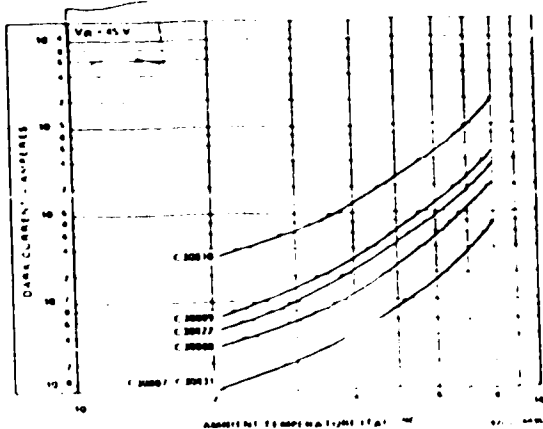


Figure 2 - Typical Dark Current vs Ambient Temperature

Appendix E

Corning Fiber Data Sheets

CORNING

Telecommunications Products Division
Corning Glass Works
Corning, New York 14831, USA
Tel 607-974-4411
Telex 932498

Corguide Optical Fiber

Product Information

50/125 μm LDF™ CPC3 Multimode Optical Fiber

Issued 1/89

Supersedes 9/87

1.0 General

Corguide® LDF™ Long Distance Fiber is a graded index multimode fiber with a 50/125 μm core/cladding diameter. LDF fiber is specified for operation at the 850 nm and 1300 nm wavelengths.

CPC3 is a mechanically strippable acrylate coating with a 250 μm nominal outside diameter. It is primarily used in loose tube and slotted core cable designs, or overcoated for use in tight buffer cable designs.

Typical applications are telephony, distribution and local networks, carrying data, voice and/or video services. This product offers both the highest bandwidth and the lowest attenuation of any multimode fiber type available.

2.0 Optical Specifications

Attenuation:

Standard Attenuation Cells:

Attenuation Cells [dB/km]	
850 nm	1300 nm
$\leq 2.4 - \leq 3.0$	$\leq 0.6 - \leq 1.2$

Special attenuation cells available upon request

Attenuation Uniformity:

No point discontinuity greater than 0.2 dB at either 850 nm or 1300 nm

Attenuation Difference:

The attenuation at 1380 nm does not exceed the attenuation at 1300 nm by more than 3.0 dB/km.

Bandwidth:

Standard Bandwidth Cells:

Bandwidth Cells (MHz·km)	
850 nm	1300 nm
≥ 400 – ≥ 1000	≥ 400 – ≥ 1500

Special bandwidth cells available upon request

Core Diameter: $50.0 \pm 3.0 \mu\text{m}$

Numerical Aperture: 0.200 ± 0.015

3.0 Environmental Specifications

Environmental Test Method	Induced Attenuation [dB/km]	
	850 nm	1300 nm
Temperature Dependence – 60°C to + 85°C	≤ 0.2	≤ 0.2
Temperature-Humidity Cycling – 10°C to + 65°C ≤ 98% Relative Humidity	≤ 0.2	≤ 0.2

Operating Temperature Range: – 60°C to + 85°C

4.0 Dimensional Specifications

Standard Lengths: 1,100, 1,700, and 2,200 m
Special lengths available upon request.

Glass Geometry:

Cladding Diameter: $125.0 \pm 3.0 \mu\text{m}$

Core to Cladding Offset: $\leq 3.0 \mu\text{m}$

Cladding Non-Circularity: $\leq 2\%$

$$\text{Defined as: } \left[1 - \frac{\text{Min. Cladding Diameter}}{\text{Max. Cladding Diameter}} \right] \times 100$$

Core Non-Circularity: $\leq 6\%$

$$\text{Defined as: } \left[1 - \frac{\text{Min. Core Diameter}}{\text{Max. Core Diameter}} \right] \times 100$$